NTNU – Trondheim
Norwegian University of
Science and Technology

Fabrication of a Silicon Photonic Crystal Biosensor

Torstein Bolstad

Nanotechnology
Submission date: June 2014
Supervisor: Astrid Aksnes, IET
Co-supervisor: Kay Gastinger, NanoLab

Norwegian University of Science and Technology
Department of Electronics and Telecommunications

Problem description

Microphotonics is a sub-branch of photonics oriented towards integrated systems on a single semiconductor chip. It involves the design, fabrication and testing of optical components to be fabricated at micro- or even nano-scale. Examples of these components are dielectric waveguides, micro-resonators, light modulators, couplers, periodic structures and more.

In this thesis, the focus will be on design and fabrication of a silicon photonic crystal biosensor structure. Simulations of non-ideal structures will be performed to investigate the effect of imperfections during fabrication. Both COMSOL Multiphysics and MIT Photonic Bands will be utilized.

The structures will be fabricated in the cleanroom at NTNU NanoLab. The fabrication of the photonic crystal will be based upon milling with focused ion beam, and most of the work will be spent on finding optimal process parameters. The use of SiO_2 and TiO_2 thin films as protective layers, and, in the case of SiO_2, as a hard mask for processing with plasma, will be studied. Thin films will be deposited using plasma enhanced vapor deposition and electron beam physical vapor deposition. The fabrication of input and output waveguides as well as a plateau to support the photonic crystal will be based on electron beam lithography and plasma etching. Resulting structures will be characterized using profilometer and scanning electron microscope. The work will be done with future fabrication using silicon on insulator in mind. The silicon sensor to be fabricated in the master project is a basis for a biosensor.

Cleanroom fabrication does not only rely upon well-established theories, but also a lot of 'know-how', which must be learned by experience. Fabrication is experimental work, and it is expected that a significant amount of time will be spent on learning the processes by hands-on experience. The thesis should seek to provide a contribution to the competence and common knowledge in the cleanroom, providing a foundation for future work on photonic crystals and silicon photonics.

Abstract

The research performed in the scope of the master project and described in this thesis is devoted to the study of a two dimensional photonic crystal biosensor in silicon. The band gap of hexagonal photonic crystal slab structures is simulated using MIT Photonic-Bands (MPB) and the dependence of slab thickness, substrate and hole depth is found. The effect of relevant fabrication errors are investigated with COMSOL Multiphysics. It is found that even small fabrication errors leads to a resonance peak split.

The photonic crystal is fabricated using a focused ion beam (FIB) system. The effect of ion beam energy, current and dwell time on the fabricated holes are studied on uncovered silicon samples and silicon samples covered with 40nm TiO_2 and 100nm SiO_2 thin films. The best result was achieved for a titanium dioxide covered sample milled with 30kV ions at a current of 9pA, a dwell time of 1ms, and a dose of 666.65pC/μm^2 yielding a sidewall angle of 3.2 degrees. Cross section of the milled holes reveas that the FIB produced very smooth hole sidewalls.

Patterning of a silicon oxide hard mask with FIB for inductively coupled plasma reactive ion etching (ICP-RIE) is investigated. It is found that the used etch chemistry (SF_6/CHF_3) gives very poor selectivity and is unsuitable for this purpose.

Input and output waveguides along with a plateau to support the photonic crystal is constructed using an electron beam lithography (EBL) and ICP-RIE process adapted from previous work at NTNU. Reproducing the results are proved difficult, finally achieving a sidewall roughness of approximately 10nm.

The full structure of waveguides and photonic crystal sensor is fabricated using a combination of EBL and FIB milling. The results are the best achieved at NTNU for use in photonic crystals with regards to hole shape and sidewall smoothness.

Sammendrag

Arbeidet i denne oppgaven omhandler et studie av en todimensjonal fotonisk krystall biosensor i silisium. Båndgapet til den heksagonale fotoniske krystall skiven er simulert ved hjelp av MIT Photonic-Bands (MPB) og avhengigheten på skive tykkelse, substrat og hull dybde er funnet. Effekten av relevante fabricasjonsfeil er undersøkt ved hjelp av COMSOL Multiphysics. Det er funnet at små fabricasjonsfeil leder til at resonanstoppen splittes.

Den fotoniske krystallen er fabrikert med et fokusert ionestrålesystem (FIB). Effekten av ionestråleenergi, strøm og holdetid på de fabrikerte hullene er studert på udekkede silisiumprøver og silisiumprøver dekket med 40nm titandioksid og 100nm silisiumdioksid tynnfilmer. Det beste resultatet kommer fra en titandioksiddekket prøve frest med 30kV ioner med en strøm på 9pA, en holdetid på 1ms og en dose på 666.65pC/μm^2 som ga en sideveggvinkel på 3.2 grader. Tverrsnittet til de freste hullene viser at den fokuserte ionestrålen produserte glatte sidevegger.

Mønstring av en silisiumdioksid hardmaske med FIB for induktivt koblet plasna reaktiv ioneets (ICP-RIE) er undersøkt. Det er funnet at den brukte etsekjemien (SF_6/CHF_3) gir dårlig selektivitet og er uegnet for dette formålet.

Inngangs- og utgangsbølgeledere sammen med et platå for den fotoniske krystallen er konstruert med en elektronstrålelitografi- (EBL) og ICP-RIE-prosess adaptert fra tidligere arbeid ved NTNU. Reproduksjon av resultatene er vist vanskelig og en sideveggruhet på 10nm er oppnådd.

Den fulle strukturen med bølgeledere og fotonisk krystallsensor er fabrikert med en kombinasjon av EBL og FIB fresing. I forhold til tidligere arbeid med fotoniske krystaller på NTNU er dette det beste resultatet med tanke på hullvegglatthet og hullform.

Preface

This thesis is delivered in partial fulfilment for the degree of M.Sc. in Nanotechnology at the Department of Electronics and Telecommunications at the Norwegian University of Science and Technology, NTNU. The work contained within this thesis is the individual work of the author except for some important contributions by the people acknowledged below.

Acknowledgements

First I would like to thank my supervisor, professor Astrid Aksnes, for her help on both this thesis and the project thesis. She has helped with management of the work, interpretation of the results, and getting me in contact with other authorities when I had questions she was unable to answer. Her willingness to get up early in the morning to have skype meetings has also been greatly appreciated.

Secondly I would like to thank my co-supervisor, Kay Gastinger. As the head of NTNU NanoLab, he has helped me with all questions related to the clean room and the results attained there, both through his own expertise and with the help of his staff.

Therefore an important thanks goes out to Espen Rogstad, Mark Chiappa, and Ken Roger Ervik, enigneers at NTNU NanoLab, for all their help with training and questions regarding the use and operation of the instruments in the cleanroom.

Lastly a thanks goes to my fellow students for helpful discussions and tips both regarding the theoretical and practical aspects of the work in this thesis.

Previous work

This thesis is a continuation of the project thesis, completed fall 2013. The work on the thesis included simulations of a photonic crystal sensor and its potential as a sensor of biomolecules. The simulations were carried out using COMSOL Multiphysics and MIT Photonic-Bands. Some of the content from the project thesis is reprinted or adapted for use in this thesis, specifically some paragraphs of the introduction, sections of the theory chapter, and some results.

Trondheim, 2014-06-16

Torstein Bolstad

Contents

List of Figures

List of Tables

Chapter 1

Introduction

Ever increasing demands for smaller semiconductor components with higher speed, bandwidth and sensitivity has led to extensive research on using photons as information carriers instead of electrons, for instance in integrated circuit components. One of the potentially important parts in such a photonic component could be the photonic crystal [1]. A photonic crystal is a material with a periodic variation in the refractive index. The variation can be in either one, two or three dimensions and the crystal will have different properties depending on the structure and the periodicity. In a normal semiconductor crystal the periodic variation of potential can give a band gap for electrons, i.e. forbidden energy levels [2]. In a photonic crystal the periodic variation in refractive index can lead to a photonic band gap, meaning that certain frequencies are not allowed.

The concept of a photonic crystal comes from the work of Yablonovitch [3] and John [4] in 1987. After the discovery, photonic crystals have been used in a myriad of different applications. Examples include the use of photonic crystals as waveguides [5, 6, 7], as filters, in high quality factor cavities [8, 9, 10], and as sensors [11, 12, 13].

This Master's thesis is based on a photonic crystal biosensor designed by Mindy Lee and Philippe M. Fauchet [13]. This two-dimensional photonic crystal is based on silicon on insulator (SOI). Silicon is the material most extensively used in the CMOS industry [14, p. 33] and is the second most abundant element on earth [14, p. 34]. This makes component fabrication with silicon as a starting point much cheaper than other materials due to the high availability and that the fabrication techniques used have been refined by a large industry over several years.

Traditionally III-V semiconductor materials have been the material of choice for photonic components [15], but silicon has become more important and has been the basis for much research [15, 16]. Using silicon also makes integration with electrical circuits convenient because the complete component can be constructed on the same wafer. Monolithic integration of Si and GaAs, a popular III-V material used in photonics, is difficult due to different lattice constants [17].

Silicon is easy to oxidize [14, ch. 10] and the refractive index of silicon oxide is approximately 1.45 compared to approximately 3.48 for Si at optical wavelengths [16] giving good

confinement in SOI-devices.

Two-dimensional photonic crystals are interesting for use in bio-sensing devices because the light propagation occurs in-plane, allowing integration on a single-chip bio-sensing device [18]. Usually the sensor works by monitoring changes in the transmission spectrum of the crystal when biomolecules bind to the surface. Photonic crystal sensors are predicted to be able to detect down to femtogram of analyte [13, 19]. They have been used to sense various molecules like proteins and solvents [19, 20].

Fabrication of photonic crystals has been done using a variety of methods, including focused ion beam (FIB) [21, 22, 23], electron beam lithography (EBL) [24, 25, 26, 27], and optical lithography [28, 29, 30]. In the last few years there have been several attempts at fabrication of two-dimensional photonic crystal structures in silicon at the NTNU NanoLab [31, 32], and one attempt at the fabrication of a waveguide resonator [33]. These Master's theses were the first endeavours to fabricate silicon photonic structures, all using EBL.

This thesis will investigate the fabrication of a two dimensional photonic crystal structure using the FIB system at NTNU NanoLab. An undertaking which has not previously been attempted at NTNU. The effect of changing the available FIB milling variables will be studied, both on standard silicon samples and on thin film covered silicon samples deposited using plasma enhanced chemical vapor deposition (PECVD) and electron beam physical vapor deposition (e-beam evaporation). In addition, input and output waveguides will be fabricated using EBL and etched using inductively coupled plasma reactive ion etching (ICP-RIE).

In addition to the fabrication this thesis will present simulations of relevant band structures using MIT Photonic-Bands and simulations of the effect of probable fabrication errors on the resonance peak using COMSOL Multiphysics.

Much of the time at the start of the thesis work was needed to get familiarized with the great number of instruments used in this work. The work on the EBL fabricated structure was also hampered by unforeseen long down times (from the start of January until end of February and from the middle of April until the middle of May).

The following chapter will introduce the basic electromagnetic theory and how it applies to photonic crystals. At the end of the chapter theory needed to understand the behaviour of photonic crystal defects is presented. Chapter 3 shows the expected photonic band gaps of the fabricated structures and the effect of predicted fabrication errors. In chapter 4 the equipment used and basic theory of operation is described and the work flow is presented. Chapter 5 presents the results of the fabrication and discusses these. Lastly chapter 6 gives conclusions gained from the work and describes potential future work.

Chapter 2

Theory

Some sections of this chapter have been adapted from the project thesis [34], specifically sections 2.1-2.4 and section 2.6.1.

When establishing a theoretical basis for the study of photonic crystals we start with Maxwell's equations [35, p. 6].

$$\nabla \times \mathbf{E} = -\frac{\delta \mathbf{B}}{\delta t} \tag{2.1}$$

$$\nabla \times \mathbf{H} = \mathbf{J} + \frac{\delta \mathbf{D}}{\delta t} \tag{2.2}$$

$$\nabla \cdot \mathbf{D} = \rho \tag{2.3}$$

$$\nabla \cdot \mathbf{B} = 0 \tag{2.4}$$

where $\mathbf{E}(\mathbf{r}, t)$ is the electric field, $\mathbf{H}(\mathbf{r}, t)$ the magnetic field, $\mathbf{D}(\mathbf{r}, t)$ the electric flux density, $\mathbf{B}(\mathbf{r}, t)$ the magnetic flux density, $\mathbf{J}$ the current density and ρ the free charge density. We only study the propagation of light through a mixed dielectric medium with no currents or free charge and do not vary with time, i.e. $\mathbf{J}, \rho = 0$. For the materials usually used we can assume that they are linear, isotropic and non-dispersive [35, p. 7]. Because of that we can relate $\mathbf{E}$ to $\mathbf{D}$ and $\mathbf{H}$ to $\mathbf{B}$ with

$$\mathbf{D}(\mathbf{r}) = \epsilon_0 \epsilon(\mathbf{r}) \mathbf{E} \tag{2.5}$$

$$\mathbf{B}(\mathbf{r}) = \mu_0 \mu(\mathbf{r}) \mathbf{H} \tag{2.6}$$

where ϵ_0 is the electric permittivity in vacuum, ϵ is the relative permittivity, μ_0 is the magnetic permeability in vacuum and μ is the relative permeability. The materials we look at are not magnetic so we set $\mu = 1$. Combining these equations gives

$$\nabla \times \mathbf{E} = -\mu_0 \frac{\delta \mathbf{H}}{\delta t} \tag{2.7}$$

$$\nabla \times \mathbf{H} = \epsilon_0 \epsilon(\mathbf{r}) \frac{\delta \mathbf{E}}{\delta t} \tag{2.8}$$

$$\nabla \cdot \mathbf{E} = 0 \tag{2.9}$$

$$\nabla \cdot \mathbf{H} = 0 \tag{2.10}$$

We want to derive an equation from Maxwell's equations that allows us to describe how a photonic crystal works. First we divide equation 2.8 by $\epsilon(\mathbf{r})$ and take the curl which yields $\nabla \times (\frac{1}{\epsilon(\mathbf{r})} \nabla \times \mathbf{H}) = \nabla \times \epsilon_0 \frac{\delta \mathbf{E}}{\delta t}$. Since the nabla operator is time independent and ϵ_0 is a constant we change the order of differentiation and get $\nabla \times (\frac{1}{\epsilon(\mathbf{r})} \nabla \times \mathbf{H}) = \epsilon_0 \frac{\delta \nabla \times \mathbf{E}}{\delta t}$. Combining with equation 2.7 we get $\nabla \times (\frac{1}{\epsilon(\mathbf{r})} \nabla \times \mathbf{H}) = -\mu_0 \epsilon_0 \frac{\delta^2 \mathbf{H}}{\delta t^2}$. From Fourier analysis we know that any solution can be expressed as a superposition of harmonic waves [35, p. 9]. We therefore express the fields as

$$\mathbf{E}(\mathbf{r}, t) = \mathbf{E}(\mathbf{r}) e^{-i\omega t} \tag{2.11}$$

$$\mathbf{H}(\mathbf{r}, t) = \mathbf{H}(\mathbf{r}) e^{-i\omega t} \tag{2.12}$$

where ω is the frequency. Finally we get

$$\nabla \times \left(\frac{1}{\epsilon(\mathbf{r})} \nabla \times \mathbf{H}(\mathbf{r}) \right) = \frac{\omega^2}{c^2} \mathbf{H}(\mathbf{r}) \tag{2.13}$$

with $c = \frac{1}{\sqrt{\mu_0 \epsilon_0}}$ which is the speed of light. This equation is called the master equation. One interesting property of the equation is that it does not have a fundamental length scale, it is scale invariant. If all length scales in the structure are scaled by an integer then ω and $\mathbf{H}$ are scaled by the same integer, i.e. if the lengths are scaled with a then the new frequency is ω/a.

We can perform the same operations on equation 2.8 as we did on equation 2.7 and get

$$\nabla \times (\nabla \times \mathbf{E}(\mathbf{r})) = \epsilon(\mathbf{r}) \frac{\omega^2}{c^2} \mathbf{E}(\mathbf{r}) \tag{2.14}$$

These two equations are used to find the electromagnetic properties of photonic crystals. They are usually very hard to solve analytically and in most cases numerical tools are used to solve them.

The photonic band gap will be explained physically in two different ways. First a mathematical justification following Saleh and Teich [36, ch. 7] and then a more intuitive one following Joannopolous et al. [35, ch. 2] based on the variational principle.

2.1 One-dimensional photonic crystals

2.1.1 Mathematical justification

This derivation follows the derivation in Saleh and Teich [36, ch. 7] and Dirdal [37]. One-dimensional photonic crystals have periodically varying permittivity in one direction and are constant in the other directions, with the periodicity being on the same order of magnitude as the wavelength of the incoming light. We chose that the permittivity varies in the z-direction and express this mathematically as

$$\epsilon(z + d) = \epsilon(z) \tag{2.15}$$

with d being the period, as illustrated in figure 2.1.

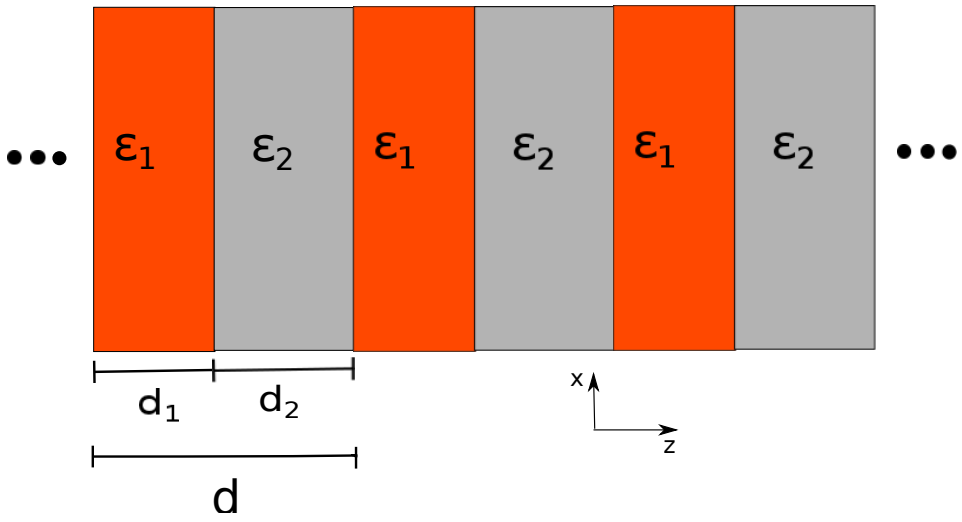

Figure 2.1: The structure of a one-dimensional photonic crystal.

We will use equation 2.14 to calculate the photonic gap. $\nabla \times (\nabla \times \mathbf{E})$ can be expanded in to $\nabla \cdot (\nabla \cdot \mathbf{E}) - \nabla^2 \mathbf{E}$. Inserting equation 2.9 and setting $k = \omega/c$ we get

$$-\nabla^2 \mathbf{E} = \epsilon(\mathbf{r}) k^2 \mathbf{E} \tag{2.16}$$

k is the wave vector of the wave. Since the optical properties vary only in the z-direction the electric field will also only vary in that direction. The nabla operator therefore reduces to $\frac{\delta}{\delta z}$.

$$-\frac{\delta^2 \mathbf{E}(z)}{\delta z^2} = \epsilon(\mathbf{r}) k^2 \mathbf{E}(z) \tag{2.17}$$

This equation is very similar to the equation that describes electrons moving in a crystal [2, p. 118].

$$-\frac{\hbar^2}{2m}\frac{\delta^2 \psi}{\delta z^2} = (E - V(\mathbf{r}))\psi \tag{2.18}$$

The solution to this equation is a Bloch wave with the same periodicity as the crystal [2, p. 119]. The solution to equation 2.17 will therefore be a Bloch wave with the periodicity of the photonic crystal.

$$\begin{aligned} \mathbf{E}(z) &= p_{kz}(z) e^{-ik_{kz}z} \\ p_{kz}(z+d) &= p_{kz}(z) \end{aligned} \tag{2.19}$$

The fact that the Bloch wave is a solution to our problem, and our knowledge of solid state physics, hints that there will be some sort of band gap for photons for the correct structure as there is in semiconductors for electrons.

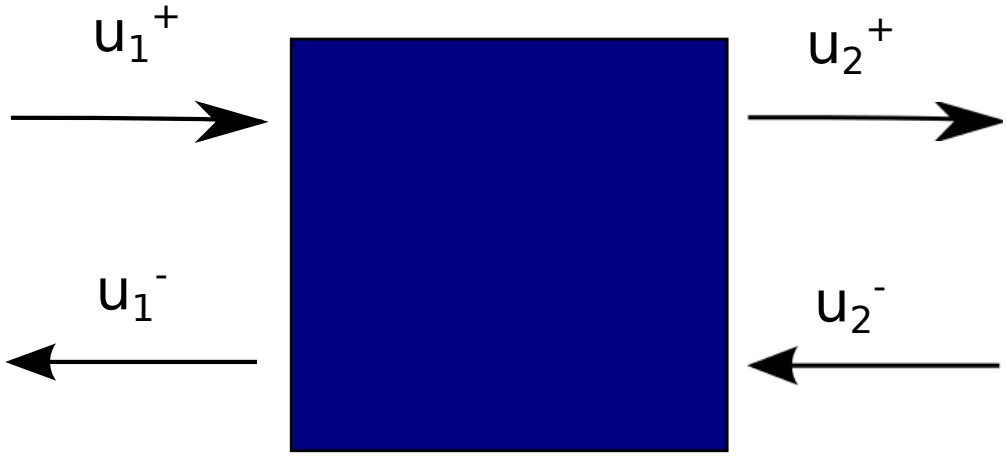

Figure 2.2: One period of the photonic crystal. u_1^+ is the incoming wave to the left, u_1^- is the outgoing wave to the left, u_2^+ is the outgoing wave to the right and u_2^- is the incoming wave to the right.

To help us solve the problem we introduce matrix formalism. We separate each period of the photonic crystal in to a box with an incoming and outgoing wave on each side as seen in figure 2.2. We can construct intuitive equations based on transmission and reflection

$$\begin{aligned} u_2^+ &= t_{12}u_1^+ + r_{21}u_2^- \\ u_1^- &= r_{12}u_1^+ + t_{21}u_2^- \end{aligned} \tag{2.20}$$

$$\begin{bmatrix} u_2^+ \\ u_1^- \end{bmatrix} = S_0 \begin{bmatrix} u_1^+ \\ u_2^- \end{bmatrix} \tag{2.21}$$

$$S_0 = \begin{bmatrix} t_{12} & r_{21} \\ r_{12} & t_{21} \end{bmatrix} \tag{2.22}$$

with t_{ij} is the transmission from material i to material j in figure 2.1 and r_{ij} is the reflection when a wave from material i reaches material j in the same figure. This is called S-matrix formalism. The problem with this formulation is that we cannot multiply the transfer matrixes to get the total transfer matrix when combining several of these boxes. Instead we use M-matrix formalism where the field on one side is expressed by the field on the other side.

$$\begin{bmatrix} u_2^+ \\ u_2^- \end{bmatrix} = M_0 \begin{bmatrix} u_1^+ \\ u_1^- \end{bmatrix} \tag{2.23}$$

$$M_0 = \frac{1}{t_{21}} \begin{bmatrix} t_{12}t_{21} - r_{12}r_{21} & r_{21} \\ -r_{12} & 1 \end{bmatrix} \tag{2.24}$$

If we assume that this is a lossless system then $S_0^\dagger S_0 = I$ where $\dagger$ symbolizes the Hermitian conjugate, i.e. the complex conjugate of the transpose [38, ch. 2]. If reciprocity is also assumed then $|t_{12}| = |t_{21}| = |t|$ and $|r_{12}| = |r_{21}| = |r|$. This gives $|t|^2 + |r|^2 = 1$, $t/r = -(t/r)^*$ and $arg(t) - arg(r) = \pm\pi/2$. Using this we can write M_0 as

$$M_0 = \begin{bmatrix} \frac{1}{t^*} & \frac{r}{t} \\ \frac{r^*}{t^*} & \frac{1}{t} \end{bmatrix} \tag{2.25}$$

The Bloch theorem says that we only get a phase difference by moving a distance d through the crystal. The same distance is traversed by applying M_0 to the field.

$$\begin{bmatrix} u_{m+1}^+ \\ u_{m+1}^- \end{bmatrix} = M_0 \begin{bmatrix} u_m^+ \\ u_m^- \end{bmatrix} = e^{-ikd} \begin{bmatrix} u_m^+ \\ u_m^- \end{bmatrix} \tag{2.26}$$

$$(M_0 - e^{-ikd} I) \begin{bmatrix} u_m^+ \\ u_m^- \end{bmatrix} = 0 \tag{2.27}$$

Solving this gives us the dispersion relation

$$cos(kd) = cos(k_1 d_1 + k_2 d_2) - \frac{(k_1 - k_2)^2}{2k_1 k_2} sin(k_1 d_1) sin(k_2 d_2) \tag{2.28}$$

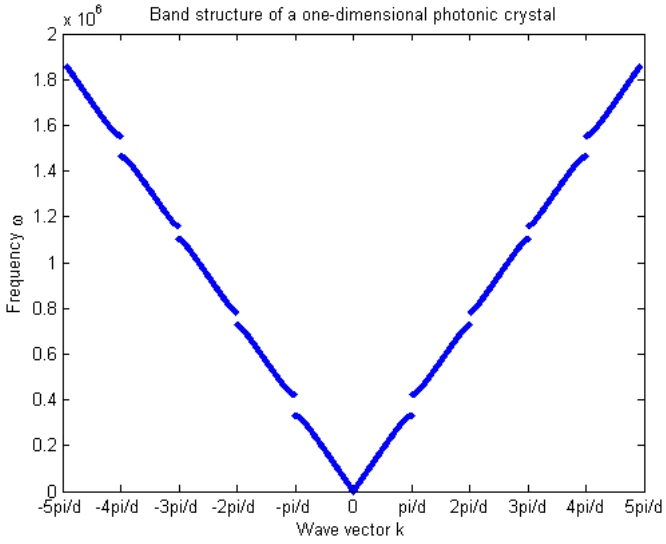

Figure 2.3: A plot of the dispersion relation with periods $d_1 = 1$, $d_2 = 1$, and refractive indices $n_1 = 1$ and $n_2 = 1.5$.

The derivation of this can be seen in appendix B. This relation is plotted in figure 2.3. For some frequencies there are no allowed k-vectors and therefore the frequency is not allowed to propagate in the crystal. The gaps appear at multiples of $\pi/d = g/2$. g is called the reciprocal lattice vector and is the spatial frequency of the medium. The area $-g/2 < k < g/2$ is called the first Brillouin zone. Solutions separated by g are not independent since they give identical Bloch waves. We can see that if we expand $u_{kz}(z)$ from equation 2.19 in to its Fourier components

$$u_{kz}(z) = \sum_{m=-\infty}^{m=\infty} c_m e^{i\frac{2\pi mz}{d}} = \sum_{m=-\infty}^{m=\infty} c_m e^{igmz} \tag{2.29}$$

$$E(z) = u_{kz+g}(z)e^{-i(k_{kz}+g)z} = \sum_{m=-\infty}^{m=\infty} c_m e^{ig(m+1)z} e^{-i(k_{kz}+g)z} = \sum_{m=-\infty}^{m=\infty} c_m e^{imgz} e^{-ik_{kz}z} = u_{kz}(z)e^{-i(k_{kz})z} \tag{2.30}$$

where m is a whole number and c_m is the Fourier coefficients. It is therefore common to use the reduced representation of the band structure where the modes have been moved multiples of g in to the first Brillouin zone (fig. 2.4).

When the refractive index contrast increases the size of the band gap increases as can be seen in figure 2.5.

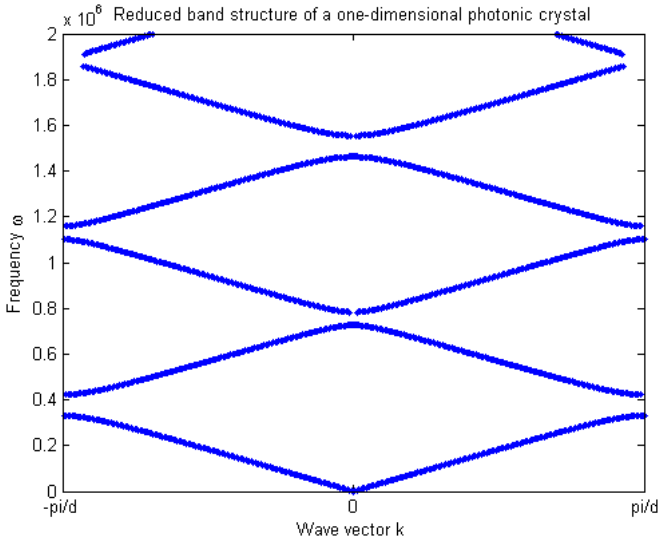

Figure 2.4: A plot of the reduced dispersion relation with $d_1 = 1$, $d_2 = 1$, $n_1 = 1$ and $n_2 = 1.5$.

2.1.2 Justification based on the variational principle

This section follows Joannopolous et al. [35, ch. 2]. We start with the master equation

$$\nabla \times \left(\frac{1}{\epsilon(\mathbf{r})} \nabla \times \mathbf{H}(\mathbf{r}) \right) = \frac{\omega^2}{c^2} \mathbf{H}(\mathbf{r}) \tag{2.31}$$

This can be viewed as an eigenvalue problem with $\hat{\Theta}\mathbf{H}(\mathbf{r}) = \nabla \times (\frac{1}{\epsilon(\mathbf{r})} \nabla \times \mathbf{H}(\mathbf{r}))$ where $\hat{\Theta}$ is an operator acting on the eigenfunction $\mathbf{H}(\mathbf{r})$ with the eigenvalue ω^2/c^2. This is handy because we can use the experience gained from eigenvalue problems in quantum mechanics. We first notice that $\hat{\Theta}$ is a linear operator since $\nabla\times$ is a linear operator. This means that a linear combination of two solutions $\alpha\mathbf{H}_1(\mathbf{r}) + \beta\mathbf{H}_2(\mathbf{r})$ is also a solution to the eigenvalue problem. So if we have a solution $\mathbf{H}_1(\mathbf{r})$ then $\alpha\mathbf{H}_1(\mathbf{r})$ is also a solution. For that reason we say that solutions that only differ by a constant multiplier are the same mode.

We will not prove the concepts from quantum mechanics here. A reader unfamiliar with quantum mechanics can refer to a standard textbook like Bransden and Joachain [39].

An important concept is the Hermitian operator. An operator $\hat{\mathbf{A}}$ is Hermitian if

$$< \mathbf{F}|\hat{\mathbf{A}}\mathbf{G} >=< \hat{\mathbf{A}}\mathbf{F}|\mathbf{G} > \tag{2.32}$$

where $< \mathbf{F}|\mathbf{G} >$ is the inner product of $\mathbf{F}$ and $\mathbf{G}$. The eigenvalues of an Hermitian operator are always real and the eigenfunctions can be chosen so that they are normalized and mutually orthogonal. To check if $\hat{\mathbf{\Theta}}$ is Hermitian we do the following

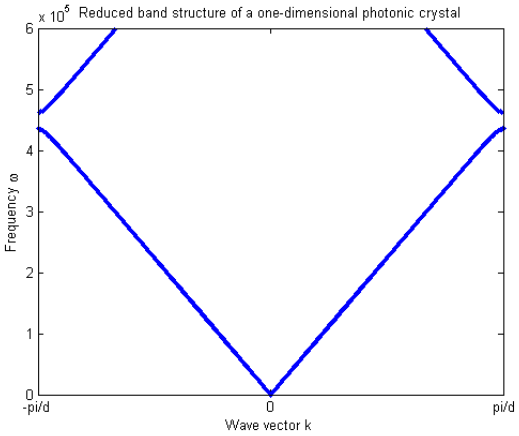

(a) $n_2 = 1.1$

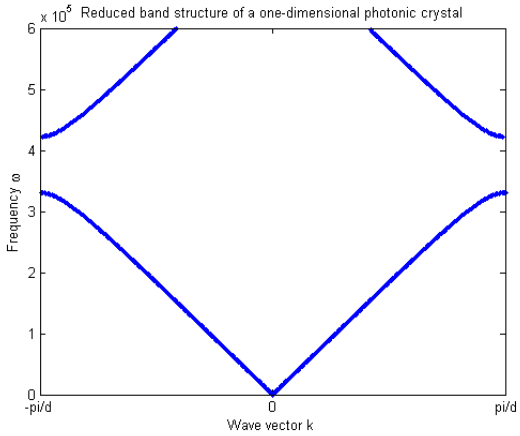

(b) $n_2 = 1.5$

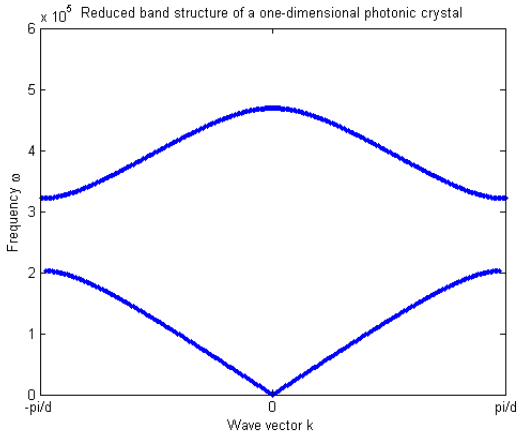

(c) $n_2 = 2.5$

Figure 2.5: The reduced band diagrams for different refractive index contrasts. In all plots $d_1 = d_2 = 1$ and $n_1 = 1$.

$$
\begin{aligned}
< \mathbf{F}|\hat{\mathbf{\Theta}}\mathbf{G} > &= \int d^3\mathbf{r}\mathbf{F}^* \cdot \nabla \times \left(\frac{1}{\epsilon(\mathbf{r})}\nabla \times \mathbf{G}\right) \\
&= \int d^3\mathbf{r}(\nabla \times \mathbf{F})^* \cdot \frac{1}{\epsilon(\mathbf{r})}\nabla \times \mathbf{G} - \int d\mathbf{S}\mathbf{F} \times \mathbf{G} \\
&= \int d^3\mathbf{r}\left[\nabla \times \left(\frac{1}{\epsilon(\mathbf{r})}\nabla \times \mathbf{F}\right)\right]^* \cdot \mathbf{G} - 2\int d\mathbf{S}\mathbf{F} \times \mathbf{G} \\
&= < \hat{\mathbf{\Theta}}\mathbf{F}|\mathbf{G} >
\end{aligned}
\tag{2.33}
$$

This proves that $\hat{\mathbf{\Theta}}$ is Hermitian. In the proof we have used the divergence theorem twice and then neglected the surface terms. We can do this because the fields $\mathbf{F}$ and $\mathbf{G}$ we will look at will either decay to zero at large distances or the fields are periodic in the region of integration.

Now we introduce the electromagnetic variational theorem which is analogous to the variational principle in quantum mechanics. The variational principle in quantum mechanics says that the eigenstate that minimizes the energy is the ground state. The next state is the eigenstate that minimizes the energy while remaining orthogonal to the ground state. The same is true for the electromagnetic variational principle. The lowest frequency mode is the mode given by the eigenstate $\mathbf{H}(\mathbf{r})$ which minimizes the eigenvalue ω^2/c^2 while also fulfilling $\nabla \cdot \mathbf{H} = 0$. Again we use the master equation

$$
\hat{\Theta}\mathbf{H}(\mathbf{r}) = \frac{\omega^2}{c^2}\mathbf{H}(\mathbf{r}) \tag{2.34}
$$

We multiply with $\mathbf{H}(\mathbf{r})$ and integrate, yielding

$$
\begin{aligned}
< \mathbf{H}(\mathbf{r})|\hat{\Theta}\mathbf{H}(\mathbf{r}) > &= \frac{\omega^2}{c^2} < \mathbf{H}(\mathbf{r})|\mathbf{H}(\mathbf{r}) > \\
\frac{\omega^2}{c^2} = U_f(\mathbf{H}) &= \frac{< \mathbf{H}(\mathbf{r})|\hat{\Theta}\mathbf{H}(\mathbf{r}) >}{< \mathbf{H}(\mathbf{r})|\mathbf{H}(\mathbf{r}) >}
\end{aligned}
\tag{2.35}
$$

U_f is called the electromagnetic energy functional. If we insert equation 2.12 into 2.7 and 2.11 into 2.8 we get

$$
\mathbf{H} = \frac{1}{-i\omega\mu_0}\nabla \times \mathbf{E} \tag{2.36}
$$

$$
\nabla \times \mathbf{H} = -i\omega\epsilon_0\epsilon(\mathbf{r})\mathbf{E} \tag{2.37}
$$

From equations 2.33, 2.37 and 2.35 we see that

$$\begin{aligned}\frac{\omega^2}{c^2} < \mathbf{H}(\mathbf{r})|\mathbf{H}(\mathbf{r}) > =< \mathbf{H}|\hat{\Theta}\mathbf{H} >= \int d^3\mathbf{r}(\nabla \times \mathbf{H})^* \cdot \frac{1}{\epsilon(\mathbf{r})}\nabla \times \mathbf{H} = \int d^3\mathbf{r}\frac{1}{\epsilon(\mathbf{r})}|\nabla \times \mathbf{H}|^2 \\ < \mathbf{H}(\mathbf{r})|\mathbf{H}(\mathbf{r}) >= \frac{c^2}{\omega^2}\int d^3\mathbf{r}\frac{1}{\epsilon(\mathbf{r})}(-i\omega\epsilon_0\epsilon(\mathbf{r}))(i\omega\epsilon_0\epsilon(\mathbf{r}))|\mathbf{E}|^2 \\ = \frac{\epsilon_0}{\mu_0}\int d^3\mathbf{r}\epsilon(\mathbf{r})|\mathbf{E}|^2 = \frac{\epsilon_0}{\mu_0} < \mathbf{E}|\epsilon(\mathbf{r})\mathbf{E} >\end{aligned} \tag{2.38}$$

This is inserted in to the energy functional

$$\begin{aligned}U_f(\mathbf{H}) &= \frac{< \frac{1}{-i\omega\mu_0}\nabla \times \mathbf{E}|\nabla \times \left(\frac{1}{\epsilon(\mathbf{r})}(-i\omega\epsilon_0\epsilon(\mathbf{r}))\mathbf{E}\right) >}{\frac{\epsilon_0}{\mu_0} < \mathbf{E}|\epsilon(\mathbf{r})\mathbf{E} >} \\ &= \frac{\frac{\epsilon_0}{\mu_0} < \nabla \times \mathbf{E}|\nabla \times \mathbf{E} >}{\frac{\epsilon_0}{\mu_0} < \mathbf{E}|\epsilon(\mathbf{r})\mathbf{E} >} \\ &= \frac{\int d^3\mathbf{r}|\nabla \times \mathbf{E}|^2}{\int d^3\mathbf{r}\epsilon(\mathbf{r})|\mathbf{E}|^2}\end{aligned} \tag{2.39}$$

We see that U_f is minimized when the field is concentrated in the areas with high $\epsilon(\mathbf{r})$ and when the amount of spatial oscillations is low. The allowed fields in the crystal need to have the same symmetry as the crystal. At the band gap at the Brillouin zone edge there are two possible ways to place the field nodes of a solution with wavelength $2a$, where a is the period, or the lattice constant, of the crystal. In the center of the areas with low index or in the center of the areas with high contrast (fig. 2.6). These two field configurations are orthogonal to each other as required and have the same amount of spatial oscillations. The solution with the nodes in the low index material will have lower U_f because of a higher field strength in the high index layers. From equation 2.35 we see that a lower U_f gives a lower frequency ω. The other solution will have a higher U_f due to having higher field strength in the low index material and thus a higher frequency ω. This difference in ω creates a frequency gap between the two solutions at that k-point. The size of the gap will grow when the refractive index difference increases because the U_f difference will grow. This matches what we found in section 2.1.1.

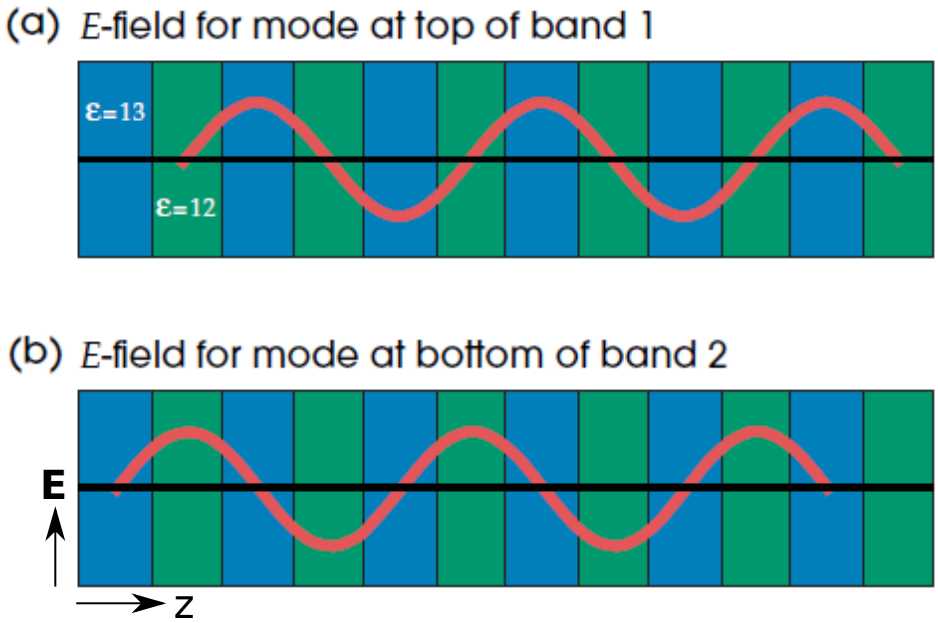

Figure 2.6: In (a) the nodes are centered in the low index material and therefore have most of its energy confined in the high index material. In (b) the situation is reversed with the nodes in the high index material and most of its energy is confined in the low index material. Figure taken from Joannopolous et al. [35]

2.2 Waves in a photonic crystal

A mode with a frequency allowed in the crystal is called an extended state. This mode will have a real wave vector k. However a wave with a frequency in the band gap will have a complex k. The wave will then decay exponentially in the crystal with a decay constant $Im\{k\}$. These modes are called evanescent modes [35, p. 52].

A wave propagating in the crystal will couple to a possible wave vector. The frequency has to be conserved in a linear medium, but the k-vector can change. A wave with frequency ω will thus couple to the k-vector allowed for that ω.

In a band diagram the region above a gap is sometimes referred to as the air band and the region below as the dielectric band. This is because the modes above the gap have more of its energy concentrated in the low refractive index materials while the modes below have more energy in the high refractive index materials. In two and three-dimensional photonic crystals the low refractive index material is usually air, therefore the name air band [35, p. 47].

2.3 Origin of the band gap

When finding the band structure we used the Bloch theorem which assumes an infinite crystal. We can study a non-infinite periodic crystal to see the origin of the band gap. Again we use matrix formalism

$$\begin{bmatrix} u_{out}^{+} \\ u_{out}^{-} \end{bmatrix} = M_{tot} \begin{bmatrix} u_{in}^{+} \\ u_{in}^{-} \end{bmatrix}, \tag{2.40}$$

$$M_{tot} = M_{(N-1)N} M_{prop(N-1)} \dots M_{12} M_{prop1} M_{01} \tag{2.41}$$

where M_{nm} is the transfer matrix from layer n to layer m from equation 2.25 and M_{propn} is the propagation matrix through layer n described in equation B.11.

In figure 2.7 we can see the transmission plotted for different numbers of layers (N equal 10, 20 and 100). As the number of layers increases the reflectance peaks get flatter and we see that the photonic band gaps appear. The origin of the band gap is therefore no unknown effect, only constructive and destructive interference from reflection and transmission. We also observe that the transmission is not necessarily 1 outside the band gap.

Even though the math behind photonic crystals assume that the crystal is infinite we see that there is a clear formation of a band with very low transmission, even with a finite crystal.

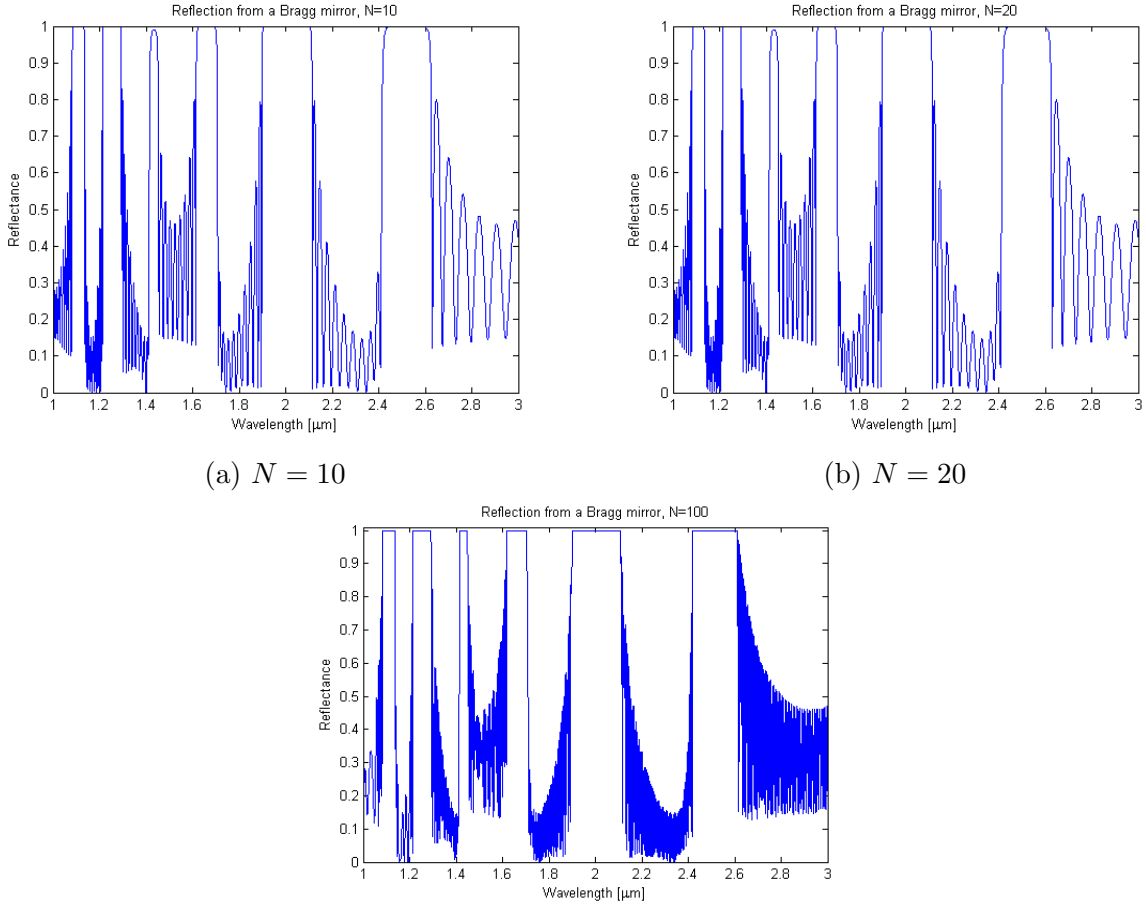

(a) $N = 10$

(b) $N = 20$

(c) $N = 100$

Figure 2.7: Reflectance in a Bragg mirror for various numbers of layers N. The refractive index of layer one is $n_1 = 1.5$ and for the second layer $n_2 = 3.5$.

2.4 Two-dimensional photonic crystals

In a two dimensional photonic crystal there is a periodic variation in the refractive index in two dimensions while the refractive index remains constant in the third dimension. A photonic band gap will appear in the plane of periodicity, for either some or all directions in the plane.

To find the band structure we again turn to the master equation (eq. 2.13). As the structures get more complex finding exact solutions to the master equation quickly becomes impossible. Therefore only numerical solutions given by the freely available computer software MIT Photonic-Bands [40] will be presented. The solutions are based on the same principles as for the one dimensional structure, now with two dimensional Bloch waves. The

solutions are therefore for a structure that is infinitely periodical in two dimensions and infinitely constant in the third.

As with propagation through other two dimensional structures the solutions can be split in to two polarizations, TE and TM. For TE polarization $\mathbf{H}$ is normal to the plane and $\mathbf{E}$ is in the plane. If the plane of periodicity is the xy plane then $\mathbf{H}(\mathbf{r}) = H(\mathbf{r})\hat{\mathbf{z}}$ and $\mathbf{E}(\mathbf{r}) \cdot \hat{\mathbf{z}} = 0$. The situation is reversed for the TM polarization with $\mathbf{E}$ normal to the plane and $\mathbf{H}$ in the plane.

The band structures for the two different polarizations are usually very different. There are a lot of different structures one can imagine, but here we will only treat square and hexagonal structures.

2.4.1 Square lattice

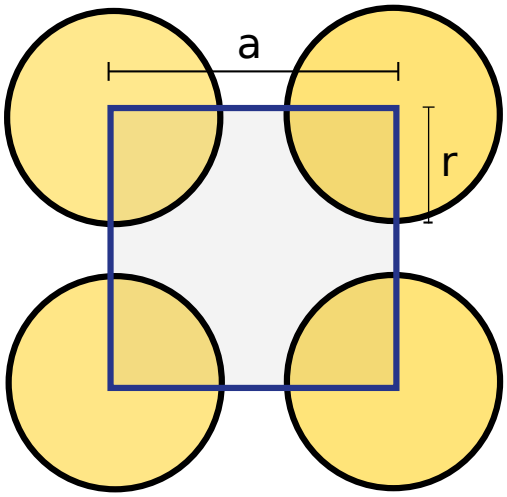

(a) The structure of a square lattice with the unit cell marked with a blue square. a is the lattice constant and r is the cylinder radius.

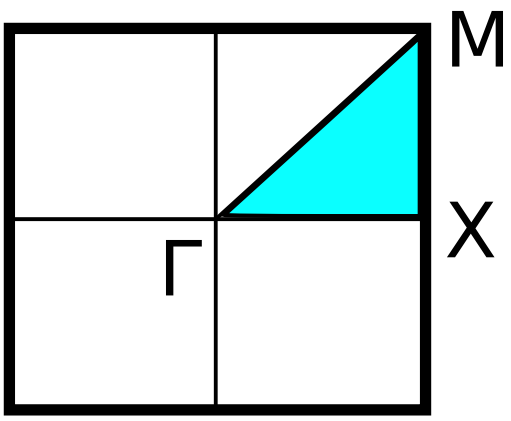

(b) The Brillouin zone with the irreducible zone marked in blue and Γ, X and M point marked.

Figure 2.8: A square lattice structure.

In figure 2.8a a square lattice is shown. In this case there are cylindrical areas with a different refractive index than the surrounding material. r is the radius of the cylinders and a is the lattice constant. The unit cell is marked with a blue square. In figure 2.8b the Brillouin zone is shown.

We begin by looking at a structure of silicon rods in air. Since the master equation is scale invariant, we only need to specify the relative length, r/a. In this case $r/a = 0.25$. The silicon is given a relative permittivity $\epsilon = 12$ and air $\epsilon = 1$. The resulting band structure

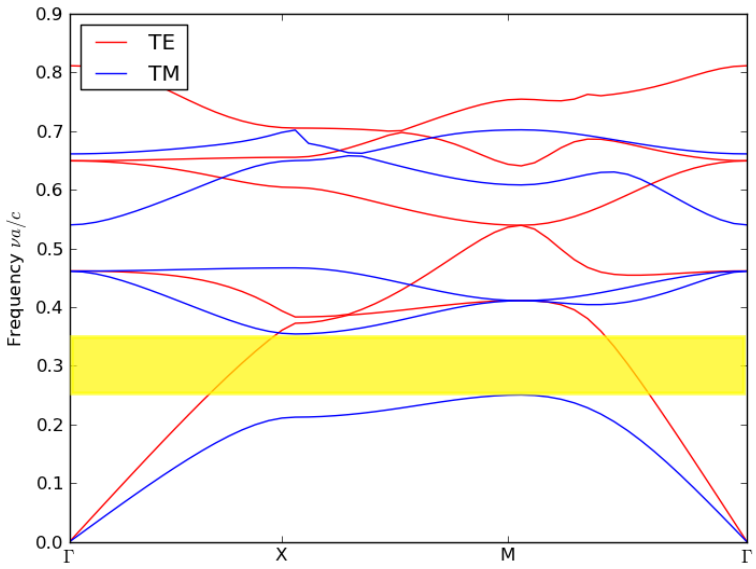

Figure 2.9: The five lowest TE and TM modes of a square lattice of Si rods in air. The lowest photonic gap is marked with yellow.

can be seen in figure 2.9. As with the one dimensional structure, we only need to look at the irreducible zone to know the band structure everywhere. We follow the edges of the irreducible Brillouin zone from the Γ point to X to M and back to Γ again. The reason the interior of the Brillouin zone is not plotted is that the minima and the maxima almost always appear at the zone edges. This is true for all the structures discussed here [35, p. 68]. The y-axis is given in normalized frequency because we only defined the ratio r/a and not r and a. Therefore the plot will be correct for all structures where $r/a = 0.25$. If a lattice constant a is given then the blocked frequencies ν are

$$\nu = \frac{\omega}{2\pi} = \frac{\nu_n c}{a} \tag{2.42}$$

where ν_n is the normalized frequency. For this structure there is a complete band gap for the TM polarization between the first and the second mode. A complete band gap means that there is a band of frequencies which are not allowed to propagate through the crystal for any k-vector in the plane. There is no complete band gap for the TE polarization.

We can also look at the case with air holes in silicon (fig. 2.10). In this case there is no photonic band gap for either polarization. This means that a two dimensional periodic structure does not need to have a complete band gap.

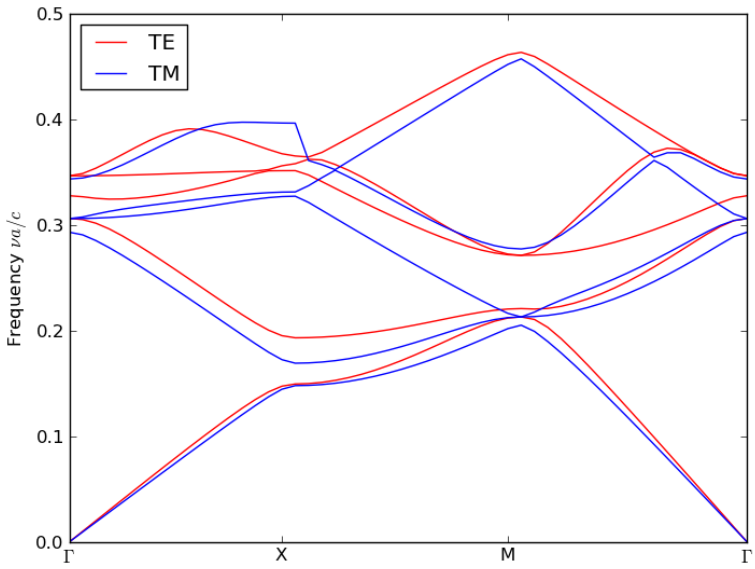

Figure 2.10: The five lowest TE and TM modes of a square lattice of air holes in Si.

2.4.2 Hexagonal lattice

Another possible structure is a hexagonal arrangement of circles with different refractive index than the surroundings (fig. 2.11a). The corresponding Brillouin zone is shown in figure 2.11b defined by the points Γ, M and K. In figure 2.12 we can see the band structure for hexagonal air holes in Si with $r/a = 0.25$.

This structure has a complete band gap for TE polarization. We see that this structure has a TE band gap, while the square lattice of Si columns in air gave a TM band gap. In general a TM band gap is favored in a structure with isolated high ϵ regions, and TE band gaps are favored in a structure where the high ϵ areas are connected [35, p. 75]. However, it is possible to make structures that have overlapping TE and TM gaps like the one in figure 2.13. In this structure of air holes in Si with $r/a = 0.48$ the Si areas are connected which promotes a TE band gap, but only barely connected which gives rise to a TM band gap at the same time.

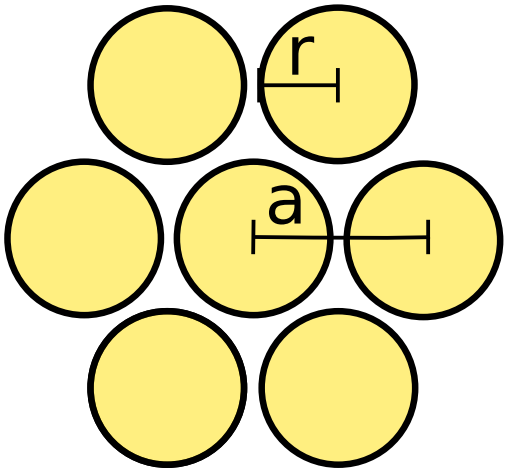

(a) The structure of a hexagonal lattice. a is the lattice constant and r is the cylinder radius.

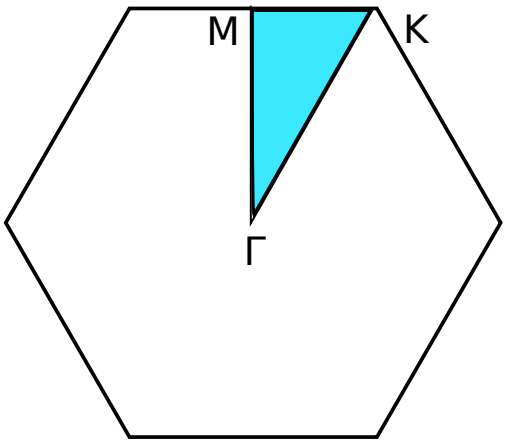

(b) The Brillouin zone with the irreducible zone marked in blue and defined by Γ, M and K.

Figure 2.11: A hexagonal lattice structure.

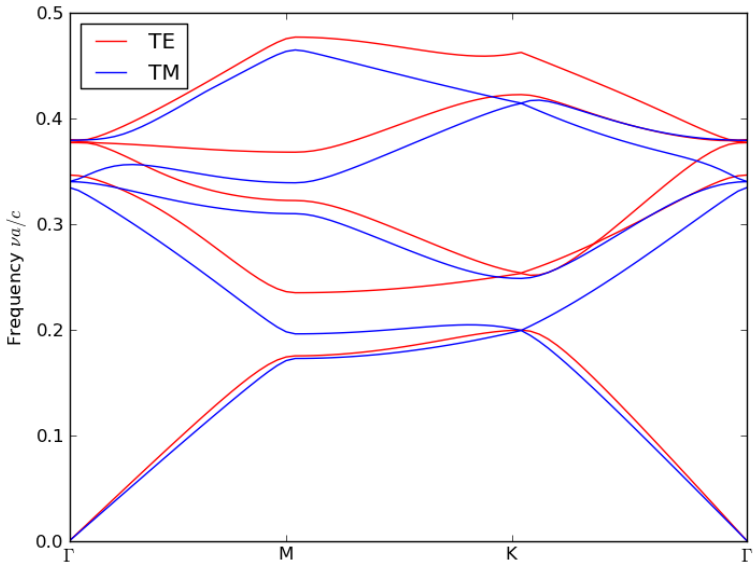

Figure 2.12: The five lowest TE and TM modes of a hexagonal lattice of air holes in Si.

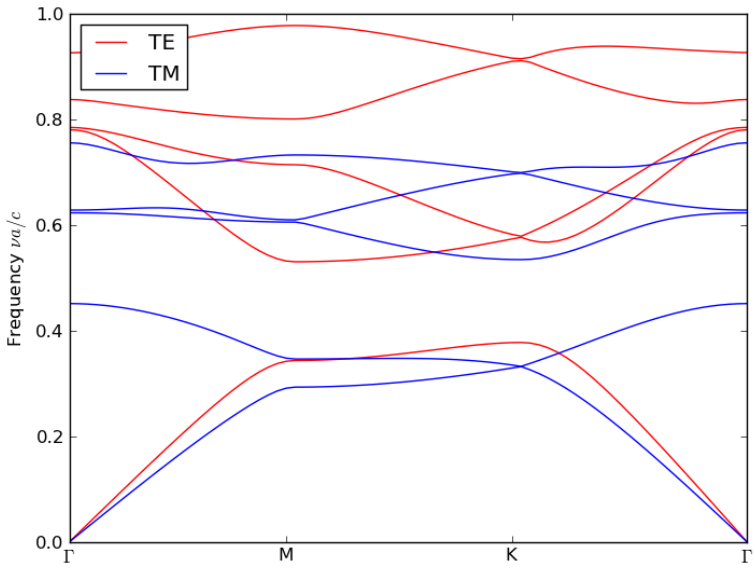

Figure 2.13: The five lowest TE and TM modes of a hexagonal lattice of air holes in Si with $r/a = 0.48$.

2.5 Photonic crystal slabs

Until now we have looked at two dimensional structures which are infinite in the third dimension. However, this is not realizable practically, the third dimension has to be limited to some finite length, which introduces new behavior. These structures are called photonic crystal slabs. The light is affected by the periodicity in two dimensions (x,y) while being index guided in the third (z) due to the difference in refractive index between the photonic crystal and the surroundings.

This section is based on Joannopolous et al. [35, ch. 8] where not otherwise specified. We will mainly look at silicon slabs with air holes, however most of the general knowledge presented here will be correct for slabs of rods in air.

First, we will look at a slab suspended in air as seen in figure 2.15. The in-plane vector $\mathbf{k}_{||} = (k_x, k_y)$ will be conserved due to the periodicity in x and y, while k_z will not be conserved. Normally, the modes of a three dimensional structure cannot be divided in to TM and TE polarizations, however for thin structures with mirror symmetry modes will be mostly polarized. At the mirror plane the modes will be purely polarized, and near the plane the fields will be mostly like a TE or TM mode as seen in figure 2.14. Then the modes can be classified as TE-like or TM-like. The fields will be less TM or TE like as we move away from the symmetry plane, therefore it is important that the slab is thin, with thickness

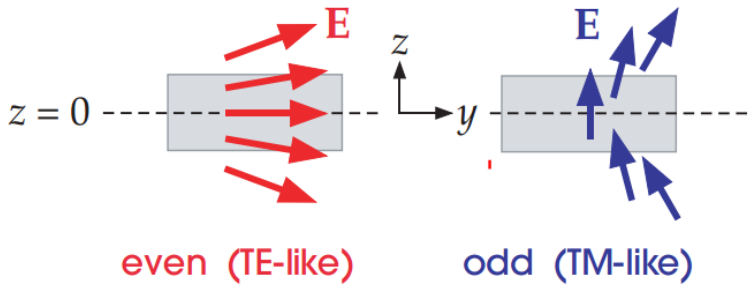

Figure 2.14: The electric field lines in a thin structure with mirror symmetry around $z = 0$. The fields are polarized at $z = 0$ and almost polarized around the symmetry plane. Figure taken from Joannopolous et al. [35].

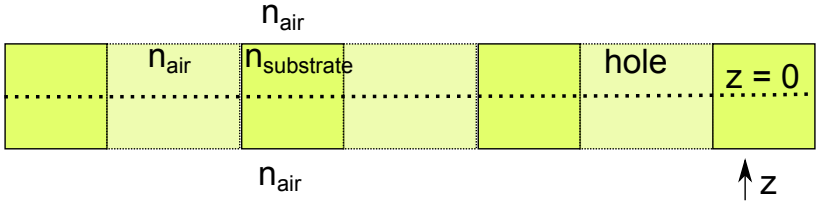

Figure 2.15: Cross section of a symmetric slab with refractive index $n_{substrate}$ suspended in air.

smaller than the wavelength. The system in figure 2.15 is invariant under reflections around the $z = 0$ plane, which means that the modes can be classified as either TE-like or TM-like modes. The band diagram can be plotted as before, but now we plot the frequency ω versus the in-plane wave vector $k_{||}$.

When looking at photonic crystal slabs we have to introduce the light cone. There are a continuum of states that extend infinitely in to the region outside the slab above the light line, the line defining the light cone. States in the band structure above the light line will not be confined to the slab, but radiate out to the background. The states below the light line are the only states of interest to us. These states are infinitely extended in the plane of the slab and decay exponentially in to the background. The confinement below the light line is analogous to total internal reflection, as it is created by the experienced higher refractive index in the slab by the light [41]. The placement of the light line depends on the material surrounding the slab and is given by $\omega = c/n\sqrt{k_{||}^2 + k_y^2}$, with $n = \sqrt{\epsilon}$. Since we are only looking at the in-plane wave vectors this reduces to $\omega = c/n|k_{||}|$. The values of $k_{||}$ can be found by using solid state physics knowledge and the Brillouin zone. We start with the basis vectors of the hexagonal structure as seen in figure 2.16a. One representation of the basis vectors are given by

$$\begin{aligned} \mathbf{a_1} &= 0.5a\mathbf{x} + \frac{\sqrt{3}}{2}a\mathbf{y} \\ \mathbf{a_1} &= 0.5a\mathbf{x} - \frac{\sqrt{3}}{2}a\mathbf{y} \end{aligned} \tag{2.43}$$

In a two-dimensional system, the reciprocal vectors $\mathbf{b_1}$ and $\mathbf{b_2}$ can be found by using

$$\begin{aligned} \mathbf{a_i} \cdot \mathbf{b_i} &= 2\pi \\ \mathbf{a_i} \cdot \mathbf{b_j} &= 0 \end{aligned} \tag{2.44}$$

where i, j are 1 or 2. This yields

$$\begin{aligned} \mathbf{b_1} &= 2\pi\left(\frac{1}{a}\mathbf{k_x} + \frac{1}{\sqrt{3}a}\mathbf{k_y}\right) = \frac{4\pi}{\sqrt{3}a}\left(\frac{\sqrt{3}}{2}\mathbf{k_x} + 0.5\mathbf{k_y}\right) \\ \mathbf{b_2} &= 2\pi\left(\frac{1}{a}\mathbf{k_x} - \frac{1}{\sqrt{3}a}\mathbf{k_y}\right) = \frac{4\pi}{\sqrt{3}a}\left(\frac{\sqrt{3}}{2}\mathbf{k_x} - 0.5\mathbf{k_y}\right) \end{aligned} \tag{2.45}$$

which also is a hexagonal lattice, rotated 30 degrees relative to the real lattice. By drawing lines that are equally spaced between one element of the lattice and the next, we construct the Brillouin zone. The reciprocal lattice and the Brillouin zone is shown in figure 2.16c.

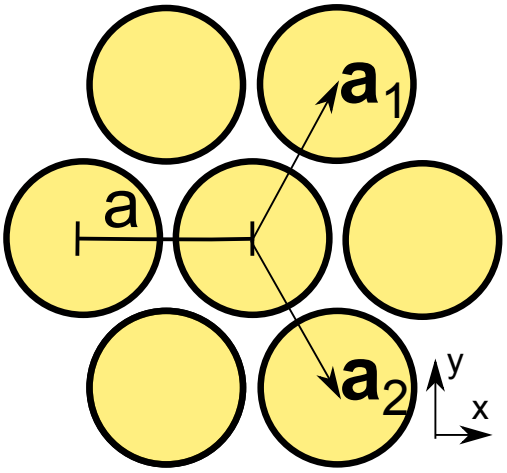

(a) The structure of a hexagonal lattice. a is the lattice constant $\mathbf{a_1}$ and $\mathbf{a_2}$ are the basis vectors.

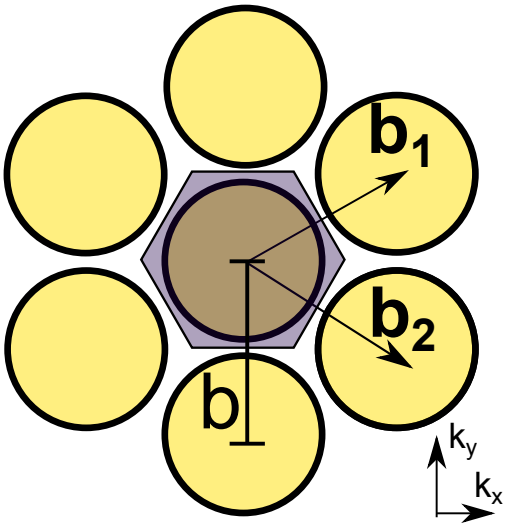

(b) The reciprocal lattice with the reciprocal lattice vectors $\mathbf{b_1}$ and $\mathbf{b_2}$ and the lattice constant $b = \frac{4\pi}{\sqrt{3}a}$. The Brillouin zone is marked in purple.

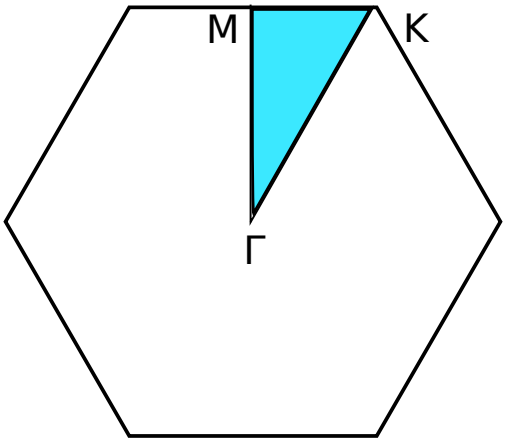

(c) The Brillouin zone with the symmetry points Γ, M and K marked.

Figure 2.16: A hexagonal lattice structure.

The reciprocal lattice vectors enable us to find the value of $|k_{||}|$ at the symmetry points and the lines connecting them. For example the M-point is located half way between two lattice points. This gives $|k_{||}| = 2\pi/(\sqrt{3}a)$, $\omega = c/n2\pi/(\sqrt{3}a)$. Converting this in to normalized frequency gives $\nu_n = 1/(\sqrt{3}n)$. A higher refractive index of the materials surrounding the slab will result in a lower light line and therefore fewer guided modes.

The photonic band structure for a silicon slab in air, with relative permittivities as in previous sections, is plotted in figure 2.17. The holes have a relative radius of $r/a = 0.25$ and the relative thickness of the silicon slab is $d/a = 0.5$. This structure is made with MPB as the band structures in previous sections. Since MPB requires periodicity, a supercell of one slab unit with surrounding material and a hole is created. In this case first a block of air, then a block of Si with an air hole, and then an air block again. This supercell is repeated infinitely in all directions and a dispersion relation is calculated. The resulting structure will be correct in the plane of the slab, but unrealistic in the z-direction. Thus we need enough vertical space between each sequence of slabs to ensure that the confined modes are not affected noticeably. The non-confined modes will be affected, but this is disregarded as they fall above the light line and are therefore uninteresting to us. This method has been used in several published articles [41, 42, 43, 44, 45].

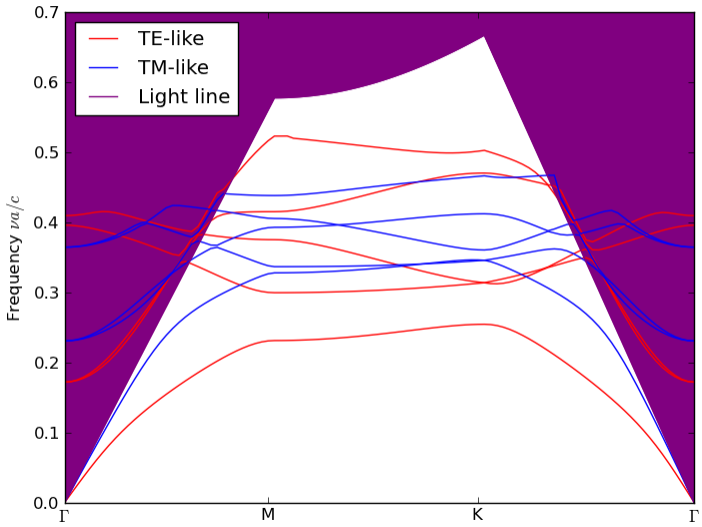

Figure 2.17: The five lowest bands for a silicon slab of holes in a hexagonal lattice suspended in air with relative radius 0.25 and relative thickness of 0.5.

A photonic crystal slab suspended in air can be difficult to realize. Placing it on a dielectric substrate makes it easier to fabricate, but also removes the mirror symmetry at $z = 0$, creating asymmetric slabs. This results in that the modes can no longer be classified

as TE-like or TM-like and there is no longer a photonic band gap [41]. However, if the refractive index difference between the photonic crystal and substrate is large, then the modes will largely be confined to the slab and create a photonic band gap [42, 45]. A plot of the band structure for the photonic crystal slab from figure 2.17 on a substrate with relative permittivity of $\epsilon = 2.14$ is shown in figure 2.18.

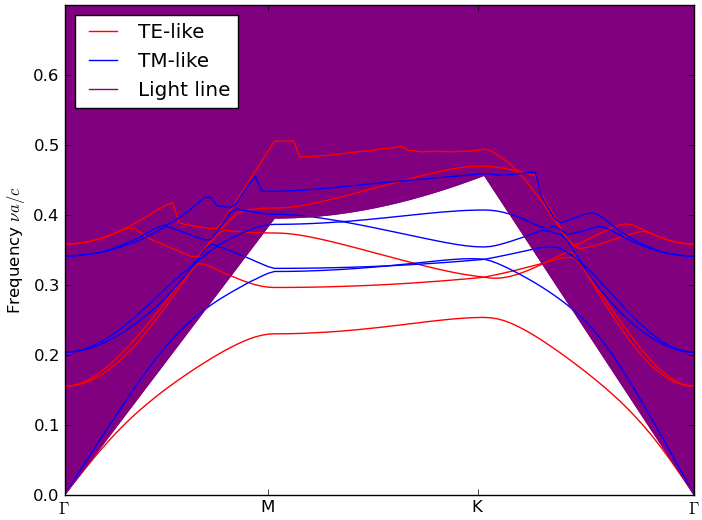

Figure 2.18: The five lowest bands for a silicon slab of holes in a hexagonal lattice on a substrate ($\epsilon = 2.14$) with relative radius 0.25 and relative thickness of 0.5.

In asymmetric slabs, the TM-like and TE-like modes will couple and become leaky. For silicon on SiO_2, numerical simulations have shown that this coupling effect is very small and meaningful photonic band gaps can be produced [46, p. 68]. The effect of the leakage can also be reduced by etching the holes in to the substrate material. This will also produce larger gaps [41, 42, 45]. This is confirmed by simulations done in MPB shown in figure 2.19. The difference between the two band structures are difficult to discern, but in the second band structure all the modes, except the lowest order TE mode, are slightly lifted, creating a larger gap.

The size of the band gap is dependent on the slab thickness. For very thin slabs the modes will be very weakly guided and extend greatly in to the background, making the periodicity less important and therefore the gap will be reduced. A very thick slab will approach the infinite two dimensional crystal and higher order modes will be pulled down and populate the gap. The optimal slab thickness is dependent on the polarization of the gap, with TE gaps preferring thinner slabs than TM gaps.

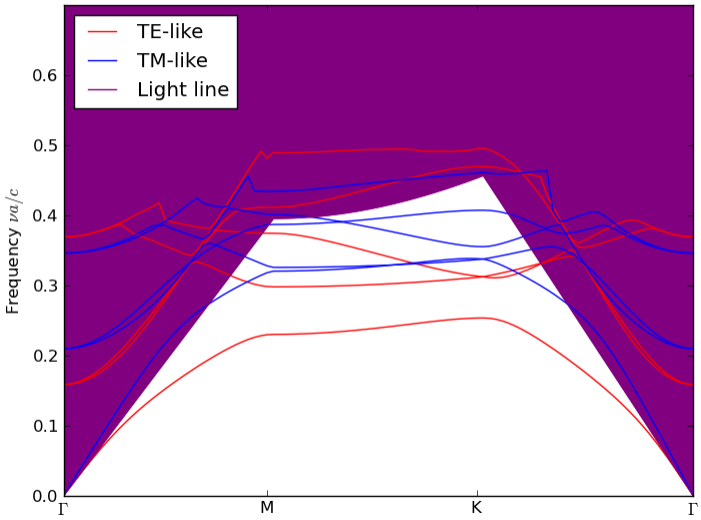

Figure 2.19: The five lowest bands for a silicon slab of holes in a hexagonal lattice on a substrate ($\epsilon = 2.14$) with relative radius 0.25 and relative thickness of 0.5.

2.6 Defects

Many interesting properties appear when defects are introduced in to the photonic crystal [1, 35]. A defect is introduced if one of the units in the crystal is different from the rest. For example in a one-dimensional crystal one layer can be thicker or narrower than the other layers. For the frequencies that are in the band gap this structure will be like two mirrors on both sides of the defect. Waves with wavelength $\lambda = 2Ln/m$, where L is the defect layer length, n the refractive index, and m an integer, will experience constructive interference and the result is a Fabry-Perot etalon [36, p. 254]. These wavelengths will be transmitted 100% through the crystal even though it is in the band gap. It is evident from this that a defect can introduce an allowed state that would otherwise be forbidden in the band gap.

A defect can also be introduced if one unit has a different refractive index. In two-dimensional crystals a rod or hole can be bigger or smaller than the rest or be a different material. It is called a point defect when only one site is perturbed. This gives rise to a localized state where light can be trapped. A wave with frequency in the band gap hitting the crystal will normally be reflected, but an evanescent tail will extend in to the crystal and decay exponentially. If this wave has the same frequency as the new state created by the defect the evanescent tail can couple in to the defect and create a strong field around the defect which can then couple out again on the other side of the crystal. This is the effect that will be utilized in the sensor in this project. If the defect size or the size of the

surrounding units changes, then the position of the new state would also change, resulting in the transmission peak shifting to a different wavelength [1]. A defect that traps the light in this manner can also be called a cavity.

When a defect is introduced, it does not make sense to include it in the plot of the dispersion relation. The symmetry is broken and therefore the dispersion relation cannot be accurate. We get the k in the dispersion equation from the Bloch wave that assumes infinite periodicity. The density of states (DoS) gives the number of allowed states per unit frequency. For the frequencies in the band gap the DoS will be zero. A defect will make new DoS peaks for the supported frequencies, which can be in the band gap [35, ch. 4].

2.6.1 Temporal Coupled-Mode Theory

To investigate the effect of defects we can use temporal coupled-mode theory. This section will follow Joannopolous et al. [35, ch. 10]. In this theory there are only two building blocks in this theory, propagating modes and localized modes. Propagating modes are supported in a waveguide and localized modes in a resonant cavity. The results are described by the frequency of the wave and the decay time of the field in the defect which must be determined in some other way. The theory makes certain assumptions, the first one being that we assume a monochromatic wave. The second is that the cavity is weakly coupled to the surroundings, i.e. that it has a large decay time. We also assume linearity which means that that non-linear effects do not occur and the frequency stays constant. Conservation of energy is assumed and it is assumed that the material and geometry properties stay constant over time. The last assumption is time-reversal invariance which means that reversing the sign of time gives the same events in reversed order.

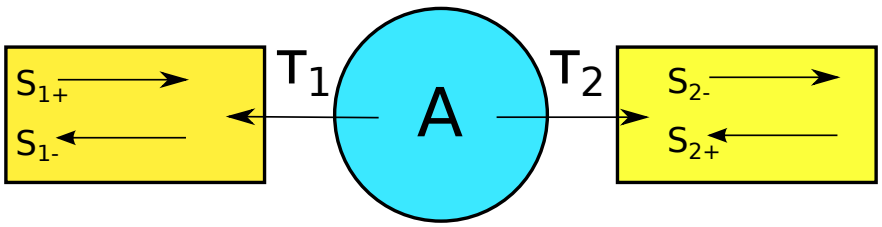

Figure 2.20: A schematic figure of a system with an input waveguide, a photonic crystal with a cavity, and an output waveguide. The input waveguide has S_{1+} as the incoming field and S_{1-} as the outgoing field, the photonic crystal has a cavity with a field proportional with A and decay time into the two waveguides of τ_1 and τ_2, and the output waveguide has S_{2+} as the incoming field and S_{2-} as the outgoing field.

Most relevant to this project is the case of a crystal with a point defect. An input single mode waveguide on one side guides the light towards the crystal and an output single mode waveguide on the other side guides the light away from the crystal. This is shown in figure

2.20. In both waveguides there are incoming (S_{1+} and S_{2+}) and outgoing fields (S_{1-} and S_{2-}). The field in the resonant defect is proportional to A and has a decay time of τ_1 and τ_2 in to the respective waveguides. This means that the field strength decays with $e^{-t/\tau}$. The cavity will have one resonant frequency ω_0.

By using these assumptions and the assumption that we only have an incoming field from one side (this is the case with the sensor investigated in this project) we end up with a transmission given by

$$T(\omega) = \frac{|S_{2-}|^2}{|S_{1+}|^2} = \frac{\frac{4}{\tau_1\tau_2}}{(\omega-\omega_0)^2 + \left(\frac{1}{\tau_1}+\frac{1}{\tau_2}\right)^2} \tag{2.46}$$

The details of the derivation of this transmission can be found in appendix C. This gives a transmission of 1 when we are at the resonant frequency ($\omega = \omega_0$) and the decay times are equal ($\tau_1 = \tau_2$). The last requirement is true when the structure is symmetric.

2.6.2 Analysis of defect modes using group theory

A simple analysis of the defect modes in photonic crystal and the effects of faults in the lattice can be made using symmetry analysis. This section is mainly based on Painter and Srinivasan [47], Painter et al. [48], and Painter [49], and will not be a comprehensive introduction to group theory and symmetry. Analysis using group theory is more commonly used in quantum mechanics and solid state physics, but again knowledge can be gained from those fields and be applied to photonic crystals. We will study a two dimensional photonic crystal of air holes in a solid substrate and only look at TE modes, as only TE modes have a band gap in the structure used in this work. In section 2.4.2 it is shown that the band gap forms from the lowest order mode, therefore the analysis uses the fundamental magnetic field vector of an unpatterned slab waveguide, $\mathbf{B}_{\mathbf{k}_\perp}(\mathbf{r}_\perp) = \hat{z}e^{-(\mathbf{k}_\perp \cdot \mathbf{r}_\perp)}$ as the seed vector, where $\mathbf{k}_\perp$ is the wave vector in the plane of the crystal and $\mathbf{r}_\perp$ is an in-plane coordinate.

Both the real and reciprocal space of the hexagonal structure has C_{6v} symmetry. We can see this from the operations that transform the structure in to a state indistinguishable from the original. The first operation is the identity operation E which leaves the system unchanged. There are three different kinds of rotations around a lattice point that all leave the system indistinguishable from the first, C_2 (rotation 180 degrees), C_3 (rotation 120 degrees), and C_6 (rotation 60 degrees). Rotating the system 120 degrees, 240 degrees and 360 degrees are all C_3 rotations. However, the 360 degree rotation is essentially the same as not rotating at all, thus we are left with two unique C_3 rotations. We can do 6 C_6 rotations before returning to the original system. Most of these rotations are already covered by the previously discussed rotations, giving two unique C_6 rotations (60 degrees and 300 degrees). In addition to the rotations, there are planes which mirror the system. These are classified

as σ_d and σ_v, with three unique planes for both. The mirror planes are marked with dashed lines in figure 2.21.

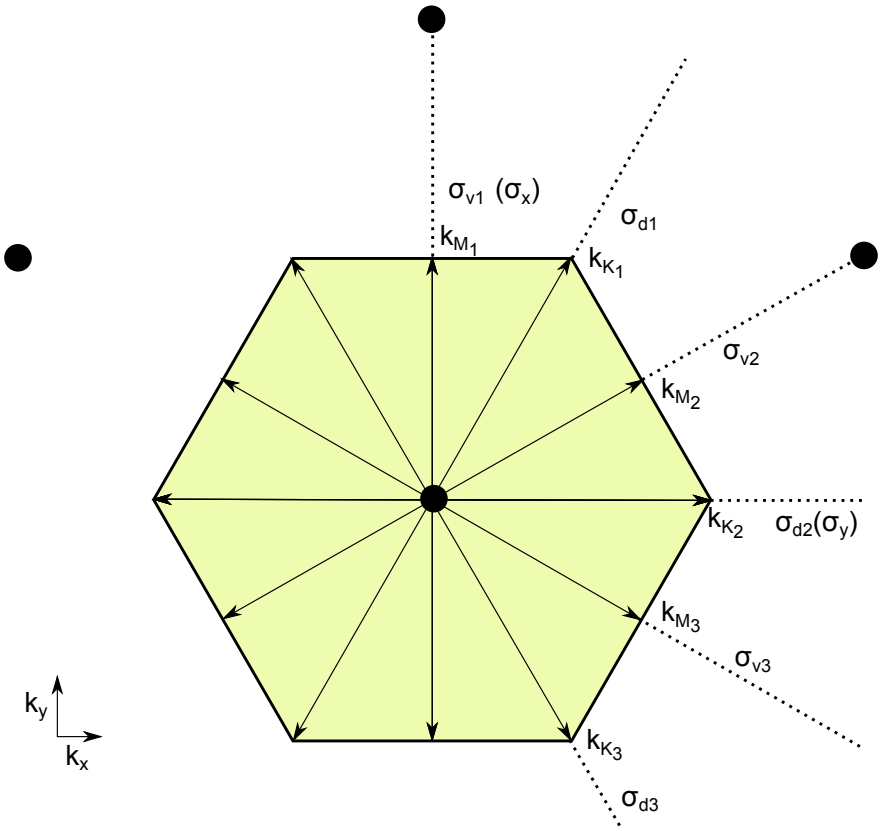

Figure 2.21: An illustration of the Brillouin zone of a hexagonal structure with k vectors from the origin M- and K-points, and mirror planes σ marked. Some of the lattice points are indicated with black circles.

In this analysis we will only look at the modes at the M-point because this is the lowest point of the air band for this structure. When introducing defects that reduces the area with low refractive index, i.e. making a hole smaller, a state gets pulled down from the bottom of the air band [35, ch. 4], in this case at the M-point.

The wavevector at the M-point, k_M has a C_{2v} symmetry. The vector cannot be rotated by 120 or 60 degrees and still remain indistinguishable, but can be rotated 180 degrees. In addition to applying the identity operator the vector can be mirrored through two planes σ_x and σ_y. The symmetry basis for the modes can be found by applying these operations to the seed vector $\mathbf{B}_{\mathbf{k}_{M_1}}$. $E\mathbf{B}_{\mathbf{k}_{M_1}}$ leaves $\mathbf{B}_{\mathbf{k}_{M_1}}$ unchanged. Rotating 120 degrees gives $\mathbf{B}_{-\mathbf{k}_{M_1}}$, mirroring through σ_x gives $\mathbf{B}_{\mathbf{k}_{M_1}}$. Lastly mirroring through σ_y gives $\mathbf{B}_{-\mathbf{k}_{M_1}}$, resulting in two basis vectors, $\mathbf{B}_{\mathbf{k}_{M_1}}$ and $\mathbf{B}_{-\mathbf{k}_{M_1}}$.

Table 2.1: Point group character table for C_{2v}.

C_{2v}	E	C_2	σ_x	σ_y
A_1	1	1	1	1
A_2	1	1	-1	-1
B_1	1	-1	-1	1
B_2	1	-1	1	-1

The character table of the irreducible representation (IRREP) space of C_{2v} is shown in table 2.1 [50]. To find the projection of the basis on to an IRREP we multiply the character of the IRREP with the result of the same symmetry operation on the seed vector and add them together.

$$\begin{aligned}
&\mathbf{B}_{\mathbf{k}_{M_1}} + \mathbf{B}_{-\mathbf{k}_{M_1}} + \mathbf{B}_{\mathbf{k}_{M_1}} + \mathbf{B}_{-\mathbf{k}_{M_1}} = 2\mathbf{B}_{\mathbf{k}_{M_1}} + 2\mathbf{B}_{-\mathbf{k}_{M_1}} = \hat{z}cos(\mathbf{k}_{M_1} \cdot \mathbf{r}_\perp) \\
&\mathbf{B}_{\mathbf{k}_{M_1}} + \mathbf{B}_{-\mathbf{k}_{M_1}} - \mathbf{B}_{\mathbf{k}_{M_1}} - \mathbf{B}_{-\mathbf{k}_{M_1}} = 0 \\
&\mathbf{B}_{\mathbf{k}_{M_1}} - \mathbf{B}_{-\mathbf{k}_{M_1}} - \mathbf{B}_{\mathbf{k}_{M_1}} + \mathbf{B}_{-\mathbf{k}_{M_1}} = 0 \\
&\mathbf{B}_{\mathbf{k}_{M_1}} - \mathbf{B}_{-\mathbf{k}_{M_1}} + \mathbf{B}_{\mathbf{k}_{M_1}} - \mathbf{B}_{-\mathbf{k}_{M_1}} = 2\mathbf{B}_{\mathbf{k}_{M_1}} + 2\mathbf{B}_{-\mathbf{k}_{M_1}} = \hat{z}sin(\mathbf{k}_{M_1} \cdot \mathbf{r}_\perp)
\end{aligned} \tag{2.47}$$

We are not interested in the magnitude, therefore any multiplicative constant is omitted. This yields the projection of the basis on to the IRREP spaces

$$\begin{aligned}
\mathbf{B}_{A_1}^{M_1} &= \hat{z}cos(\mathbf{k}_{M_1} \cdot \mathbf{r}_\perp) \\
\mathbf{B}_{B_2}^{M_1} &= \hat{z}sin(\mathbf{k}_{M_1} \cdot \mathbf{r}_\perp)
\end{aligned} \tag{2.48}$$

The structure has an air hole at the origin and in section 2.1.2 it was stated that the lowest order mode has its electrical field concentrated in the high refractive index areas. Since the electric and magnetic field generally will be spatially offset, this results in the magnetic field concentrating in low refractive index for the fundamental mode. $\mathbf{B}_{B_2}^{M_1}$ is 0 at the origin and corresponds to the air band mode and $\mathbf{B}_{A_1}^{M_1}$ corresponds to the dielectric band mode. There are two additional unique M-points, M_2 and M_3 which yield similar results when projected on to C_{2v}. The result is a set of degenerate air band modes

$$A\mathbf{B}_{B_2}^{M} = \hat{z} \begin{bmatrix} sin(\mathbf{k}_{M_1} \cdot \mathbf{r}_\perp) \\ sin(\mathbf{k}_{M_2} \cdot \mathbf{r}_\perp) \\ sin(\mathbf{k}_{M_3} \cdot \mathbf{r}_\perp) \end{bmatrix} \tag{2.49}$$

The dielectric band modes have a similar set of modes, but are not shown because the defect mode is formed from the air band mode.

When a hole is made smaller the translational symmetry is lost and only the C_{6v} symmetry of the defect is retained. Thus we need to find the characters of the representation of the $A\mathbf{B}_{B_2}^{M}$ basis under the operations of C_{6v}. The characters of the representation are the traces of the transformation matrices that perform the operations in C_{6v} on the basis. For example for the the E operator we need to solve the following equation

$$EA\mathbf{B}_{B_2}^{M_1} = E\hat{z}\begin{bmatrix} sin(\mathbf{k}_{M_1}\cdot\mathbf{r}_\perp) \\ sin(\mathbf{k}_{M_2}\cdot\mathbf{r}_\perp) \\ sin(\mathbf{k}_{M_3}\cdot\mathbf{r}_\perp) \end{bmatrix} = \hat{z}\begin{bmatrix} sin(\mathbf{k}_{M_1}\cdot\mathbf{r}_\perp) \\ sin(\mathbf{k}_{M_2}\cdot\mathbf{r}_\perp) \\ sin(\mathbf{k}_{M_3}\cdot\mathbf{r}_\perp) \end{bmatrix} \tag{2.50}$$

which has the solution

$$E = \begin{bmatrix} 1 & 0 & 0 \\ 0 & 1 & 0 \\ 0 & 0 & 1 \end{bmatrix} \tag{2.51}$$

and a trace equal to 3. Similarly to find the character for C_2 operation we need to solve the equation

$$C_2A\mathbf{B}_{B_2}^{M_1} = C_2\hat{z}\begin{bmatrix} sin(\mathbf{k}_{M_1}\cdot\mathbf{r}_\perp) \\ sin(\mathbf{k}_{M_2}\cdot\mathbf{r}_\perp) \\ sin(\mathbf{k}_{M_3}\cdot\mathbf{r}_\perp) \end{bmatrix} = \hat{z}\begin{bmatrix} sin(-\mathbf{k}_{M_1}\cdot\mathbf{r}_\perp) \\ sin(-\mathbf{k}_{M_2}\cdot\mathbf{r}_\perp) \\ sin(-\mathbf{k}_{M_3}\cdot\mathbf{r}_\perp) \end{bmatrix} = \hat{z}\begin{bmatrix} -sin(\mathbf{k}_{M_1}\cdot\mathbf{r}_\perp) \\ -sin(\mathbf{k}_{M_2}\cdot\mathbf{r}_\perp) \\ -sin(\mathbf{k}_{M_3}\cdot\mathbf{r}_\perp) \end{bmatrix} \tag{2.52}$$

which yields

$$C_2 = \begin{bmatrix} -1 & 0 & 0 \\ 0 & -1 & 0 \\ 0 & 0 & -1 \end{bmatrix} \tag{2.53}$$

and a trace of -3. Since we are only looking for the trace we see that we only need to know which k_M vectors stay in the same place. For the C_3 operation the $\mathbf{k}_{M_1}$ vector switches place with the $\mathbf{k}_{M_3}$ vector, the $\mathbf{k}_{M_2}$ vector with the $-\mathbf{k}_{M_1}$ vector, and the $\mathbf{k}_{M_3}$ vector with the $-\mathbf{k}_{M_2}$ vector. Thus, no vector remains in the same place and the trace and character equals 0. Similarly for C_6. Mirror along σ_d and one vector flips, while the other two switches places, giving a trace of -1. For the mirror plane σ_c one vector remains in place, while the two others switch places, resulting in a trace of 1. This representation is labelled S_{d1} and is shown along with the IRREPs in the character table for C_{6v} in table 2.2.

We see that S_{d1} is a combination of $B_1^{''}$ and E_1. The new basis functions for $B_1^{''}$ and E_1 can be found by projecting $A\mathbf{B}_{B_1}^{M}$ onto the IRREP spaces of C_{6v} as previously. This will yield three new basis functions. One for the $B_1^{''}$ space, $\mathbf{B}_{B_1^{''}}^{d1}$, and two degenerate functions for the two dimensional E_1 space, $\mathbf{B}_{E_1}^{d1}$. The degenerate $\mathbf{B}_{E_1}^{d1}$ functions transforms as an (x,y)-dipole pair which provides a good description of the the resonance mode [49]. By going from the C_{6v} symmetry to a lower symmetry, the degeneracy can be removed and the resonance mode can split in to one x-dipole and one y-dipole resonance modes.

Table 2.2: Point group character table for C_{6v}.

C_{6v}	E	C_2	$2C_3$	$2C_6$	$3\sigma_v$	$3\sigma_d$
$A_1^{''}$	1	1	1	1	1	1
$A_2^{''}$	1	1	1	1	-1	-1
$B_1^{''}$	1	-1	1	-1	1	-1
$B_2^{''}$	1	-1	1	-1	-1	1
E_1	2	2	-1	1	0	0
E_2	2	-2	-1	-1	0	0
S_{d1}	3	-3	0	0	1	-1

Chapter 3

Design and simulations

3.1 Sensor design and purpose

The sensor structure is based on an article by Lee and Fauchet [13]. The sensor is made up by air holes 270nm in diameter in a hexagonal pattern in silicon with a lattice constant of 465nm. There are 21 holes in the Γ-M direction and 11 holes in the Γ-K direction. In the center of the photonic crystal there is a hole with a diameter of 140nm, creating a defect state. The defect is placed at the center of the crystal to enable maximal transmission. Light is led in to and out from the photonic crystal through 700nm wide waveguides. The waveguide is 700nm wide to match the mode of the microcavity [13]. A sketch of the structure made in COMSOL is shown in figure 3.1. The sensor and waveguides will be constructed on a silicon on insulator (SOI) wafer. The thickness of the top silicon layer is 200nm. From the article by Lee and Fauchet [13] it is expected that a resonance will appear at a wavelength of 1.58nm.

To test the sensor, light needs to be coupled in to the waveguides. This can be done in a variety of ways, with two common methods being through butt coupling and grating coupling. A butt coupler works by aligning the end of a single mode optical fiber with the cleaved end of the waveguide on the SOI structure. The core diameter of such a fiber is typically $8-10\mu$m while the waveguide is only 700nm wide and 200nm high. This mismatch will cause high losses, typically around 20dB for TE polarized light at 1.55μm [51]. These losses can be reduced by using a taper. The light is then coupled into a waveguide with a width comparable to the fiber, which is then tapered down to 700nm wide. The loss can then be reduced to 0.5dB with a 0.7mm long rounded taper [52].

A grating coupler works through the coupling of light from a fiber placed near vertically above the wafer to a waveguide through a grating on the sample surface. The grating diffracts the light from the fiber in to the waveguide through a taper. The grating area is typically $10\mu\text{m} \times 10\mu\text{m}$. A grating coupler will be optimized for one wavelength depending

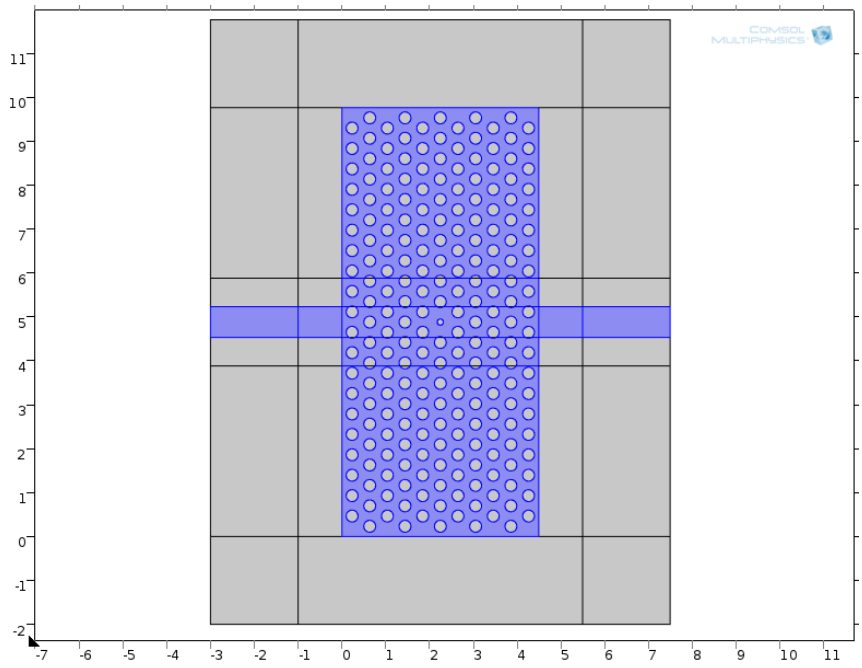

Figure 3.1: A sketch of the sensor structure with input and output waveguides made in COMSOL. The silicon is marked in blue and air in grey. The units of both axes are in µm.

on the period of the grating. Taillaert et al. [53] found that a simple grating with a period of 630nm resulted in a coupling efficiency of 31% with a 40nm 1dB bandwidth. Simulations have shown that with optimal oxide thickness, an efficiency of 61% can be reached [53]. This efficiency can be improved to 69% by the use of a gold layer as a bottom mirror, but this makes the structure much more complex [54]. A silicon oxide overlay that has been etched through along with the silicon can also improve efficiency. Also here a 69% efficiency was reported by Vermeulen et al. [55].

To limit complexity, the simple butt coupling was the chosen coupling mechanism for this project. This will produce a large loss, but high efficiency is not needed to test the sensor. To avoid that the uncoupled light from the fiber gets picked up by the sensor at the output waveguide, a 90 degree bend is introduced in the waveguide. An illustration of the full structure is shown in figure 3.2.

The waveguides along with the plateau that the photonic crystal will be situated on will be constructed by patterning a resist using electron beam lithography (EBL) and afterwards etched using inductively coupled plasma reactive ion etching (ICP-RIE). The process will be based on work done previously at NTNU by Vigen [33]. The photonic crystal structure will be made and optimized using focused ion beam (FIB) milling. The waveguides will not be made with FIB milling due to reported high losses from FIB milled waveguides [56].

The goal of the structure is to function as a sensor. Due to the central defect, there will

Figure 3.2: A sketch of the full structure with input and output waveguides, a 90 bend, and a plateau with the photonic crystal structure.

be a sharp transmission peak at the resonance frequency. The surface can be modified to allow the binding of specific probe molecules, which will have a strong affinity for a target molecule [13]. Some molecules, for example various proteins and DNA, will only bind to one target molecule [57], resulting in a very specific sensor. The change in hole thickness and refractive index will give a shift in resonance frequency that can be measured. The shift is proportional to both the coating thickness and coating refractive index, which both will change when a higher amount of biomolecules bind to the surface. Knowing the relation between the density of the biomolecule film, the film thickness, and the film refractive index, the amount of biomolecules bound to the sensor can be found from the resonance peak shift. A schematic figure of the binding process can be seen in figure 3.3. The results of a layer of biomolecules on the resonance of the described sensor was investigated in the project thesis [34]. The surface can be functionalized by using a procedure similarly to the one described in Pal et al. [58].

There are several possible problems with this approach. If the entire structure is functionalized, then molecules will bind everywhere. The resonance shift will depend on where the molecules bind. Molecules bonded to the top of the structure or at the bottom of holes will create a smaller shift than molecules bonded to the sidewalls [13]. This can make it difficult to precisely determine the exact amount of analyte bonded to sample. To do the calculations the density of bonded molecules at each type of surface needs to be known. An assumption that the density is equal everywhere might be wrong. It is common in sensors like these for the solution containing the analyte to flow over the sensor [59]. The flow might

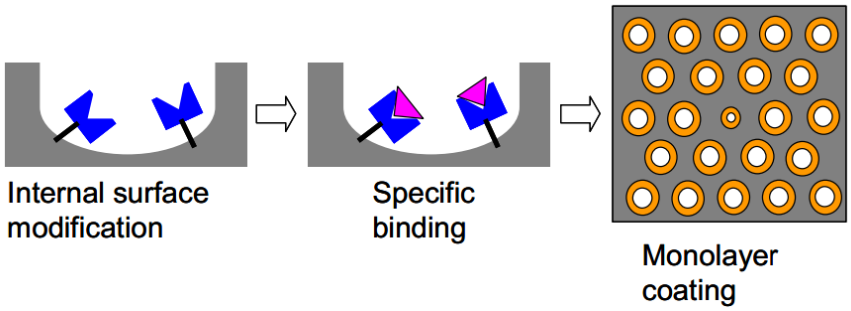

Figure 3.3: A schematic drawing of the biomolecule binding process. The target molecules are captured by the probe molecules which results in a layer of biomolecules on the sensor surface. Figure taken from Lee and Fauchet [13].

be lower in the holes than on the surface, creating differing probabilities of binding and thus differences in density.

Care also has to be taken with regard to the assumed refractive index of the biomolecule refractive index. Most proteins are substantially smaller than the resonance wavelength of this structure [57], which means that the light does not see each individual molecule, but an average of the refractive index of the molecules and the surroundings. The refractive index is thus dependent on the density of the biomolecule layer. The effective index method might be suitable in determining the refractive index [60].

3.2 Band structures

Band structures for photonic slab structures have been found using MIT Photonic Bands (MPB)[40]. A tutorial on MPB and example code can be found in appendix D. The structure is modelled as a layer of silicon ($n = 3.47$) on silicon oxide ($n = 1.44$), with air holes ($n = 1$). The values of n are the refractive indices of the materials at wavelength $\lambda = 1.6\mu$m, which is expected to lay somewhere in the band gap, making the band gap structure as accurate as possible. The SOI wafers available in this work have a 200nm layer of silicon. This gives a thickness relative to the lattice constant ($a = 465$nm) of 0.4301. The holes have a radius of 135nm giving $r/a = 0.2903$.

3.2.1 Shallow holes

The band structures presented in this section are for structures with air holes only in the silicon layer. This structure may be preferred if using an etching process that is highly selective towards silicon compared to silicon oxide. In figure 3.4 the band structure for a 200nm thick silicon layer on oxide can be seen. There is a band gap for TE-like modes

between normalized frequencies of 0.280 and 0.348, or, with a lattice constant of 465nm, $1.81e14$Hz and $2.24e14$Hz. In terms of wavelength this gives a band gap between 1.34µm and 1.66µm, which includes the found resonance wavelength of 1.58µm from Lee and Fauchet [13]. The band structure for the structure with infinite thickness silicon was found during the project[34] and is reprinted in figure 3.5. It is observable that the slab band gap has moved towards higher frequencies. The band gap in figure 3.5 stretches from $\nu_n = 0.207$ to $\nu_n = 0.268$, a band gap size approximately equal to the slab band gap size.

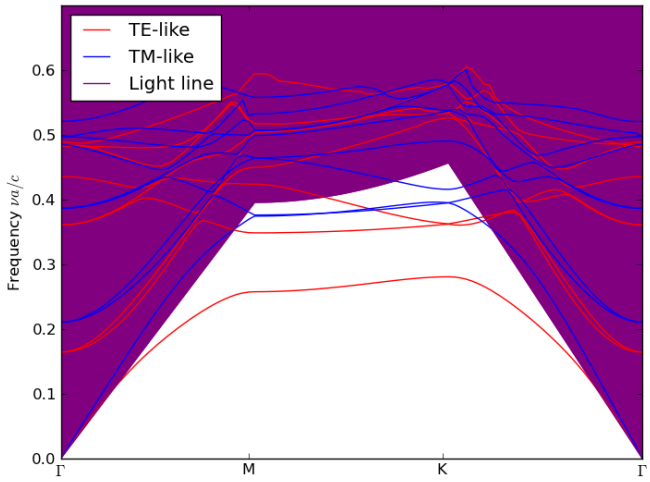

Figure 3.4: The band structure of a silicon photonic crystal slab on oxide with air holes in an hexagonal pattern.

SOI is available with varying top layer thicknesses. Changing the thickness results in a change in the band gap size according to the theory. In figure 3.8 a plot of the TE gap-midgap ratio versus relative substrate thickness can be observed. This plot follows the trend stated in section 2.5, with the biggest band gap size appearing at a specific thickness and not at infinite thickness. The biggest band gap appears around a relative thickness of 1.0, i.e. at a thickness equal to the lattice constant for this structure. Still, it is not the goal of the structure investigated in this work to achieve the largest band gap, but to make a structure with a band gap large enough with the available substrate and fabrication techniques. From the plot it is apparent that there is an area from a relative thickness of 0.4 to 1.1 where the gap-midgap ratio is relatively constant, well above 20%. This corresponds to a real thickness of 186nm to 511nm for the studied structure, which includes the thickness of the top layer of the SOI wafer available.

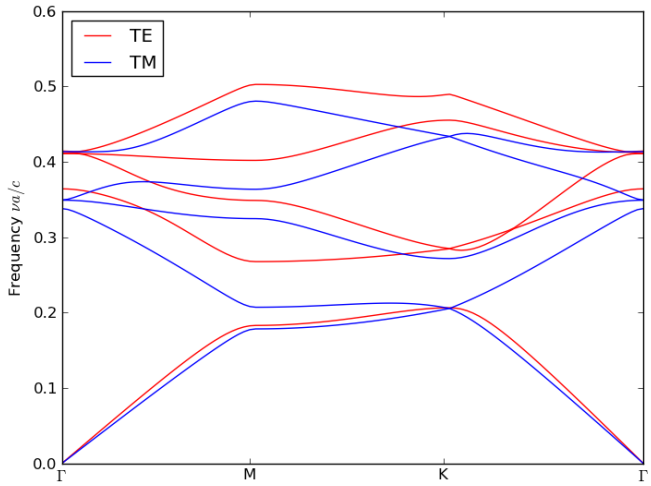

Figure 3.5: The band structure of a hexagonal photonic crystal which is infinite in the z-direction.

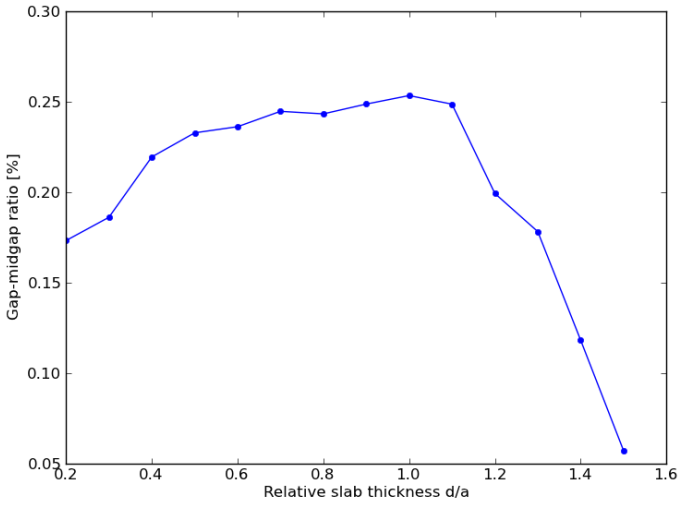

Figure 3.6: TE gap-midgap ratio versus relative substrate thickness for a structure of silicon on silicon oxide with $r/s = 0.2903$.

3.2.2 Deep holes

Etching holes in the oxide substrate as well as in the silicon may be easier to fabricate, for example when using etches with low selectivity and etch rate control. The results of a simulation of the band structure for the hexagonal photonic crystal slab with holes running through the oxide can therefore be seen in figure 3.7. There is barely a difference between this structure and the structure with shallow hole. This band gap stretches from $\nu_n = 0.280$ to $\nu_n = 0.353$, which is larger as predicted in section 2.5, but only a marginally larger band gap. This points to that changing the hole depth has a negligible effect on the resulting band gap for this photonic structure and thus probably also a negligible effect on the position of the resonance.

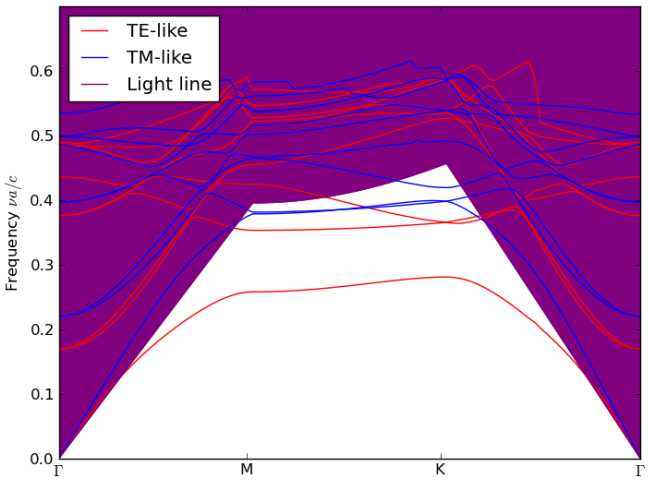

Figure 3.7: The band structure of a silicon photonic crystal slab on oxide air holes running through the entire structure.

The effect of varying slab thickness has been found for this structure as well (figure 3.8). The differences between this plot and the one presented for the slab with holes only in the silicon layer are small, but noticeable. The effect is most profound for thinner structures, where holes running through the entire structure gives a gap-midgap ratio up to 5% larger. The peak gap-midgap ratio appears for both structures at a relative thickness of 1.0, however the structure with deep holes has a smaller variation in size around the peak, making this kind of structure less sensitive to a change of SOI substrate.

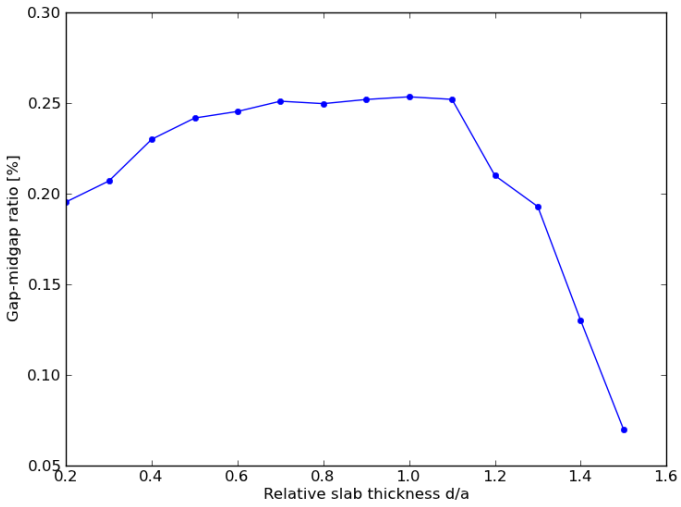

Figure 3.8: TE gap-midgap ratio versus relative substrate thickness for a structure of silicon on silicon oxide with $r/s = 0.2903$ and holes running through both the silicon and oxide layer.

3.2.3 Symmetrical structure

For comparison, the band structure for the photonic crystal slab suspended in air is shown in figure 3.9. The band gap stretches from $\nu_v = 0.282$ to $\nu_v = 0.336$, i.e. a smaller band gap than seen for the asymmetrical photonic crystal slabs. However, the differences between the studied structures are small, and going from one to another would not give a noticeable effect as the size of the band gap is not of importance in the studied structure. It is to be noted that a change in structure would likely also affect the position of the resonance, which would be noticeable.

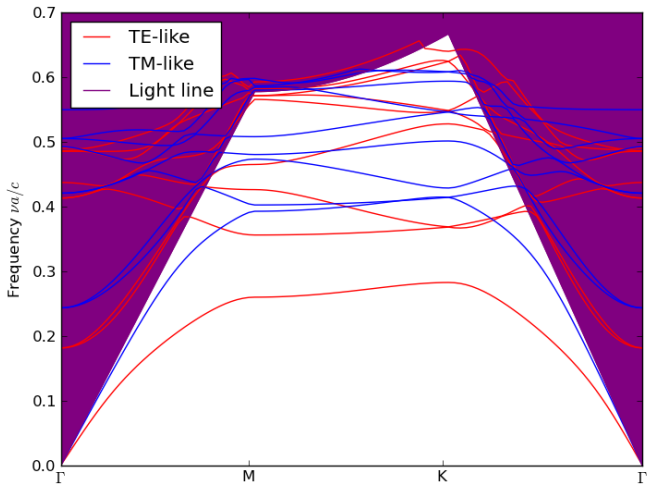

Figure 3.9: The band structure of the silicon photonic crystal slab supended in air.

3.3 Simulations of non-ideal sensor stuctures

In the project thesis[34] transmission through a perfect photonic crystal was investigated. However, during a fabrication process errors can be introduced. Work previously done on photonic crystals have shown that both hole position and hole shape can deviate from the desired position and shape [31, 32]. The effects of this have been investigated in literature [61, 62, 63]. Here the effects of these fabrication errors have been investigated in relation to the structure studied in this thesis. The deviating shape is modelled as a normally distributed deviation from an ideal radius r_0 and is adapted from the work on the project thesis by Lorvik [64]. Each hole will be quantified by the equation

$$r(\phi) = r_0 \cdot (1 + \mathcal{N}(0, \sigma_r^2)) \tag{3.1}$$

where r_0 is the ideal radius, and $\mathcal{N}(0, \sigma_r^2)$ is the normal distribution with mean 0 and standard deviation σ_r. For each specified angle around the circle ϕ, a new radius is drawn, creating a normally distributed $r(\phi)$ around r_0. The number of points a new radius is drawn will also contribute to the shape of the holes. COMSOL will interpolate between the holes to produce the final shape. Lorvik [64] found that 8 points created suitable and realistic hole shapes.

The effect of hole position deviation is modelled similarly. During the fabrication process the position of the holes deviates from the ideal position by a distance given by a normal distribution [62]. The equation used takes on a similar shape to equation 3.1

$$\begin{aligned} p(x) &= p_0(x) + \mathcal{N}(0, \sigma_p^2) \\ p(y) &= p_0(y) + \mathcal{N}(0, \sigma_p^2) \end{aligned} \tag{3.2}$$

where $p_0(x)$ and $p_0(y)$ are the x- and y-coordinates of the ideal position, respectively, and $\mathcal{N}(0, \sigma_p^2)$ is the normal distribution with mean 0 and standard deviation σ_p^2. The script used and an introduction to COMSOL can be found in appendix E. In all simulations the refractive index of air has been set to 1 and the refractive index of silicon to 3.455, which is the correct value for a wavelength of 1.85µm [65].

In both cases a split of the resonance in to an x-dipole and a y-dipole is expected as the symmetry of the structure is removed.

The simulations are done in two dimensions, not three, thus the resonance will not be in the same position as if the structure was modelled as a slab [34]. This can also be seen from the fact that the resonances will not appear inside the bandgaps found in section 3.2. However, the general behaviour of the resonances will be correct also for three dimensional structures as was found in the project thesis [34].

3.3.1 Effect of hole shape on resonance

The effect of deviating hole shape was studied using three different values of σ_r: 0.01, 0.03, and 0.05. The shape of one of the holes along with the full structure for $\sigma_r = 0.01$ can be seen in figure 3.10. The deviation from the ideal hole shape can barely be detected. $\sigma_r = 0.01$ equals a standard deviation of 2.7nm for a hole with radius of 270nm as in these simulations. A plot of the transmission can be seen in figure 3.11. For comparison a plot of the transmission with perfect holes can be seen in figure 3.12.

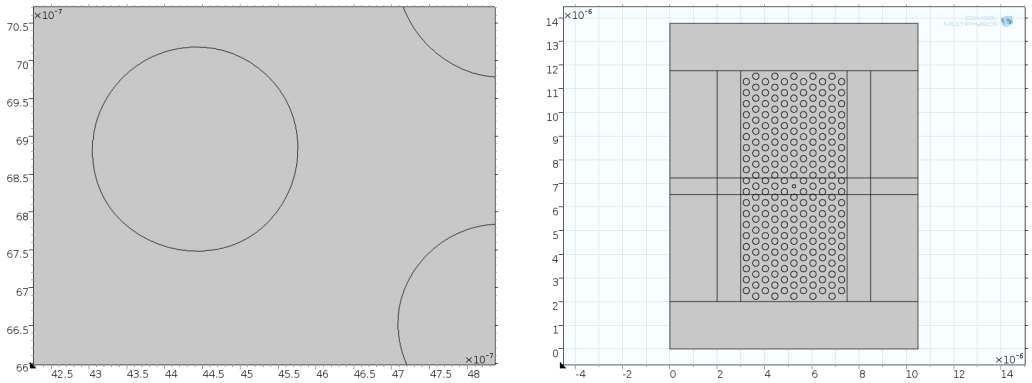

(a) A single hole. (b) The entire structure.

Figure 3.10: A sensor with $\sigma_r = 0.01$. Both axes have unit m.

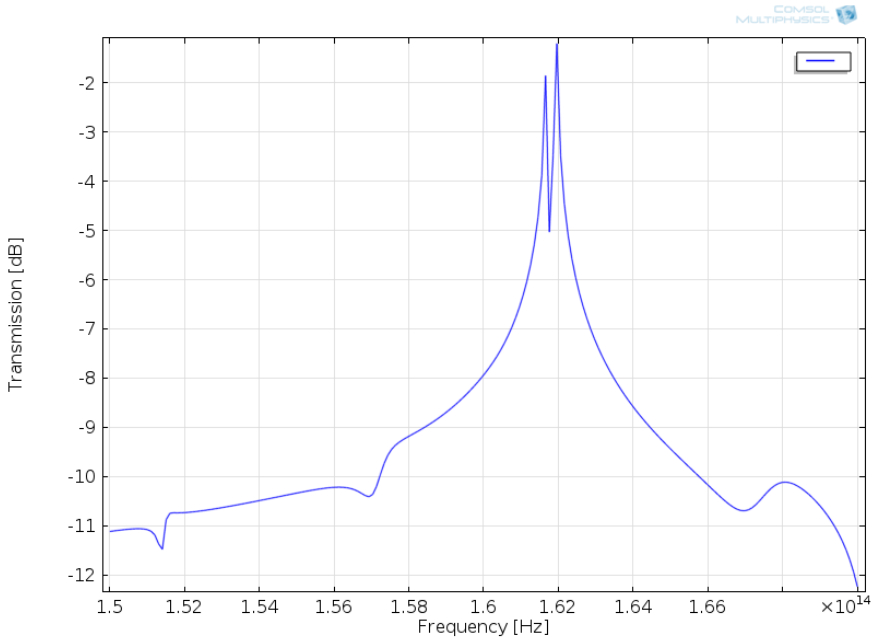

Figure 3.11: Transmission through the photonic crystal with $\sigma_r = 0.01$. The transmission was calculated at 200 equally spaced points between 1.5e14Hz and 1.7e14Hz.

The split of the resonance peak as predicted by the group theory can clearly be seen, even for such a small degree of hole unevenness. The electric field norms (defined as $\sqrt{|E_x|^2 + |E_y|^2 + |E_z|^2}$) of the two new resonances can be seen in figure 3.13. The fields match the expected modes from the theory in section 2.6.2 with two dipoles orthogonal to each other. Using the coordinate system from section 2.6.2 we label the highest frequency resonance as the x-dipole and the lowest as the y-dipole. The deviating hole shape has otherwise had a small effect on the spectrum.

The frequency resolution of the simulation is not high enough to observe if the strength of the resonances are equal. A new calculation with 200 equally spaced frequencies between 1.616e14Hz and 1.62e14Hz was therefore made. The results are shown in figure 3.14. It is apparent that the two resonances do not behave exactly the same with regards to shape, width, and height, but that the differences are small. The difference in strength of the resonances is negligible. The difference in wavelength for the two peaks is 2.3nm, meaning that the split will be observable even with such a small hole shape deviation.

The simulations were repeated for several randomly generated structures with $\sigma_r = 0.01$ with the results shown in figure 3.15. The spectra are clearly different, with the splitting barely being observed for some structures. This is both due to the frequency resolution and due to the hole shape being randomly generated. There are enough holes that the general unevenness of the holes will be the same for every generated structure, nonetheless, the field

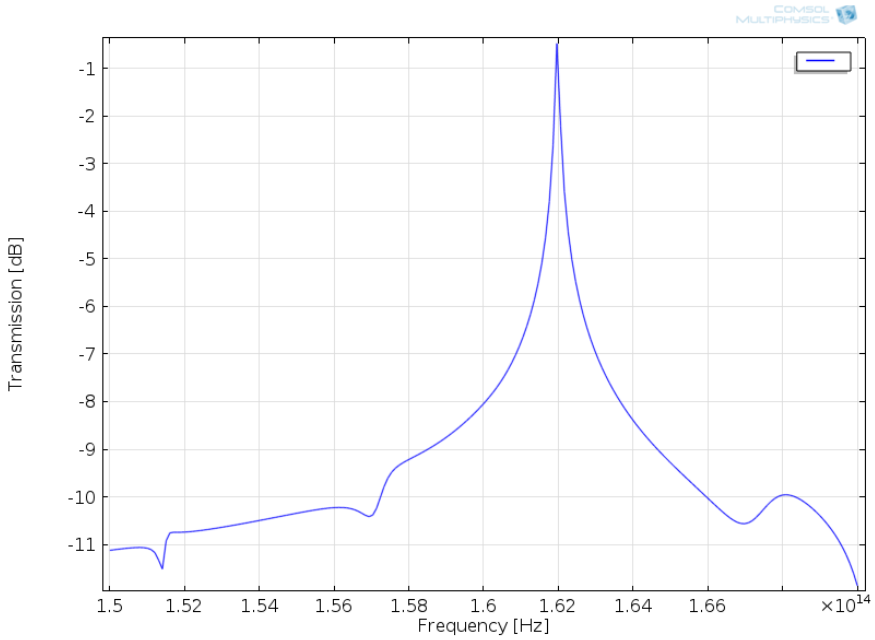

Figure 3.12: Transmission through the perfect photonic crystal. The transmission was calculated at 200 equally spaced points between 1.5e14Hz and 1.7e14Hz.

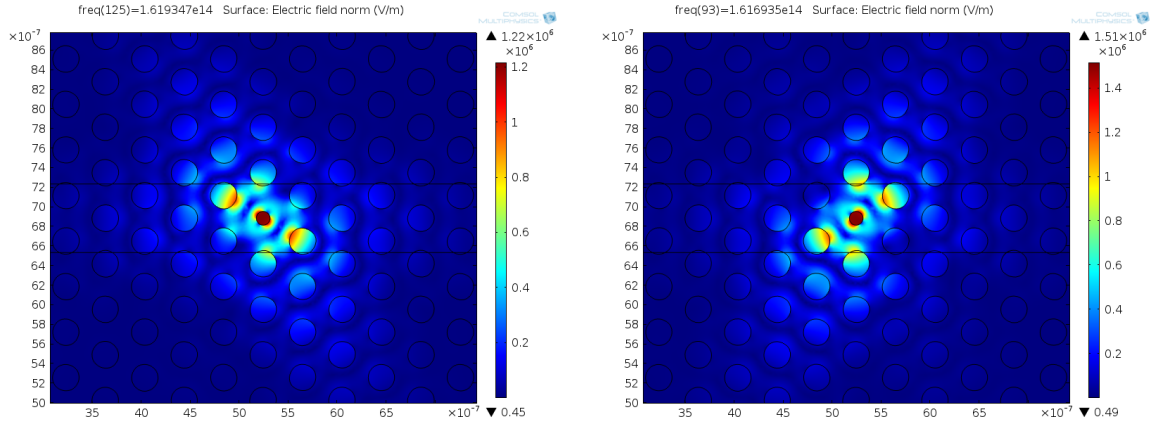

(a) x-dipole.

(b) y-dipole.

Figure 3.13: The electric field norms of the resonances in figure 3.11.

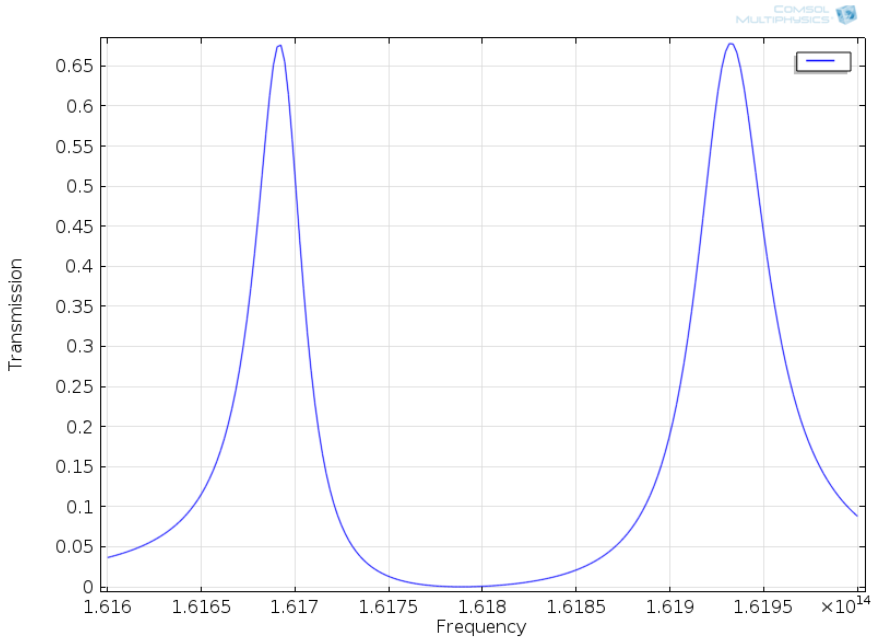

Figure 3.14: A close up of the resonance peaks from figure 3.11.

is concentrated around the defect, making the holes in the vicinity most important for the resonance behaviour. If by chance the holes near the defect have a smaller deviation from the ideal hole shape, then the split will be smaller.

Simulations were done with $\sigma_r = 0.03$ and $\sigma_r = 0.05$ with the calculated spectra shown in figure 3.16 and the typical hole shapes for each structure shown in figure 3.17. The split increases as the hole shape deviated more from the perfect circle. This supports the claim made earlier that the differences in spectra in figure 3.15 are due to differences in hole deviation near the defect.

The electric field norms of the split resonances are shown in figure 3.18. From the figures it is observed that the x-dipole is always the higher frequency resonance and that the direction of the dipoles with regards to the photonic crystal is not always the same. This is probably again due to the randomness of the hole shapes. The mode in the cavity will position its electric field to achieve an energy as low as possible. This position will mostly be dependent on the holes around the defect and thus be different for each generation of the structure.

It can also be observed that the resonances do not line up perfectly with the symmetry axes of the photonic crystal. Again this is due to the symmetry being broken. When the photonic crystal is perfect, the resonance modes needs to have the same symmetry as the cavity, however now there is no symmetry left and the energy minima may not line up with the previous symmetry axes.

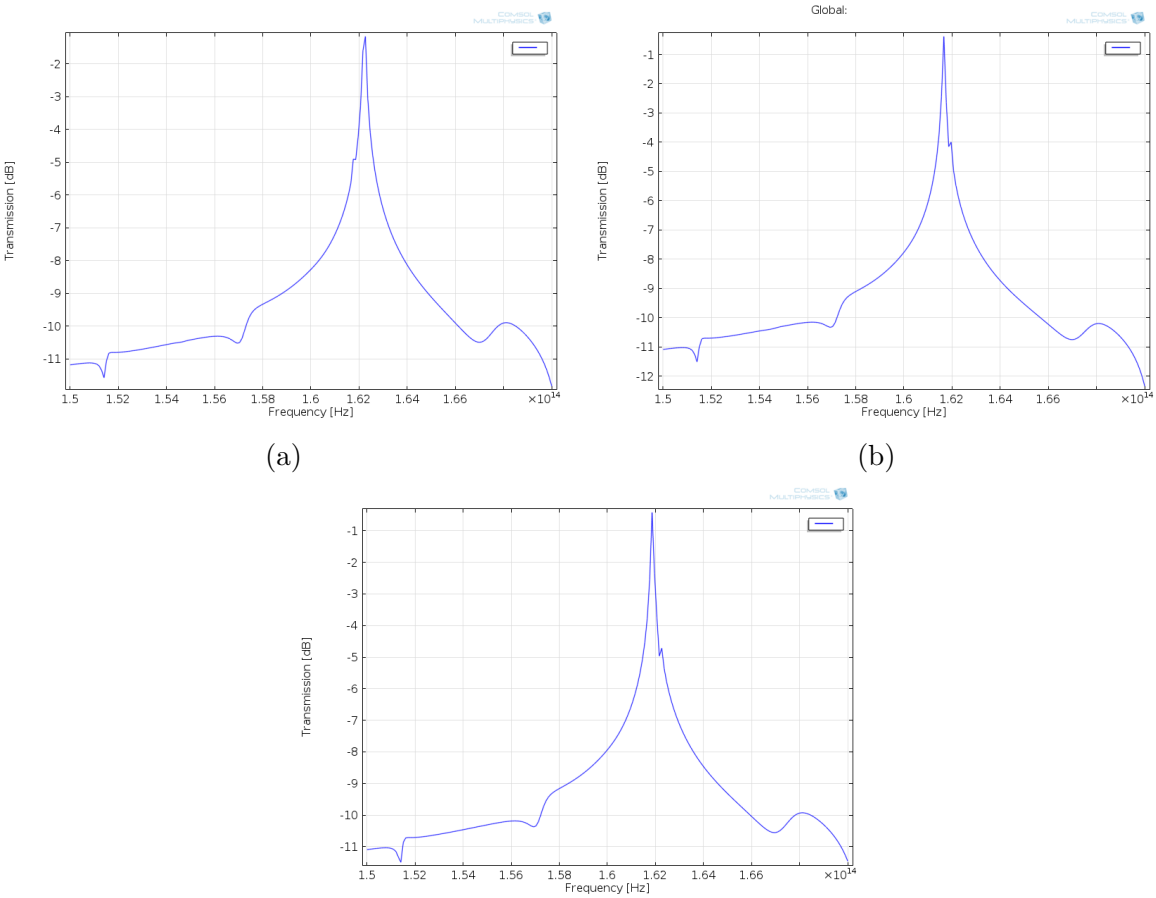

Figure 3.15: Frequency spectra for three generated structures with $\sigma_r = 0.01$. The transmission was calculated at 200 equally spaced points between $1.5e14$Hz and $1.7e14$Hz.

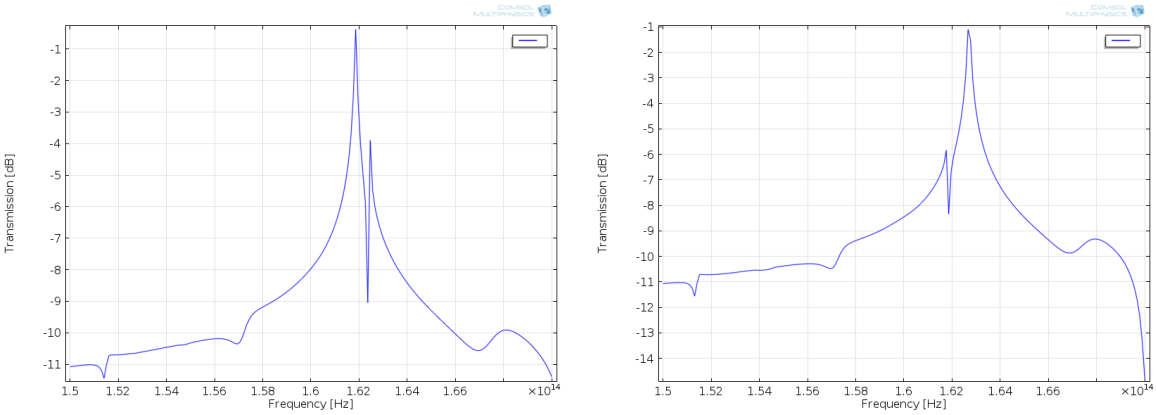

(a) $sigma_r = 0.03$. (b) $sigma_r = 0.05$.

Figure 3.16: Frequency spectra structures with $\sigma_r = 0.03$ and $\sigma_r = 0.05$. The transmission was calculated at 200 equally spaced points between $1.5e14$Hz and $1.7e14$Hz.

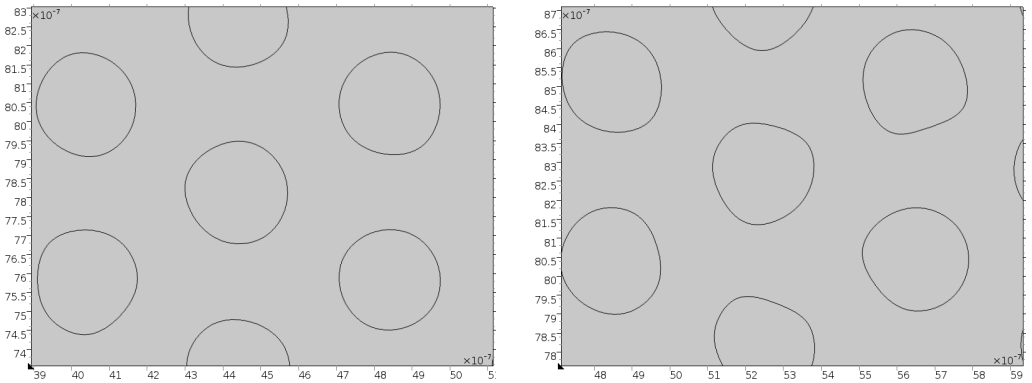

(a) $sigma_r = 0.03$. (b) $sigma_r = 0.05$.

Figure 3.17: Typical hole shapes for the structures with $\sigma_r = 0.03$ and $\sigma_r = 0.05$.

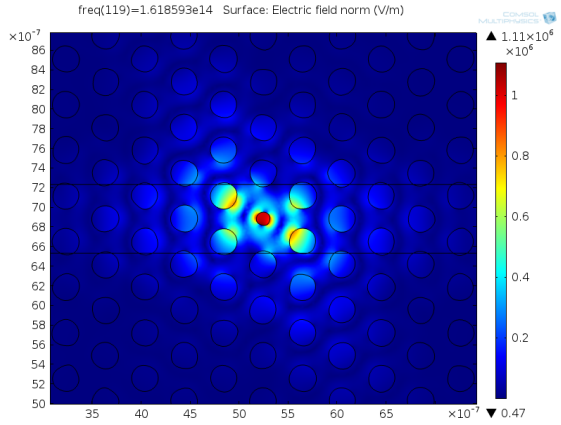

(a) x-dipole for $sigma_r = 0.03$.

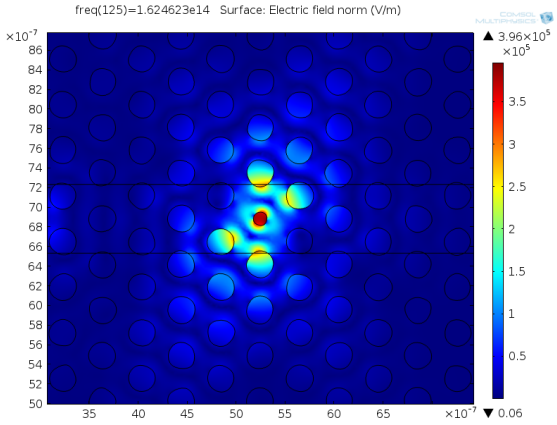

(b) y-dipole for $sigma_r = 0.05$.

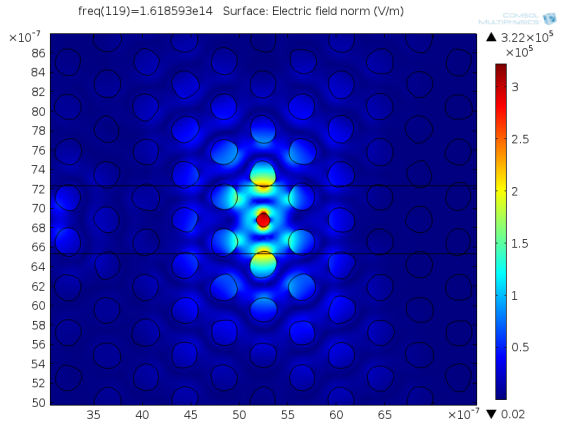

(c) x-dipole for $sigma_r = 0.03$.

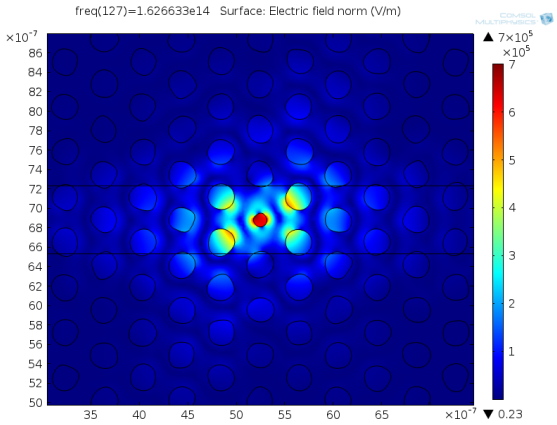

(d) y-dipole for $sigma_r = 0.05$.

Figure 3.18: The electric field norms for the resonances in structures with $\sigma_r = 0.03$ and $\sigma_r = 0.05$.

3.3.2 Effect of hole position on resonance

Fan et al. [62] found that in their fabrication process the average hole position deviated from the correct position with a standard deviation in the x-direction of 2.63nm and in the y-direction of 2.05nm. The effect of deviating hole positions was thus studied with $\sigma_p = 2.5e\text{–}9$. In addition, the effect of structures with $\sigma_p = 6e\text{–}9$ and $\sigma_p = 10e\text{–}9$ were investigated. The frequency spectrum of the photonic crystal with $\sigma_p = 2.5e\text{–}9$ is shown in figure 3.19 and the geometry is shown in figure 3.20.

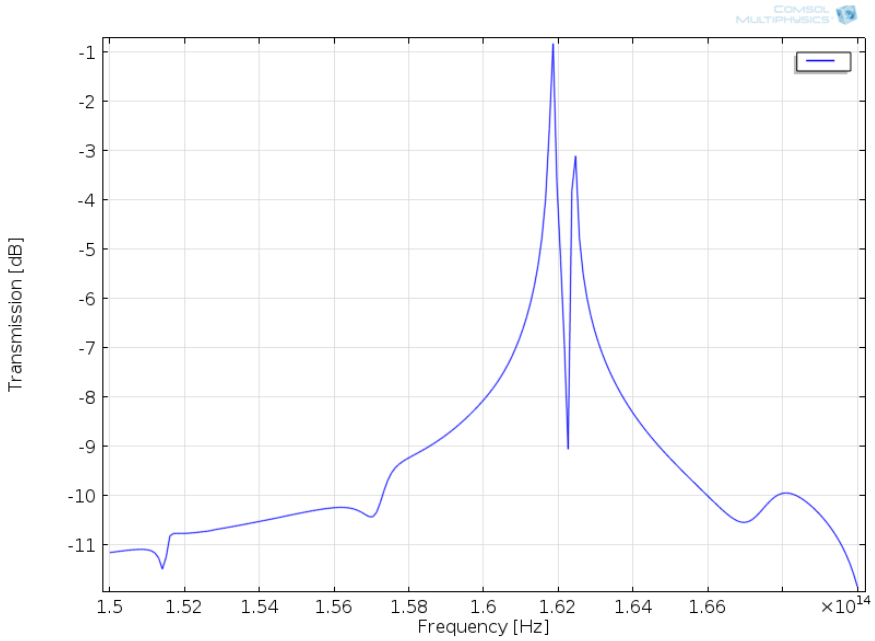

Figure 3.19: Transmission through the photonic crystal with $\sigma_p = 2.5e\text{–}9$. The transmission was calculated at 200 equally spaced points between $1.5e14$Hz and $1.7e14$Hz.

Again the resonance is split in to an x- and a y-dipole as predicted by theory. The electric field norms of the two peaks are presented in figure 3.21. As in the previous section a higher resolution simulation was done comparing the strength of the two peaks (fig. 3.22). Again, the two peaks look quite similar, but are slightly different with regards to both shape and height.

The splitting of the resonance is magnified with increasing hole position deviation as can be seen in the transmission spectra for $\sigma_p = 6e\text{–}9$ and $\sigma_p = 10e\text{–}9$ in figure 3.23. The electric field norms of the resonances are shown in figure 3.25 and follow the same trend as with increasing σ_r. The typical geometry of the structures can be seen in figure 3.24.

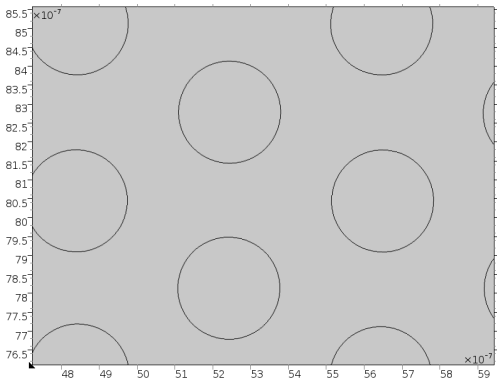

Figure 3.20: The geometry of a photonic crystal with $\sigma_p = 2.5e$–9.

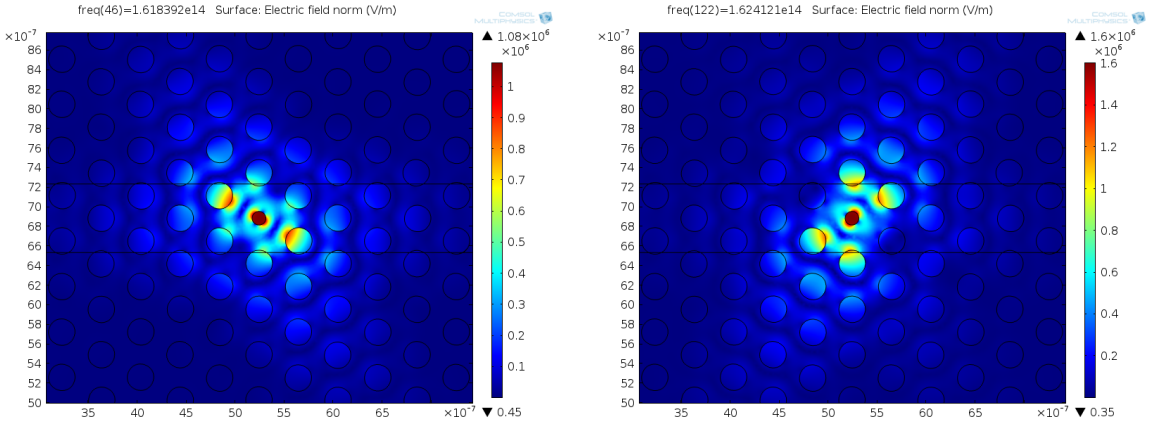

(a) x-dipole. (b) y-dipole.

Figure 3.21: The electric field norms of the resonances in figure 3.19.

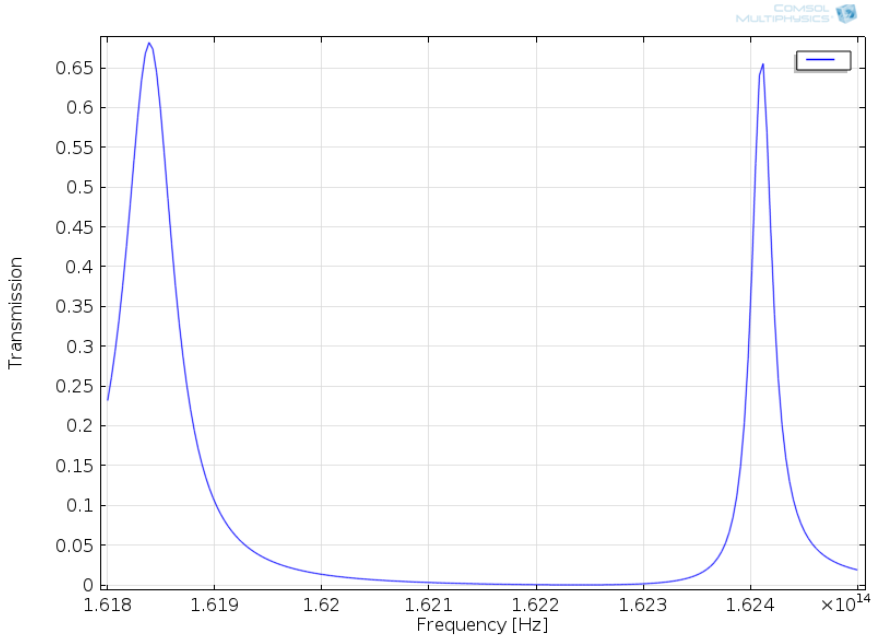

Figure 3.22: Transmission through the photonic crystal with $\sigma_r = 2.5e{-}9$. The transmission was calculated at 200 equally spaced points between $1.618e14$Hz and $1.625e14$Hz.

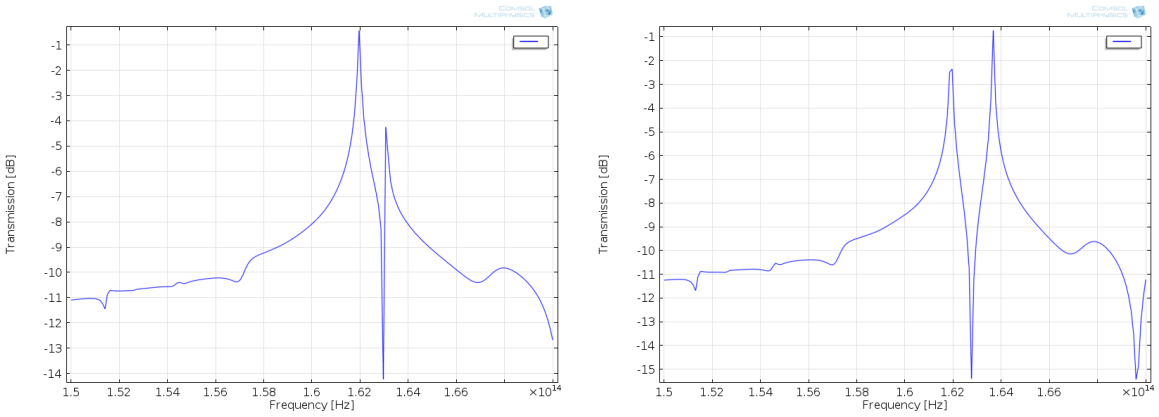

(a) $\sigma_p = 6e{-}9$. (b) $\sigma_p = 10e{-}9$.

Figure 3.23: Transmission through the photonic crystal with $\sigma_p = 6e{-}9$ and $\sigma_p = 10e{-}9$. The transmission was calculated at 200 equally spaced points between $1.5e14$Hz and $1.7e14$Hz.

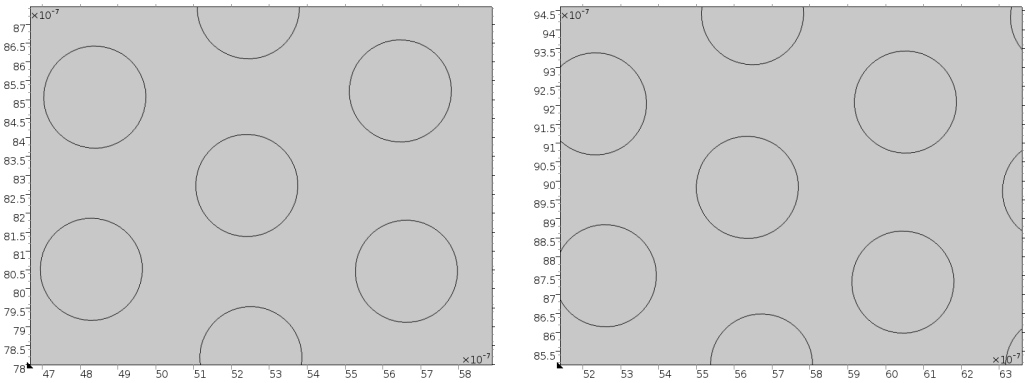

(a) $sigma_r = 6e{-}9$. (b) $sigma_p = 10e{-}9$.

Figure 3.24: Typical geomtry for the structures with $sigma_r = 6e{-}9$ and $sigma_p = 10e{-}9$.

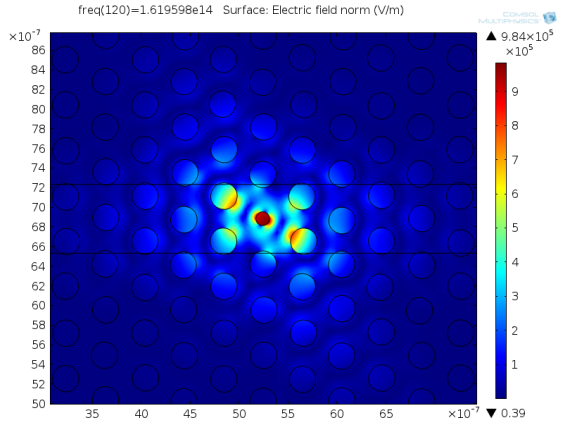

(a) x-dipole for $\sigma_p = 6e$–9.

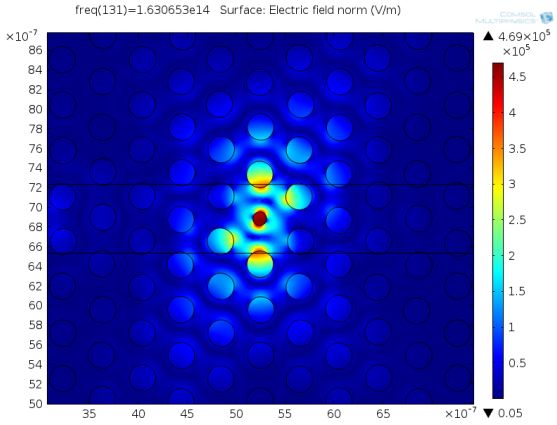

(b) y-dipole for $\sigma_p = 6e$–9.

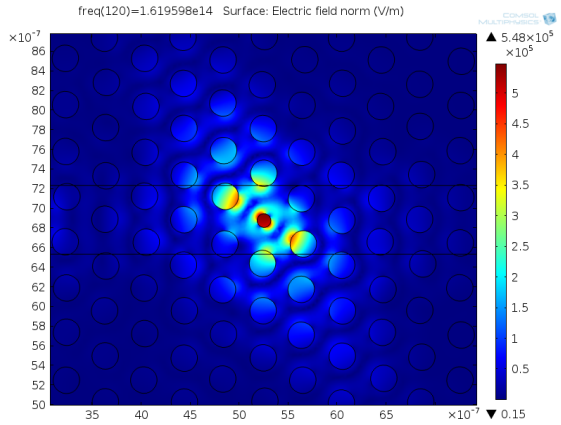

(c) x-dipole for $\sigma_p = 10e$–9.

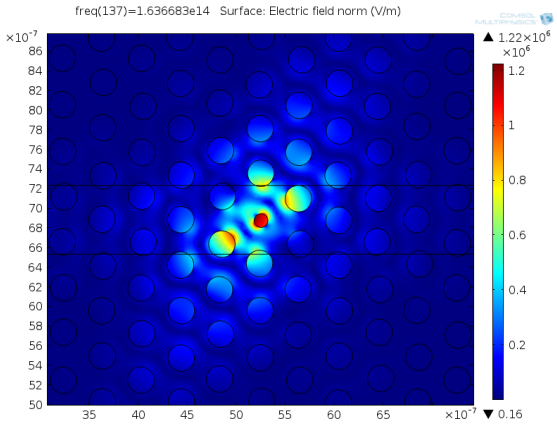

(d) y-dipole for $\sigma_p = 10e$–9.

Figure 3.25: The electric field norms for the resonances in structures with $\sigma_p = 6e$–9 and $\sigma_p = 10e$–9.

Chapter 4

Equipment and fabrication

4.1 Scanning electron microscope

The scanning electron microscope (SEM) uses electrons to image primarily the surface of a sample. Some information can also be gained from the interior of the material. A beam of electrons is focused to a probe size of down to an atom [66]. In figure 4.1 a typical SEM can be seen.

The electron beam is focused using lenses and apertures as in an optical microscope, but in this case the lenses are electromagnets. Just before the sample, two magnetic deflection coils scan the electron beam over the surface [67].

In figure 4.2 the interaction volume from the electron beam hitting the specimen is shown. As seen the electrons interact with not just the surface, but also from a volume inside the specimen. When looking at the surface, secondary electrons (SE) are used as they have a very short escape depth, 1nm in metals. Secondary electrons have low energy ($E < 50$eV) that are released due to inelastic scattering with the primary electron beam [68].

Backscattered electrons (BSE) come from elastic scattering when the primary electron beam interacts with the atoms in the specimen and returns out of the surface again. They have energies from 50eV up to the energy of the electron beam. They scatter from a larger area inside the interaction volume than SE and therefore give information about volume and not just the surface. Heavier atoms scatter more electrons making it possible to gain information about the composition [69].

An electron can hit an atom an knock an electron from the inner shells loose. When electrons move down to that free energy level from higher levels x-rays can be released. Each element has a unique x-ray fingerprint. The x-rays come from an even larger volume than the BSE [69].

Electrons can also pass through a thin sample and be collected. The electrons are deflected by the atoms as in a transmission electron microscope [66].

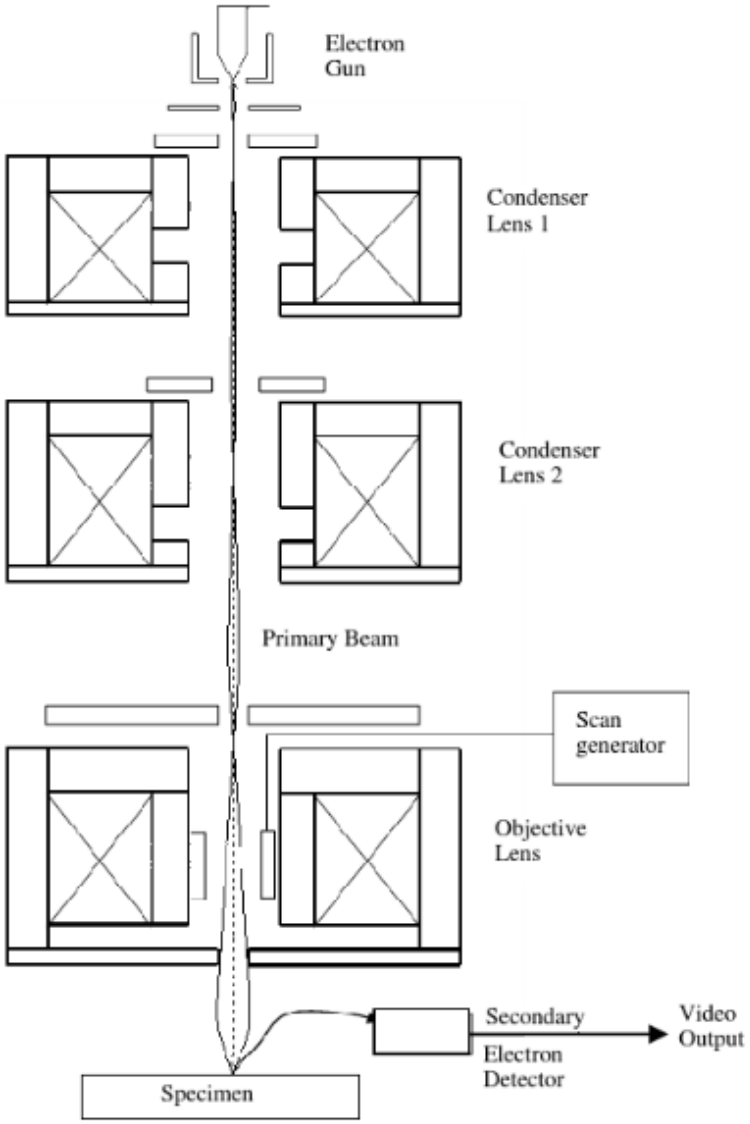

Figure 4.1: A schematic drawing of a SEM. Various other sensors in addition to the secondary electron detector can be added. Figure taken from Khursheed [67].

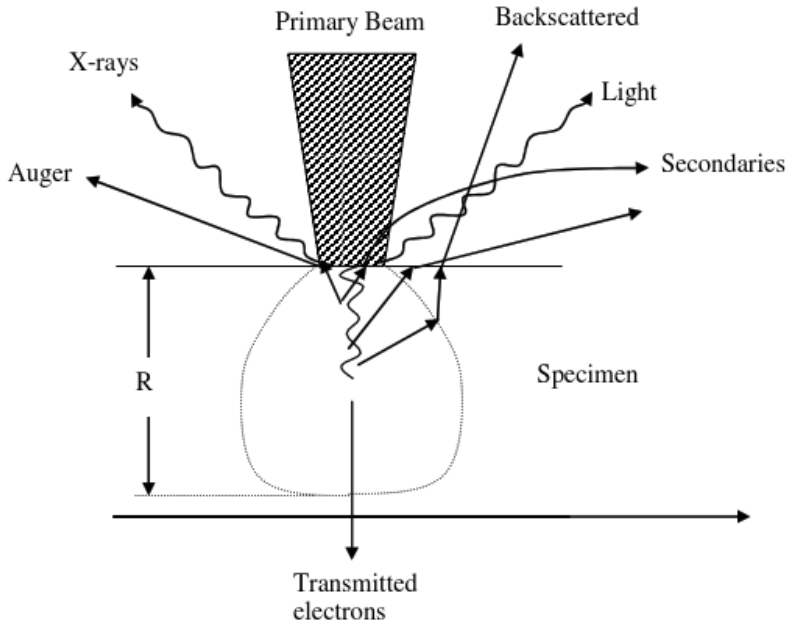

Figure 4.2: The interaction volume and the emitted signals. Figure taken from Khursheed [67].

Figure 4.3 shows a Monte Carlo simulation of the scattering of the primary electron beam in a Si sample.We see from these simulations that the interaction volume increases as the electron beam energy increases, while the width of the interaction at the surface decreases.

The SEM used in this work is an Hitachi S-5500 S(T)EM with possible acceleration voltages between 0.5kV and 30kV and an attainable resolution of 0.4nm [70].

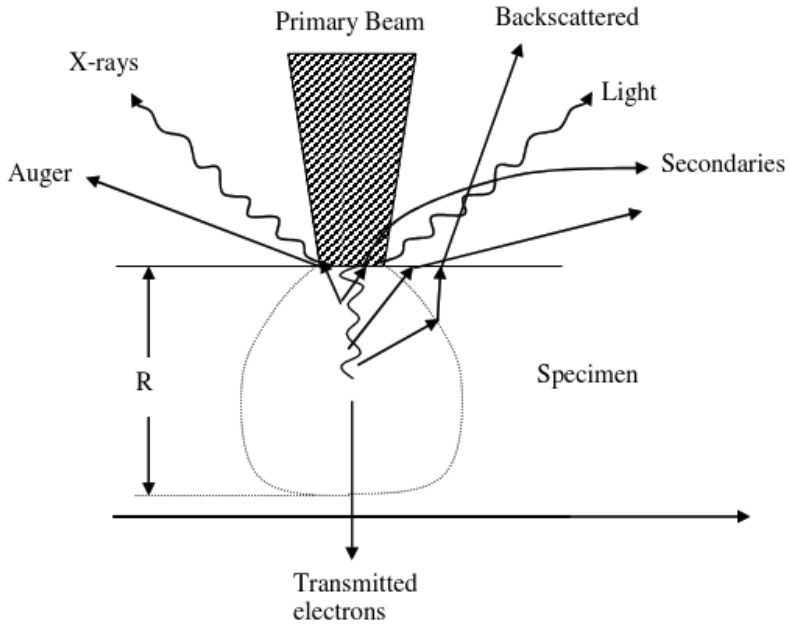

Figure 4.3: Monte Carlo simulation of the scattering of the primary beam in a Si sample. Figure taken from Khursheed [67].

4.2 Electron beam lithography

Traditional lithography is based on covering the substrate with a sacrificial layer, a photoresist, which is then patterned. The patterning is done by exposing the resist to UV light through a mask. The exposed areas are, in the case of a positive resist, made soluble in a developer liquid. The mask pattern is thereby transferred to the resist layer. When using a negative resist the exposed areas will harden and a negative of the mask will be transferred. The size of the pattern is limited by the wavelength of the light used to expose the resist, with features usually not smaller than on the order of the wavelength [14].

With electron beam lithography (EBL) the resist is exposed with electrons instead of light. No mask is used, instead a single beam is moved across the resist. The resist reacts to the exposure and the electron beam writes the pattern in the resist. This makes the EBL process slower and more expensive than the traditional UV lithography and mainly used in research [71].

A common resist is polymethylmethacrylate (PMMA) which was discovered by Hatzakis in 1969 [72] and has been used with EBL to create photonic crystals for various applications [24, 25, 26, 27]. A number of research groups have claimed to achieve sub-10nm lines using PMMA [73]. PMMA can be used both as a positive and a negative resist. Exposing the resist to a moderate dose of irradiation causes the exposed resist to degrade in to fragments

of lower molecular weight and can be disolved in methyl isobutylketone in propanol which does not affect the unexposed resist. For higher exposure (greater than 50-70C/m$^-$2 for a 100nm thick resist) PMMA acts as a negative resist, and exposure to the electron beam makes the PMMA molecules crosslink. The areas not crosslinked are soluble in acetone and submerging the resist in acetone makes the pattern as written using the EBL appear on the substrate [74].

The EBL at NTNU NanoLab (Hitachi 4300 SEM & Raith electronics [70]) is a repurposed SEM. An EBL and a SEM has many similarities, which means that we can use our SEM knowledge when understanding the EBL [75].

Important parameters when using EBL are acceleration voltage, beam current, working distance, write field size and beam speed [76]. A higher acceleration voltage enables a smaller beam size at the surface (probe size), but also leads to more backscattered electrons [75]. Higher beam current exposes the resist faster, but reduces the probe size and increases the depth of field (DoF), the depth the beam is focused in the sample. A low DoF can result in the resist being exposed unevenly at different depths. A lower current also results in a smaller probe size. The working distance is the distance from the last lens and the sample surface. Increasing the working distance gives an increased DoF, but lower resolutions and more aberrations. Increasing both the write field size and beam speed will increase the write speed at the cost of resolution and precision.

The dose is the amount of electrons per area. It is determined by the chosen current and the dwell time, the time the beam lingers at each point, which is given by the beam speed. Different doses are defined for areas, curves, lines, and dots.

Electrons can backscatter after hitting the surface as seen in figure 4.3 at higher energies, and can lead to exposure of the resist surrounding the wanted feature, called the proximity effect. This is most noticeable when exposed features are located closely. The backscattered electrons can overexpose and distort a nearby feature, making feature density an important factor when determining the dose [77].

If the desired pattern is larger than the write field, the write field must either be made larger at the cost of resolution or the stage can be moved. To achieve good results, the new write field after the stage movement has to be properly aligned with the old write field to avoid stitching errors [76]. The EBL at NTNU NanoLab uses laser interferometry to find the stage position and enables stitching of write fields with less than a 20nm shift [70].

4.2.1 Setup

In this work two resist blends (50% PMMA A9 and 50% anisol, and 46% PMMA A9 and 56% anisol) have been used as a positive resist. It is applied to the sample with a spin coater using the spin recipe in table 4.1 which along with the resist blends are adapted from Vigen [33], in which it was found that this combination gave good resist thickness uniformity. Before spin coating the samples were also dehydration baked on a hot plate for

Table 4.1: The spin recipe.

Sequence	Spin speed [RPM]	Acceleration [RPM/s]	Time [s]
1	500	1000	12
2	3500	1000	60

Table 4.2: The default EBL doses.

Parameter	Value	Unit
Area dose	100	$\mu As/cm^2$
Curved area dose	100	$\mu As/cm^2$
Line dose	300	pAs/cm
Dot dose	0.1	pAs

10 minutes at 180°C. This is to remove water molecules from the sample surface and improve resist adhesion. The sample is afterwards placed on the spin coater wafer chuck and resist is applied with a pipette. The spin coating follows the recipe in table 4.1. Following the spin coating, the sample is again baked at 180°C for 60 s and then placed on a cold plate. The underside of the sample is scraped with a scalpel to remove any resist stains. An uneven underside will make write field stitching difficult. To ensure good write field stitching, write field alignment is performed. The exposure is done at 20 kV with a current of 40 pA. Beam alignment was done on a gold covered silicon wafer to hinder unwanted exposure of the spin coated sample. The edge bead effect is the gathering of resist near the sample edges, making the resist thicker than in the center. Therefore, the exposure is done in the center of the sample. The default doses for the EBL used is presented in table 4.2. The exposure step size is 0.02µm for area and curved area exposures and 0.01µm for line exposures. The write field used is 50µm times 50µm in size.

After exposure the sample is developed in a solution of 9 parts isopropanol and 1 part deionized water with some slight agitation for 30 seconds after which the sample is immediately submerged in deionized water to stop the development. This procedure is taken from Vigen [33].

4.3 Focused ion beam

Focused ion beam (FIB) systems were developed during the 70s and early 80s with the invention of liquid metal ion source. The first commercial instruments were introduced in the late 80s [78]. FIB has been used for making various nanostructured devices, making and repairing lithographic masks, and correction of integrated circuits. As with EBL, FIB is a mask free process, but unlike an EBL system, with FIB a beam of Ga^+ ions scans over

the surface to create a pattern. The FIB system does not expose a resist, but sputters the material directly due to elastic and inelastic collisions between the ions and the substrate [79]. FIB has been used to fabricate photonic crystal structures, both in silicon [23, 80] and other materials [21, 22]

A FIB instrument is usually made up of a FIB column and a SEM column inside a vacuum chamber. Inlets for different gases can also be included. Both the ions from the FIB column and the electrons from the SEM column are focused on the sample in the same manner as in a pure SEM system. The two beams hits the sample at an angle relative to each other. In the FIB at NTNU NanoLab the beams are offset by 52 degrees. When properly aligned the beams should hit the same spot on the sample. The ion source is liquid gallium covering a tungsten needle and exposed to a high extraction field which pulls the gallium in to a sharp cone with a radius of 5-10nm. The ion beam can be focused to a very fine probe under 10nm in diameter. Gallium is used because its melting point is close to room temperature (30 °C) and does not form an alloy with the tungsten needle [81].

In the ion column the Ga atoms are accelerated by a voltage between 5kV and 30kV. A higher voltage gives the ions higher energy when reaching the surface and will penetrate deeper [82]. As with accelerated atoms, an increased energy makes the probe size smaller as well as narrowing the beam tail [83]. The number of atoms accelerated towards the surface is given by the current which in the available system is between 1.5pA and 21nA. A higher current gives faster milling and brighter imaging, though also a wider beam tip [82]. The system divides the area of the substrate it focuses on into pixels. The size of the pixels depends on the magnification. The current along with the time the ion beam dwells at each pixel, the dwell time, determines the dose each pixel receives [84]. A higher magnification gives pixels covering a smaller area on the substrate and thus higher resolution.

The SEM column is used for imaging of the surface, but the ion beam can also be used for the same purpose. When the beam scans over the surface, secondary particles such as electrons, ions and neutral atoms are released which can be picked up by a sensor (fig. 4.4a)). However one needs to be careful when using the ion beam as it will affect the surface to a larger degree than the electron beam [85].

Removal of material by milling (fig. 4.4b)) is done by using a higher current ion beam. The sputtering yield is dependent on the ion current, the ion energy, the angle of beam incidence and the substrate material. The etch rate can be increased by introducing etching gases which work by chemical removal of the reaction products. The sputtering can achieve resolutions down to tens of nanometers [79].

The FIB can also be used for deposition of materials (fig. 4.4c)) with the most common being platinum (Pt) and tungsten (W) and silicon dioxide (SiO_2). It is based on the same principle as chemical vapor deposition. The surface absorbs the precursor gasses and when exposed to the ion beam the gas decomposes and reaction products are deposited. The deposited materials are generally not very pure due to contaminants from the precursor gasses and the gallium ions. Features with dimensions down to 100nm laterally and a

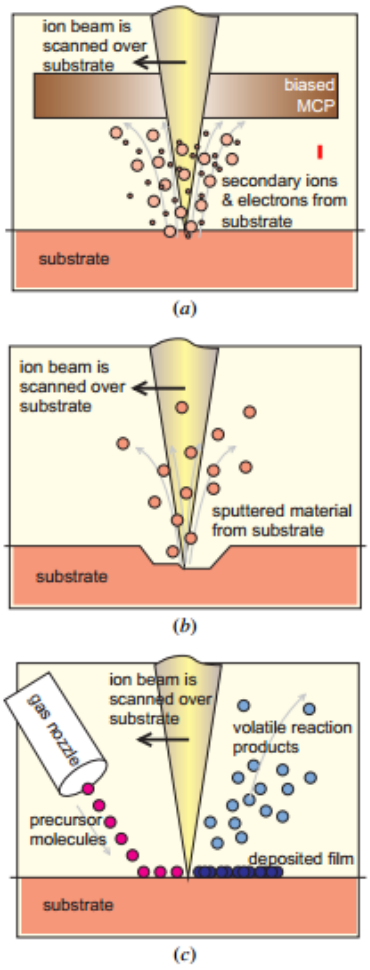

Figure 4.4: Principle of FIB a) imaging, b) milling, and c) deposition. Figure taken from Reyntjens and Puers [85].

thickness of 10nm have been deposited [85].

The FIB used for this Master's thesis is a FEI Helios NanoLab DualBeam FIB with an electron acceleration voltage of 0.5-30kV and ion acceleration voltage of 5-30kV. Before milling the stage is tilted at a 52° angle relative to the electron beam, meaning that the ion beam is normal to the surface. Both the electron beam and ion beam are focused and the height of the stage is chosen so that the area of focus does not change when tilting the sample. The use of the ion beam is avoided, unless necessary when aligning, to hinder ion beam damage of the surface.

When milling, the milling dose is defined by specifying a wanted depth in silicon. For example a dose of 666.65pC/μm^2 corresponds to an input of 0.1μm milling depth in silicon.

The milled pattern was defined using AutoScript, a limited programming language used to control the available FIB. The holes are milled in with a spiral scan starting from the center moving out to the edges. This has been found to give the best result compared to raster scan in several articles [80, 86] when milling holes in silicon. The scanning pattern of both spiral and raster scans can be observed in figure 4.5. The raster scan leads to more interhole scanning, which in turn leads to the entire working area being lowered compared to the rest of the sample. Raster scan also given unsymmetrical hole profiles and sidewalls with a higher angle to the surface normal [80]. A milling pattern can also be defined using a bitmap of the pattern. This, however, automatically uses raster scanning, therefore AutoScript has been used exclusively in this work when milling structures. The script completely finishes milling one hole before starting to process the next, ensuring as little as possible milling between each hole.

Before investigation of the cross section of the milled structures in the FIB, a material needs to be deposited over the structure, for this work platina has been used which gives a high contrast with silicon [80]. This is done to hinder redeposition of material in the holes, which will give an incorrect view of the structures. In this work, the Pt is deposited using an acceleration voltage of 30 kV and a current of 1.5pA which is lower than typically used for milling. This hinders the ions from further milling while depositing. When making the cross section in the FIB, an effort is done to make the section through the center of the hole.

4.3.1 FIB induced damage in silicon

Ga atoms will be implanted in the substrate when using the ion beam. This can create both vacancies and interstitials in the substrate lattice [87]. The implantation depth in Si is 27±9nm, 20±7nm, and 13±5nm for an Ga ion energy of 30kV, 20kV, and 10kV, respectively [88]. In photonic structures this causes large optical losses. In a waveguide etched with 30 kV Ga atoms without post-processing, losses of 3520 ± 90dB/cm have been measured. By using iodine as an etching gas and annealing at 300°C for 2 hours gave a loss of 196 ± 30dB/cm. Analysis using electron backscatter diffraction shows that the surface does not recrystallise during this treatment, suggesting that the amorphization is not the dominant cause of the

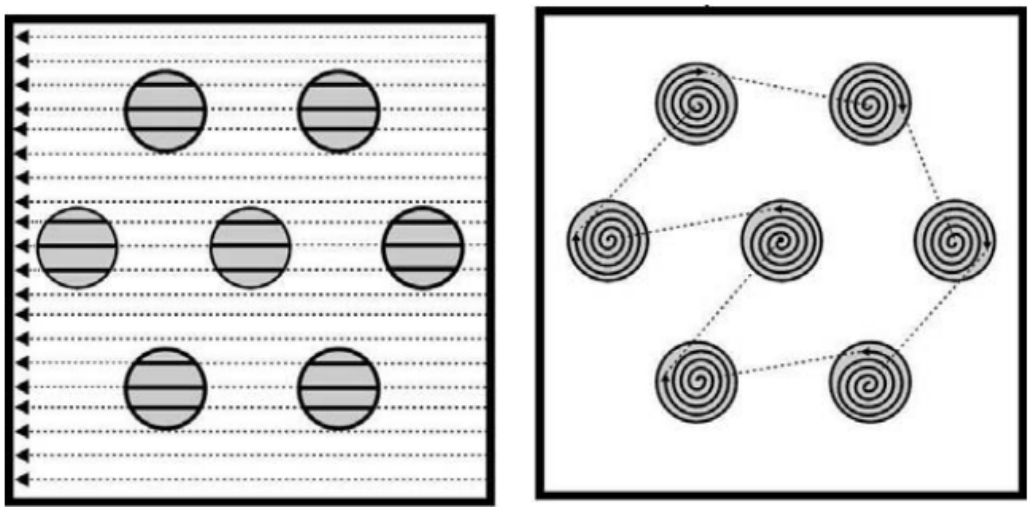

(a) Raster scan. (b) Spiral scan.

Figure 4.5: Scan routines. Figure taken from Hopman et al. [86].

optical losses [56]. Annealing a FIB fabricated Si structure at 670°C for 3000s makes the implanted gallium diffuse and precipitate at the surface [89]. This can cause adverse effects in photonic structures. Tao et al. [90] showed that annealing a photonic crystal structure at 78°C for 20 hours in an ethanol bath gave smoother sidewalls and a spectrum close to the expectations from computer simulations.

During milling, some of the sputtered atoms will redeposit on the substrate, creating unwanted features. Redeposition can be limited by using a fast scan according to Fu et al. [91] and Kolíbal et al. [83]. The ion beam will then move several times over the same feature, with fewer atoms being sputtered with each pass. A fraction of the beam is used to sputter away already redeposited material. However, Hopman et al. [80] found a large dwell time gives the least redeposition. A high current will give more redeposition [82]. Perfectly vertical sidewalls cannot be achieved using FIB partly due to redeposition, and partly due to the ion beam tail [81].

The beam tails are wider than the focus point of the ion beam and leads to rounding of already milled structures. Using lower acceleration voltage leads to wider tails and a higher degree of rounding. This results in more slanted sidewalls.

Amorphized silicon has a lower density than crystalline silicon, resulting in swelling of the irradiated area [86]. Kolíbal et al. [83] found that high energy ions gave more swelling than low energy ions when milling holes in silicon.

4.4 Inductively coupled plasma reactive ion etching

Inductively coupled plasma reactive ion etching (ICP-RIE) is a dry etch technique for removal of material using both a chemical and a physical process. A chemical process uses chemical reactions between introduced gaseous molecules and the sample surface to etch, usually an isotropic process. In a physical etch, material is removed by surface atoms being dislodged by ions accelerated towards the surface. It is an anisotropic process because the accelerated ions will only remove atoms in its path. Physical etching usually has a poor selectivity compared to chemical etching. In RIE, chemically reactive ions are accelerated towards the sample surface and both physically sputters away and reacts chemically with the surface. This results in the possibility of creating anisotropic etch profile and a good etch selectivity [14, ch. 7].

The ICP-RIE used in this work is an Oxford Instruments PlasmaLab System 100-ICP 180 which uses a combination of capacitive coupled plasmas (CCP) and inductively coupled plasmas (ICP) to generate and maintain the plasma. A plasma is a combination of free electrons, ions, radicals and neutral species. To maintain a plasma in the laboratory, energy is needed and is in this case of CCP supplied as a radio frequency (RF) voltage between a parallel anode and cathode pair. Both electrons and ions in the plasma are affected by the varying field, however, the heavy ions are not mobile enough to follow the oscillations of the electric field as the electrons are. Collisions between the fast moving electrons and the slow ions further enhances the plasma. A capacitor is placed between the RF supply and the anode plate so that electrons build up, creating a negative charge on the anode, usually called the table. This creates a potential difference V_b between the anode and plasma gas which drives the positively charged ions towards the negatively charged anode plate, and is the basis of RIE [92].

For ICP, the energy is supplied inductively through coils surrounding the plasma chamber instead of capacitively through plates, which results in a RF magnetic field. The magnetic field induces an electric field in the chamber which makes the plasma circulate in the plane parallel to the CCP plates. This movement will cause further ionization of the plasma similarly to CCP. The ICP does not drive ions towards the table. This enables the tuning of the plasma density (ICP) without affecting the incident energy of the ions hitting the table (CCP). Increasing the incident energy will increase the physical etch rate as the ions will hit the surface with a higher energy. Increasing the plasma density will increase both the physical and chemical etch rate due to a higher number of ions hitting the surface [92].

The composition and flow of the etch gases are in addition to the plasma important parameters in the etch process. This work uses a combination of SF_6 and CHF_3 injected in to the chamber simultaneously to etch a Si sample. SF_6 reacts with silicon atoms on the surface, creating SiF_4, a volatile compound, and thereby etches the surface [93]. The CHF_3 radicals forms a polymer on the silicon surface. The polymer will be physically etched by the incident ions. Surfaces that experience less ion bombardment will not have the polymer layer

Table 4.3: The ICP-RIE recipe.

Parameter	Amount	Unit
SF_6 flow	7.5	sccm
CHF_3 flow	50.0	sccm
Pressure	15	mTorr
CCP power	40	W
ICP power	600	W
Temperature	20	°C
Helium backing	10	mTorr

etched away and will therefore not be chemically etched. This creates anisotropic features as the bottom of trenches will be etched, but not the sidewalls [94]. A higher SF_6 concentration increases the etch rate as more fluorine radicals are created. An increased concentration of CHF_3 will increase the thickness of the passivation layer giving a slower etch rate, with the etch rate being inversely proportional to the thickness of the polymer layer [95]. Thus, the etch rate and anisotropy of the structures will be related to both the plasma density, the energy of the incident ions and gas composition and concentration.

The composition of etch gases used in this thesis is adapted from the work done in Vigen [33]. The specific recipe can be seen in table 4.3.

Before etching the chamber is conditioned by running the recipe for 20 minutes on a dummy wafer. This is done to ensure that the chamber conditions are as similar as possible for different etchings as residual gases and molecules absorbed on the chamber walls will influence the etch rates. All etches are done with a sapphire carrier wafer.

An important parameter in an etch process is the selectivity and is a measure on how fast one material is etched compared to another. Commonly, selectivity is interesting when considering mask materials. The formula for the selectivity between the substrate and mask is given by

$$\text{Selectivity} = \frac{\text{Etch rate of substrate}}{\text{Etch rate of mask}} \tag{4.1}$$

A high selectivity is often wanted, however, in nanoscale etching, high selectivity is not needed. Other parameters as accuracy and etch profiles are more important [14].

4.5 Plasma enhanced chemical vapor deposition

Plasma enhanced chemical vapor deposition (PECVD) is a process of depositing a solid material on a sample through a chemical reaction of a gas mixture in the reaction chamber. The sample is placed in an evacuated chamber, the precursor gases are introduced and RF

Table 4.4: The PECVD recipe.

Parameter	Amount	Unit
SiH_4 flow	8.5	sccm
N_2O flow	710	sccm
N_2 flow	161.5	sccm
Pressure	1000	mTorr
RF power	20	W
Table heater	300	°C
Chiller	20	°C

power breaks up the gas molecules, thus creating a plasma. The RF power is generated by two electrodes placed on the top and bottom of the reaction chamber. The created radicals form bonds with each other and deposits on the sample surface. Gaseous by-products are removed through the pumping system. For example, when depositing SiO_2, SiH_4 and N_2O are pumped into the chamber and the RF power breaks up the molecules, creating a plasma. The radicals in the plasma forms SiO_2, N_2, and H_2. SiO_2 forms as a film on the sample surface and N_2 and H_2 is carried away [14, ch. 11].

The reactions in a PECVD are very complex and not very well understood, therefore deposited films are found to not be very stoichiometric. Nonetheless, deposited silicon dioxide is nearly stoichiometric. The silicon dioxide film can have small amounts of hydrogen present as SiH or SiOH [14, ch. 11].

PECVD can be done at lower temperatures than other kinds of CVD, typically around 350°C for SiO_2. In addition to temperature, the variables important for the deposited film are electrode configuration and separation, RF power and frequency, gas composition, pressure and flow rate [96, p. 125].

The PECVD available at NTNU NanoLab is an Oxford Instruments PlasmaLab Systems 100-PECVD [70]. The recipe used can be seen in table 4.4.

4.6 Electron beam physical vapor deposition

Electron beam physical vapor deposition (E-beam evaporation) is a deposition technique where a material in an evacuated chamber is evaporated by exposure to an electron beam. The vapor expands in the chamber and condenses on the substrate which has a lower temperature than the vaporization temperature of the material. This is one of the easiest ways to deposit a thin film on a substrate. The chamber pressure needs to be lower than $1e{-}4$ mbar to make the mean free path of the evaporated atoms high enough [97]. The atoms can then travel in a straight line in the chamber and deposit on the sample. To produce a conformal coverage, the sample is rotated. An oxide can be deposited by introducing O_2

in the chamber while evaporating. However, different vapor pressures of different materials make exact control of the composition difficult [14]. The e-beam evaporator used in this thesis is a Pfeiffer Vacuum Classic 500 and has a chamber pressure of 5e–5 mbar [70].

The machine measures the deposited thickness using a vibrating quartz crystal. Evaporated atoms will deposit on the crystal as well as on the sample. However since the position of crystal and sample relative the the source is not the same, the thickness of the deposited films will also be different. The ratio of the deposited films is the tooling factor and has to be updated regularly for the instrument [98].

4.7 Reflectometer

The Filmetrics F20, the reflectometer available at NTNU NanoLab, uses spectral reflectometry to measure thickness and refractive index of a thin film using a light source with a 380nm to 1080nm wavelength range [70]. First the background reflection spectrum, $I_{bkg}(\lambda)$, is measured, then a reference reflection spectrum, $I_{ref}(\lambda)$. In this thesis a silicon wafer was used as a reference. Lastly, the reflection spectrum of the thin film sample, $I_{meas}(\lambda)$ is measured. The absolute reflectance is given by

$$R(\lambda) = \frac{I_{meas}(\lambda) - I_{bkg}(\lambda)}{I_{ref}(\lambda) - I_{bkg}(\lambda)} R_{ref}(\lambda) \tag{4.2}$$

where $R_{ref}(\lambda)$ is the theoretical reflectance of the reference sample [99]. How well the measured spectrum matches the theoretical is expressed in a goodness of fit parameter (GOF).

4.8 Profilometer

The profilometer used in this work is a Dektak 150 and is a contact stylus profilometer. A diamond tip is run over the surface of the sample and registers the height of the tip. It has a vertical resolution of 1Å [70]. It can be used to measure both surface roughness and etch depths.

4.9 Sample preparation

All silicon samples have been taken from polished 2 inch 250µm thick Si wafers with the $< 100 >$ direction exposed. The wafer was scribed and broken with a Dynatex DXIII into 7.5mm $\times$ 7.5mm samples.

Before use the samples were washed with acetone to remove fat and dust particles, then with ethanol and isopropanol to remove the acetone before drying and leaving residues. Lastly the sample is dried with nitrogen gas. Normally the samples were doused with spray

bottles, however, before spin coating the samples are first submerged in an ultrasonic acetone bath then in an ultrasonic ethanol bath, both for 5 minutes, before being blow dried with N_2. This is done because the spin coating process is much more sensitive to particles and contamination on the surface than the other processes in this work [14]. Before spin coating the samples were also dehydration baked on a hot plate for 10 minutes at 180°C. This is to remove water molecules from the sample surface and improve resist adhesion. The sample is afterwards placed on the spin coater wafer chuck and resist is applied with a pipette. Following the spin coating, the sample is again baked at 180°C for 60s and then placed on a cold plate. Before exposure in the EBL, the resist layer thickness is measured with the reflectometer.

When the cross section of samples are studied with the S(T)EM, the samples are cut using the same scriber as earlier. Before processing a scratch is made in the sample and the pattern is milled or etched near the end of the scratch. The sample is scribed from the edge to the end of the scratch, then broken. The structures will be destroyed if the scriber diamond tip moves over the sample so care has to be taken.

4.10 Sample types

Three different kinds of samples were investigated in this work. A clean silicon sample, 100nm silicon oxide on silicon, and 40nm titanium dioxide on silicon.

The silicon oxide thin film will be used as both a hard mask for etching in ICP-RIE and as a protective layer. When used as a hard mask, the silicon oxide layer will be patterned using the FIB. Only the oxide layer will be removed, leaving silicon exposed. The sample will then be etched using ICP-RIE using the recipe in section 4.4. The used etching gasses should have a selectivity with SiO_2 versus Si of around 10 [93]. Patterning of a hard mask using FIB has been done previously with different hard mask materials and substrates: Al_2O_3 on Si [56], Cr on Si [100], SiO_2 and Si_xN_y on InP [21], and SiO_2 on GaAs [101].

When used as a protective layer, the goal is to protect the Si from the beam tails, and thereby create more vertical walls in the Si layer. The silicon oxide may afterwards be removed, or left on the sample if it does not interfere with the light propagation. The protective layer may also hinder gallium ion implantation on the silicon surface, which gives lower losses [56]. The use of silicon oxide as a protective layer has been done previously by Tao et al. [23], then using a 240nm layer of SiO_2.

The titanium oxide thin film will also be used as a protective layer, and has previously been used by Hayat et al. [102].

Chapter 5

Results and discussion

The important parameters for assessing the fabrication of the photonic crystal sensor structure are surface roughness, sidewall angle, hole depth and hole bottom flatness.

Surface roughness of photonic structures has been investigated in relation to both waveguides [103, 104] and photonic crystals [105, 106, 107]. Lee et al. [108] found that the loss will be larger than 30 db/cm when the sidewall roughness exceeds 10nm for 500nm wide silicon on insulator waveguide. The scattering losses will increase linearly with the standard mean deviation of the roughness [104]. Roughness in photonic crystals will lead to both scattering losses [106] and a band gap shift [107]. Bogaerts et al. [106] found that scattering losses decrease with higher refractive index difference. As shown in section 3.3 roughness can also split the resonance of a photonic cavity. Gerace and Andreani [105] found that the quality factor of a cavity is reduced by roughness and disorder, however some cavity structures are less susceptible to the effects than others, both with regards to quality factor and scattering losses.

A high sidewall angle also leads to losses in a photonic crystal [109, 110, 111]. A sidewall angle of only 5 degrees can introduce a propagation loss of 80dB/cm in a photonic crystal waveguide [109]. These losses can be made smaller by making the holes deeper [111], making both the sidewall angle and hole depth important parameters. O'Faolain et al. [110] found that the sidewall smoothness and angle were the most important parameters in minimization of scattering losses.

As seen in section 3.2, the band structure changes with holes penetrating the substrate. If the first band structure is wanted, it is important that the hole bottoms are flat to avoid losses [111].

5.1 Deposition of thin films

SiO_2 was deposited using PECVD with the recipe described in section 4.5 for 78 s giving a thickness of 101.2nm (GoF = 0.9998) as measured by the reflectometer. This gives a deposition rate of 1.3nm/s for this recipe. During subsequent depositions it was found that the deposition would vary, ranging from 92.73nm to 101.6nm. The varying deposition rate is likely due to the condition of the chamber and the gases previously used. During depositions, the films will deposit on the chamber wall as well as on the sample. This along with molecules and gases absorbed in the chamber will influence the deposition rate. If a highly accurate thickness is required the chamber can be conditioned by running the process on a dummy wafer before sample processing. This will ensure equal chamber conditions before each deposition and a predictable deposition rate [112].

E-beam was used to deposit TiO_2. A 100nm film as measured by the instrument resulted in a 69.94nm (GOF = 0.9995) thick film as measured by the reflectometer. The tooling factor was adjusted accordingly. The following samples were deposited with 40nm as the input, giving film thicknesses of 43.21nm and 43.51nm when measured by the reflectometer. The results were close enough to the wanted 40nm thickness that no further adjustment of the tooling factor was performed.

Because the exact film thickness is usually not important for the results and there are small variations, the deposited thin films will be referred to as 100nm SiO_2 and 40nm TiO_2 and not their exact thicknesses.

5.2 Fabrication using focused ion beam

5.2.1 Determining optimal FIB milling voltage

Tests were performed to determine the optimal ion beam voltage when milling. A hexagonal pattern of holes, 270nm in diameter, was milled at 5kV, 8kV, 16kV, and 30kV, with a current of 9pA, 11pA, 14pA, and 9pA, respectively, and a dwell time of 1µs. The difference in current is due to the software only allowing set current values for each voltage. The milling dose was 666.65pC/µm^2. The results can be seen in figure 5.1. Some of the stuctures are deformed. This is due to drift from the ion beam, the sample and the stage. It can largely be avoided by leaving the sample in the chamber for several hours.

Milling at 5kV gave very poor results as seen in figure 5.1a. The ion beam could not focus on features of the required size order at this acceleration voltage, giving a large depression instead of individual holes. Kolíbal et al. [83] found that milling holes with a diameter of 300nm with a 5kV voltage gave less redeposition, flatter hole bottoms, and less swelling than at 30kV. Due to the inability to focus the beam, this could not be reproduced. They state that the chamber pressure must be lower than 2e–4 Pa during low energy milling. The FIB used in this work normally has a chamber pressure around 5e–4 Pa, with the instrument

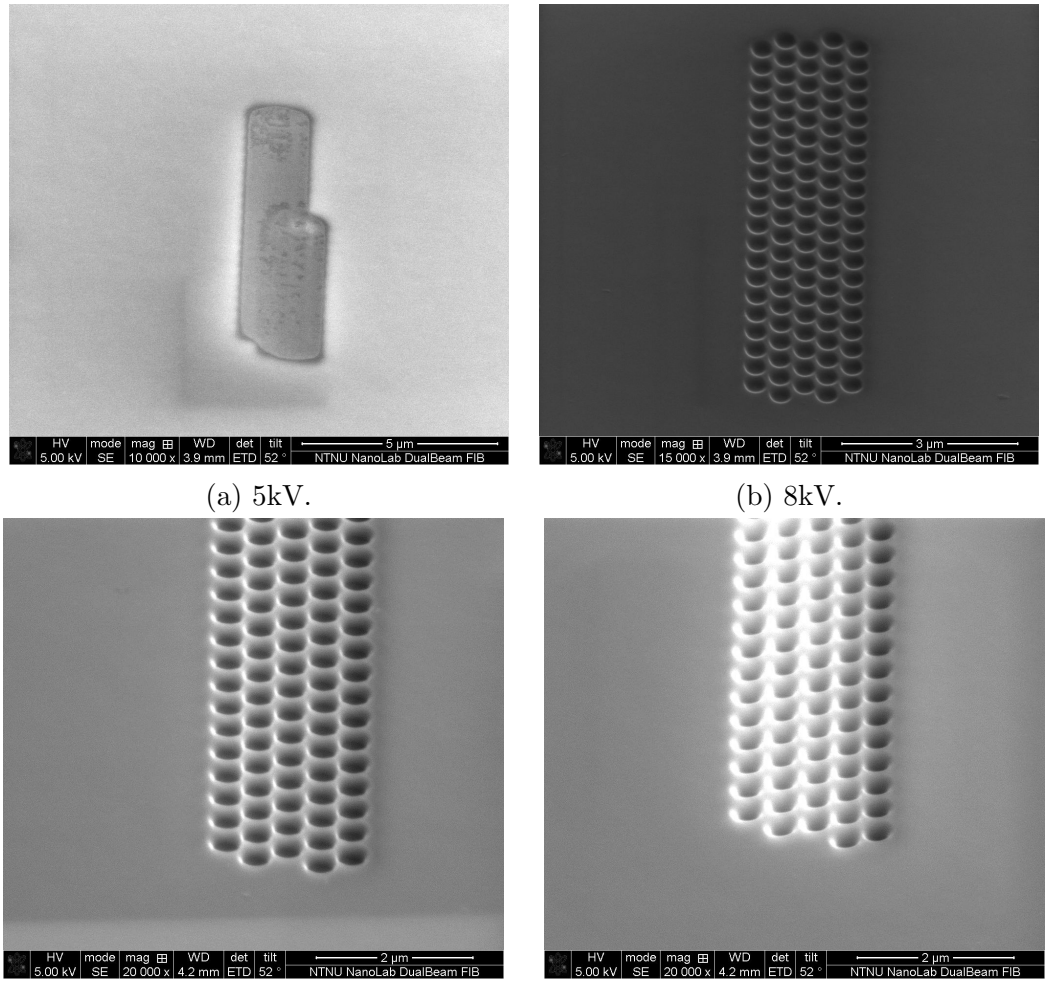

(a) 5kV. (b) 8kV.

(c) 16kV. (d) 30kV.

Figure 5.1: SEM pictures of the hexagonal hole structure milled with different acceleration voltages. Pictures taken at a 52° angle relative to the surface normal.

requirement to mill at a pressure below 1e–3 Pa. At too high pressures, the ions will deflect due to collisions with gas molecules and broaden the beam, leading to lower resolution. The difference in hole diameter is too small to explain the difference (300nm in the article versus 270nm for this structure), and would not noticeably affect the ability to focus on the milled structures.

The results of milling at 8kV is shown in figure 5.1b. On the surface the structure appears as expected, however, when the cross section is examined (fig. 5.3a), it is revealed that the holes are very shallow and rounded with high sidewall angles, which is unsuitable for use in the photonic crystal structure. The rounded bottoms and high sidewall angles are likely due to the wide tail of the low energy ion beam. The small depth is due to the low sputter yield from low energy ions as well as the scattering of low energy ions with gas molecules, keeping many atoms from reaching the intended target.

In figures 5.1c and 5.1d the milling can be seen with 16kV and 30kV, respectively. The surfaces of the two structures are similar. However, when investigating the cross sections in figures 5.3b and 5.3c it is observed that the 30kV structure is deeper and has more vertical sidewalls, likely due to the same effects discussed with regards to the structure milled at 8kV. The higher sidewall angle for lower milling voltages matches the results by Kolíbal et al. [83]. However, they found that lower voltage gave flatter hole bottoms, which does not match the results in figure 5.3. This may be due to the higher current used, therefore another milling was done with 16kV using a current of 3.4pA with the result shown in figure 5.2. The hole is slightly deeper, likely due to a smaller probe size and therefore a more focused beam. With regards to sidewall angle and hole bottom shape, the difference is negligible.

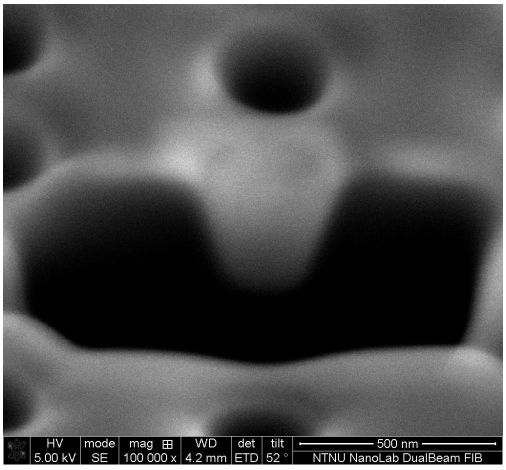

Figure 5.2: Cross section of a hole milled with 16kV and a current of 3.4pA.

It is important to note that in the cross sectional images, the section may not go through the center of the hole even though an effort is made to make it as close as possible. An inaccurate cross section will give a wrong hole profile, both with regards to sidewall angle,

hole depth and hole bottom flatness. The difference in hole size in figure 5.3c is due to the section not going through the center of the holes on the sides.

Due to vertical sidewalls being important to achieve high transmission, 30kV is chosen as the optimal milling voltage. The downside of milling with a high voltage is deeper implantation of gallium ions which will result in higher losses. A 10μm wave guide implanted with 16.02pC/μm^2 at 30kV has been found by Schrauwen [56] to have a loss of approximately 4000dB/cm, compared to a loss of approximately 3000dB/cm when implanted with 10kV ions. The high losses makes FIB unsuitable for direct milling of large photonic structures. For smaller structures the difference between the losses is not large enough to defend milling with lower energy ions. Note that the implanted ion dose is not the same as the milling dose as most of the ions hitting the sample surface will be removed along with the milled material.

5.2.2 Determining optimal FIB milling current

The current determines the probe size and the milling time. Milling the hexagonal hole structure with different currents at 30kV was done to find a compromise between the needed resolution and time. The milling dose was 666.65pC/μm^2. The current also affects the unintentional milling of the substrate during alignment of the pattern on the surface and adjustment of the focus, as a high current will affect already milled features on the sample surface quicker than lower currents.

The cross section of holes milled with 26pA, 9pA, and 1.5pA is shown in figure 5.4 with sidewall angle and hole depth measurements. The angle measurements in this work should only be taken as an approximation. The rounding of the walls and the diffuse interface between the silicon and platinum makes precise angle measurements difficult and prone to errors. The diffuse interface is due to the signal not just originating from the surface of the sample, but from the entire secondary electron interaction volume. Since the interface is rounded inside the sample, the interface becomes blurry.

From the cross sections it is observed that the best hole shape is created milling with 1.5pA, due to the smaller ion beam probe for smaller currents. However, milling one hole takes 26 seconds, resulting in that several hours is needed to mill the photonic crystal. Due to limited available instrument time, 9pA was chosen as the optimal current for this work, because 4 seconds is needed to mill one hole at the specified dose.

There is a difference in depth, which does not follow a linear relationship with the current. The hole milled with 9pA shows the largest depth, 374.5nm, while the two other holes are significantly shallower at 281.6nm and 296.1nm. It could be expected that the depth would increase with lower current as there will be less redeposition and a smaller probe size. This, however, is not seen here. One possibility is that the system could be poorly calibrated and that the current marked as 9pA by the system is in fact higher, giving a higher dose than specified, and thus a deeper hole.

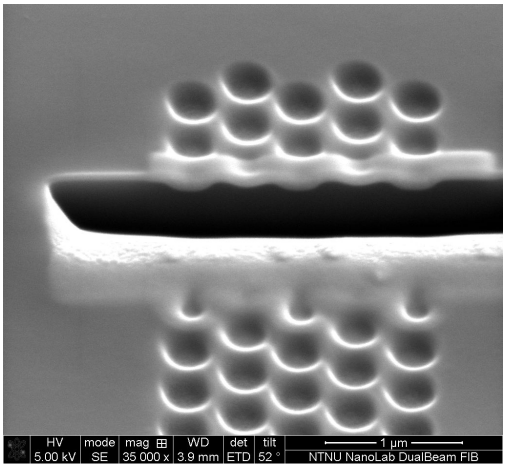

(a) 8kV.

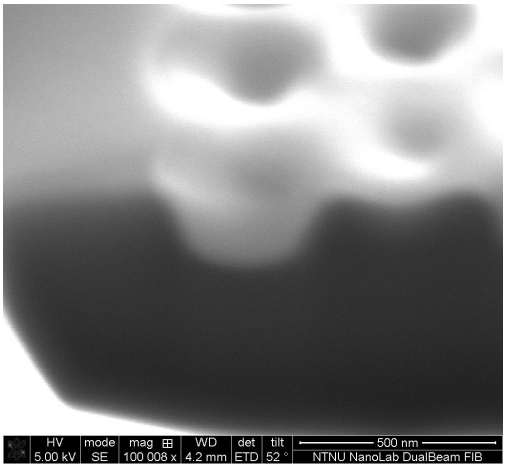

(b) 16kV.

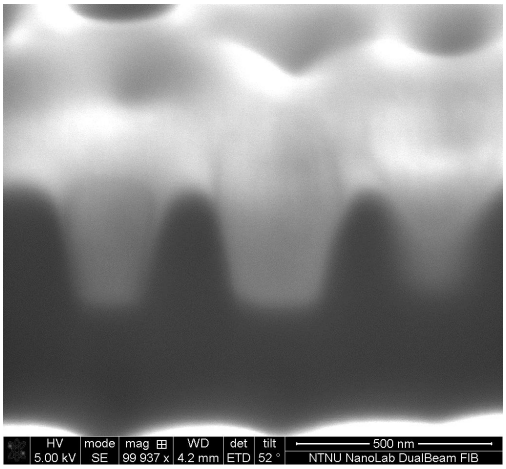

(c) 30kV.

Figure 5.3: SEM pictures of hole cross sections from figures 5.1b, 5.1c, and 5.1d. The lighter areas are deposited Pt, the darker areas are Si. Pictures taken at a 52° angle relative to the surface normal.

The dose that has been used corresponds to an input depth of 0.1µm. It is clear that the dose versus milling depth for this instrument is wrong, at least for these kinds of features and depths. It would be possible to imagine that the system is calibrated for milling of larger features, but then observed depth would be smaller than expected as milled atoms would have a higher chance of escaping and not redepositioning in large features.

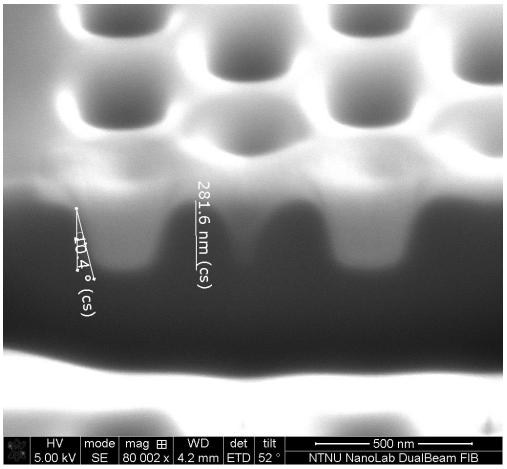

(a) 26pA, 10.4 degrees, 281.6nm.

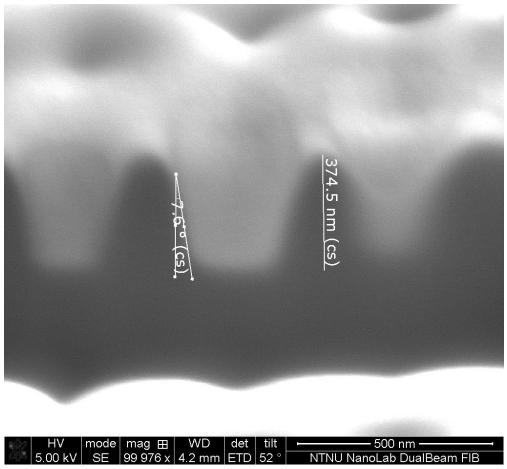

(b) 9pA, 7.6 degrees, 374.5nm.

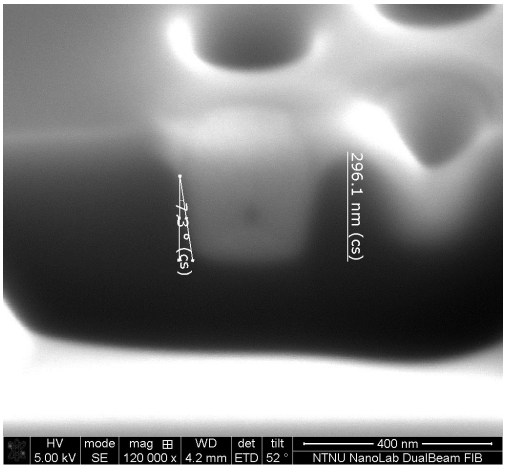

(c) 1.5pA, 7.3 degrees, 296.1nm.

Figure 5.4: SEM pictures of cross sections of holes milled with different currents at 30kV, with the current used, sidewall angle, and depth specified.

5.2.3 Determining optimal FIB milling dwell time

An investigation in to the effect of varying the dwell time was performed on the three different sample types. The results of milling holes in silicon without a protective layer using dwell times of 1ms, 100µs, 10µs, and 1µs are shown figure 5.5. The holes were milled at 30kV with a 9pA current and a dose of 666.65pC/µm^2. Close ups of each cross section with sidewall angle measurements can be seen in figure 5.6.

The same procedure was done for holes with a dose of 1.33nC/µm^2, corresponding to a depth input of 0.2µm. As found in section 3.2, deep holes will also produce a photonic band gap, and may simultaneously make fabrication easier. The results are shown in figures 5.7 and 5.8.

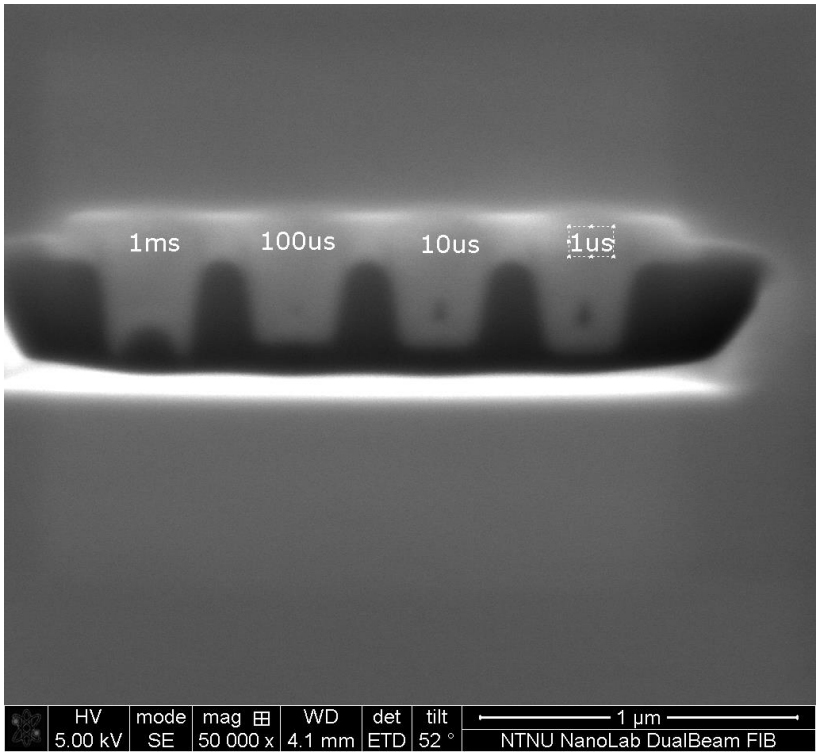

Figure 5.5: Cross sections of holes milled in silicon using dwell times of 1ms, 100µs, 10µs, and 1µs.

Of the shallow holes, the best sidewall angle was achieved with a 1ms dwell time, but has an unwanted hole bottom shape. The build-up of material in the middle is likely due to redeposition during milling. The ion beam mills from the inside of the hole, moving in a circular pattern outwards. The material milled may then redeposit on the bottom of the newly milled center, creating a mound. A high dwell time means that the ion beam spends a longer time at each pixel, giving fewer scan iterations, and the ion beam mills each pixel

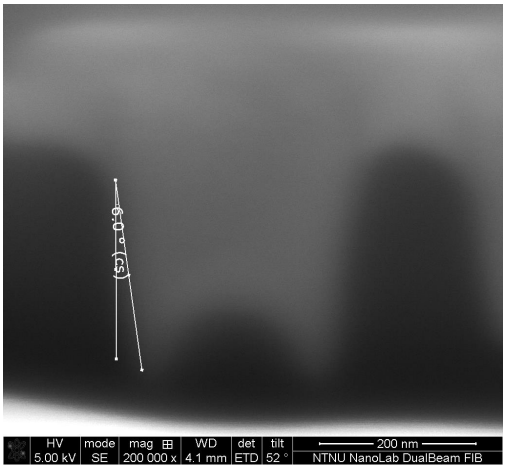

(a) 1ms, 6.0 degrees.

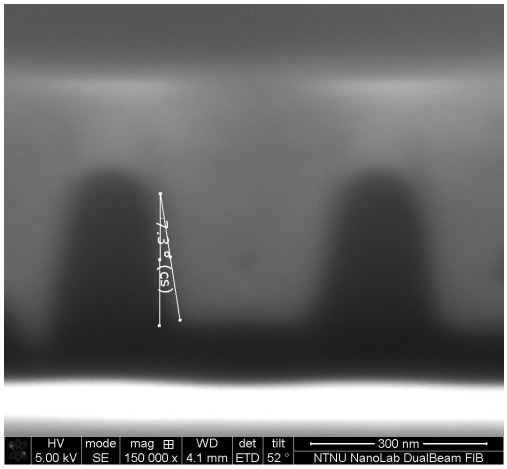

(b) 100µs, 7.3 degrees.

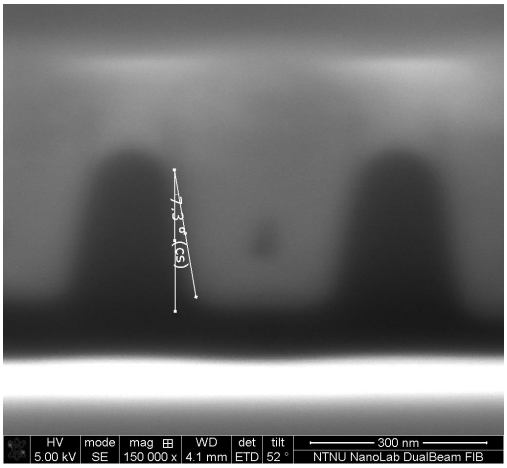

(c) 10µs, 7.3 degrees.

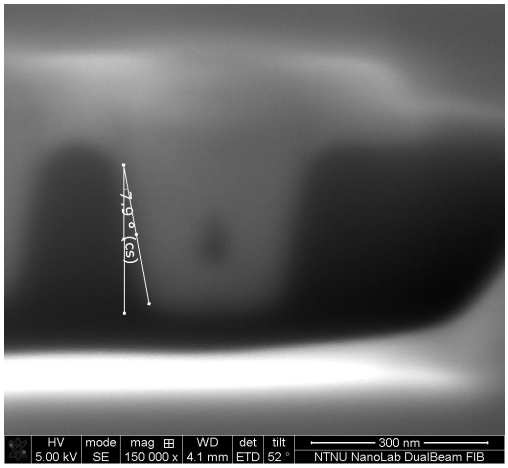

(d) 1µs, 7.9 degrees.

Figure 5.6: Close ups of the holes from figure 5.5 with sidewall angle measurements.

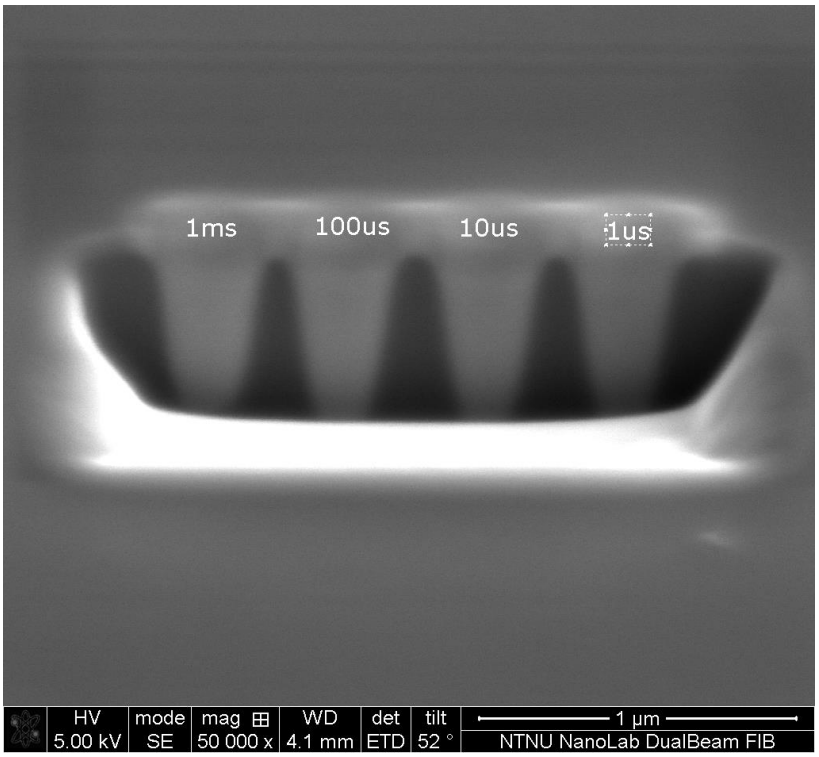

Figure 5.7: Cross sections of holes milled in silicon using dwell times of 1ms, 100µs, 10µs, and 1µs.

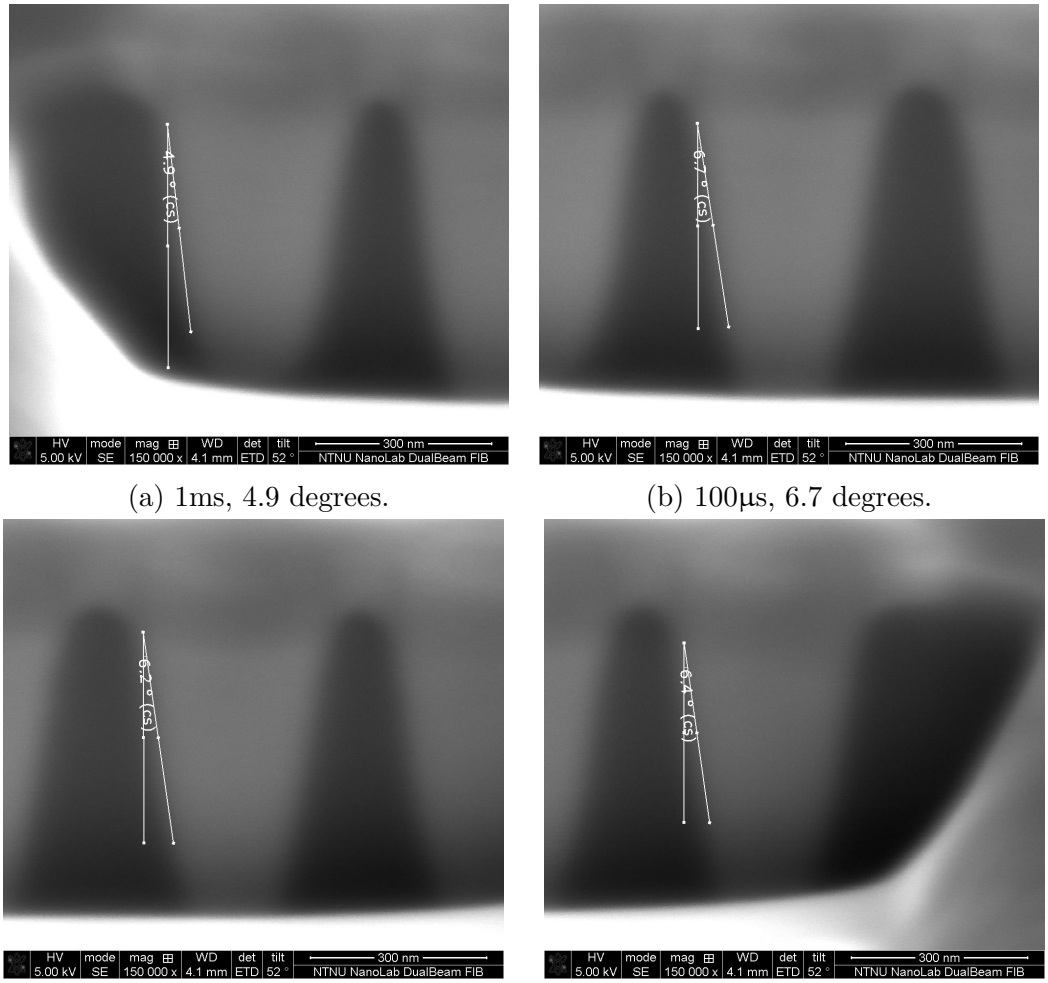

(a) 1ms, 4.9 degrees.

(b) 100µs, 6.7 degrees.

(c) 10µs, 6.2 degrees.

(d) 1µs, 7.9 degrees.

Figure 5.8: Close ups of the holes from figure 5.7 with sidewall angle measurements.

fewer times than at a low dwell time. With lower dwell time, less material is milled at each iteration, producing less redeposition for each pass and the redeposited material is milled away at the next. At low dwell times the bottom gets a downward rounded shape. These results match the findings of Kolíbal et al. [83], where it was found that a high dwell time gave a W-shaped hole, while a low dwell time gave a V-shaped hole. Different from the findings presented here, they found that intermediary dwell times also gave W-shaped holes, however, the authors only milled 50nm deep holes. When looking at the deeper holes milled for this work it is observed that the W-shapes disappear. This may point to the optimal dwell time with regards to hole bottom flatness being strongly linked with hole depth. The hole profiles of different depth holes milled using 1ms dwell time is shown in figure 5.9, and the findings support this claim.

The sidewall angle of the shallow holes are relatively similar for dwell times of 100µs, 10µs, and 1µs, with 1µs coming out worst by a small margin. This pattern is repeated for the deeper holes. All the deep holes have rounded bottoms, but in a SOI structure this will be in the oxide layer and therefore less detrimental to the performance of the photonic crystal. The deeper holes also have better sidewall angles than the shallower holes. Low sidewall angles for high dwell times is supported by Hopman et al. [80]. Both the angled sidewalls and hole bottom mound are the results of redeposition. This points to that the dwell time has an effect on where the redeposition occurs. Redeposition is a pure geometrical effect, a sputtered atom will redeposit on a surface in its path [91]. At high dwell times the ion beam mills deeper at each pixel, making it harder to escape and redeposit on the previously milled sidewalls, an example can be seen in figure 5.10. This gives a higher probability that a milled atom will redeposit on the hole bottom than on a sidewall, creating lower sidewall angles and mounds on the hole bottoms. If the holes were milled from the outside and inwards, then it is likely that the opposite would be observed, that a high dwell time gives a higher probability of redeposition on sidewalls. This also explains the bowl shape at lower dwell times, as milled atoms more frequently redeposit on the sidewalls, making milling there slower than in the center of the hole as redeposited material has to be remilled.

The change in hole shape from W to V in figure 5.9 can be explained in the same manner. When the redeposited mound is milled, the sputtered material has a free path towards the sidewalls where it can redeposit. The redeposited material will have slow milling rate at the sides of the hole until the center of the hole is milled faster than at the sides.

There is a trend towards deeper holes for higher dwell times (at least for the shallow holes, the depth of the deeper holes cannot be properly seen due to the cross section cut not going deep enough). This can also be explained by redeposition. Since there is not a mound build up at low depths for high dwell times, the ion beam can mill more in the center of the hole, at the cost of the side wall angle.

The deep holes have better sidewall angles than the shallow holes. The opposite could be expected as it will be harder for an atom milled at the bottom of a deep hole to escape compared to one milled at the bottom of a shallow hole, and thus creates more sidewall

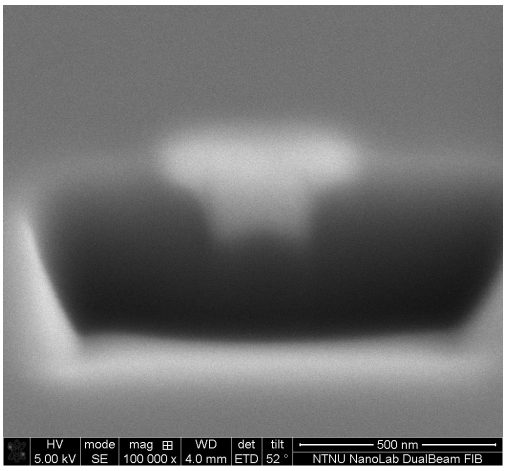

(a) 200.00pC/μm^2.

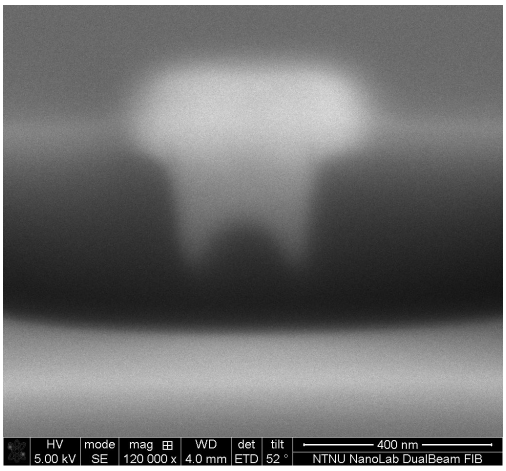

(b) 466.66pC/μm^2.

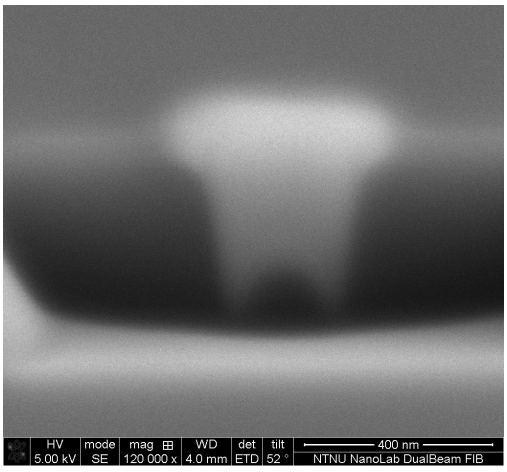

(c) 666.65pC/μm^2.

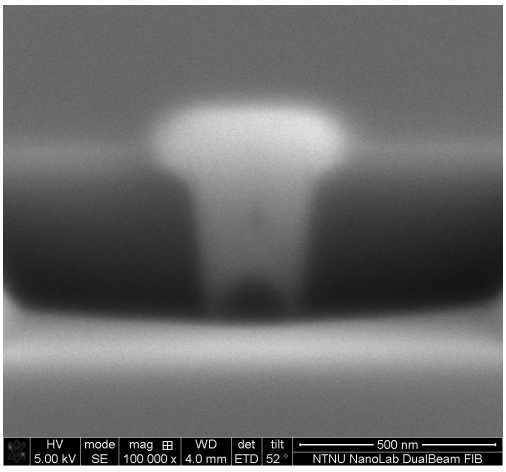

(d) 933.31pC/μm^2.

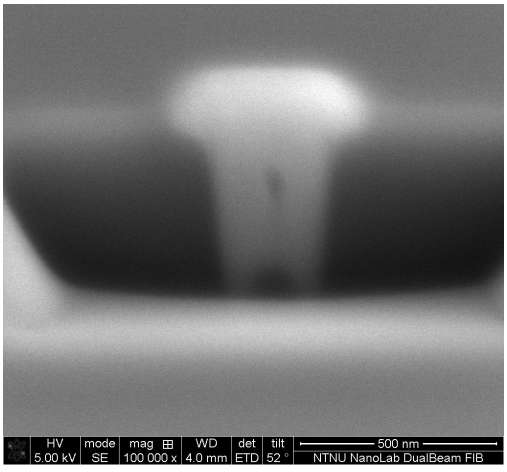

(e) 1133.31pC/μm^2.

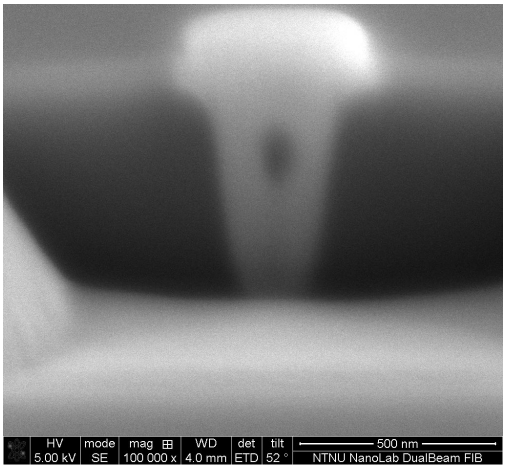

(f) 1399.97pC/μm^2.

Figure 5.9: Holes of increasing depth milled with a dwell time of 1 ms.

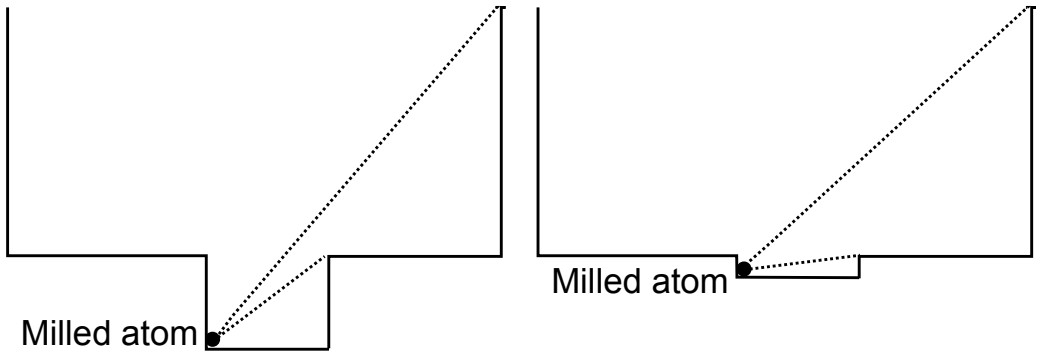

(a) High dwell time. (b) Low dwell time.

Figure 5.10: A schematic explanation of the redeposition possiblities of an atom milled at high and low dwell times.

redeposition. The observed results could be due to measurement errors or a difference in ion beam focus during milling, or possibly an unknown milling effect.

The same dwell time evaluation was done for the SiO_2 and TiO_2 thin film covered samples. The results using the same parameters as previously can be seen in figures 5.11, 5.12, 5.13, and 5.14 for the sample covered with 100nm SiO_2 and in figures 5.15, 5.16, 5.17, and 5.18 for the sample covered with 40nm TiO_2. The same pattern of hole bottom dependence on dwell time is observed. The exact dependence varies a bit, for example in figure 5.15 it is seen that there is a slight mound in the hole milled using a dwell time of 100µs which is not present in the uncovered silicon milled using the same dwell time. This can be due to the TiO_2 layer being milled at a slower rate than the silicon, corresponding to a shallower hole milled in silicon, and thus not being on that same stage on the development from a W to a V shaped hole. The corresponding hole milled in the SiO_2 covered sample does not have such a mound, which may mean that SiO_2 has a milling rate closer to Si than TiO_2. In fact the milling rate of silicon is $0.22\mu m^3/nC$, $0.23\mu m^3/nC$ for SiO_2 [113], and less than $0.15\mu m^3/nC$ for TiO_2 [102].

The evolution of the side wall angles also follow the same pattern with the best angle being achieved with the highest dwell time. The SiO_2 covered sample has slightly better sidewall angles than the uncovered sample. Height measurements (measured similarly to the height measurements shown in figure 5.4) show that the holes milled in the silicon oxide covered sample are deeper for the same dose. For example, the shallow hole milled with a dwell time of 1µs was measured to be 362nm deep for the uncovered sample while being 412nm deep for the oxide covered sample. This is due to the higher milling rate of silicon oxide. The holes milled in uncovered silicon improved their sidewall angles when the depth increased. This trend is not seen for the SiO_2 covered samples. The deep holes have poorer sidewall angles than the shallow holes as expected due to redeposition. This points to that

there may be a depth interval where the sidewall angles improves as the hole deepens, before the sidewall angle worsens.

When light propagates through the silicon oxide covered sample, the light will be mostly confined to the silicon layer, where the hole has the best sidewall angle when covered with silicon oxide. The silicon oxide layer can also be selectively etched, leaving only the silicon [114], and remove the rounded tops of the holes.

For comparison, the shallow hole milled with a dwell time of 1µs in the TiO_2 covered sample is only 228nm deep due to the low sputter rate of titanium dioxide. The holes milled in TiO_2 and Si show the best side wall angles. This is a result of the slow etching layer protecting the underlying silicon from the beam tails. The titanium dioxide layer acts as a beam stop for the slow etching beam tails. A problem with the TiO_2 layer is that it is almost impossible to selectively remove [115, 116]. The layer may interfere with and absorb light propagating through the photonic crystal. The sidewall angles increases for the deep holes similar to the silicon oxide covered samples. However, the holes milled in the titanium dioxide covered samples are shallower than the corresponding holes milled in the two other sample types, which does not support the hypothesis that there is an interval where the sidewall angle improves with increasing depth. It is apparent that the relation between sidewall angle and hole depth needs to be studied further.

It is clear that the optimal dwell time depends on the hole depth and substrate, however there is a clear trend towards better sidewall angles using higher dwell times. The best result was achieved using a dwell time of 1ms, a dose of 666.65pC/µm^2 on an titanium dioxide covered sample. Unfortunately the software bundled with the FIB used in this work does not allow the specification of dwell time when using AutoScript [117]. Thus the standard dwell time of 1µs has to be used for the photonic structure in this work. The dwell time can be changed with a software upgrade, making this work useful for future fabrication of photonic crystals using FIB.

Though it is not known how the titanium dioxide thin film will affect the propagation of light, it has been shown here that depositing a material with slower milling rate than the substrate produces more vertical sidewalls. If titanium dioxide significantly affect the propagation of light, then a different material could be utilized as a protective layer. For example aluminium oxide has a milling rate of only 0.08µm^3/nC and does not absorb light at 1.55µm to a great degree.

5.2.4 Hole cross section

Holes milled at 30kV using a current of 9pA and a dwell time of 1µs were milled in the three different sample types, cleaved using the scriber and studied using the S(T)EM. Both holes with a dose of 666.65pC/µm^2 and 1.33nC/µm^2 and with diameters of 270nm and 140nm were investigated. The scribing and breaking is an inaccurate process, thus the position a hole is cleaved is based on chance. Therefore no measurements are presented as the they

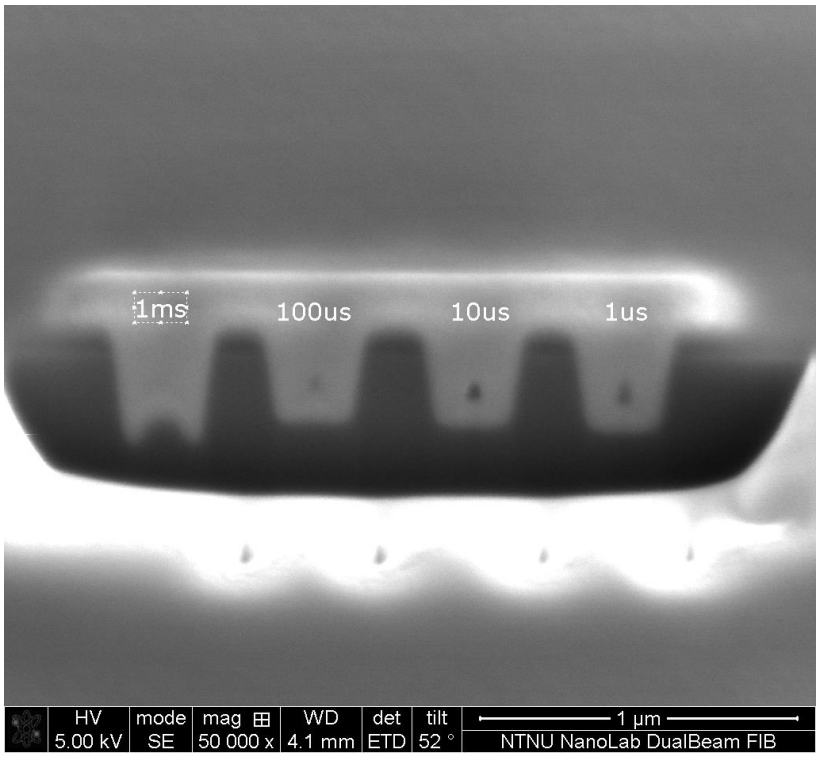

Figure 5.11: Cross sections of holes milled in silicon with a 100nm silicon oxide film using dwell times of 1ms, 100µs, 10µs, and 1µs.

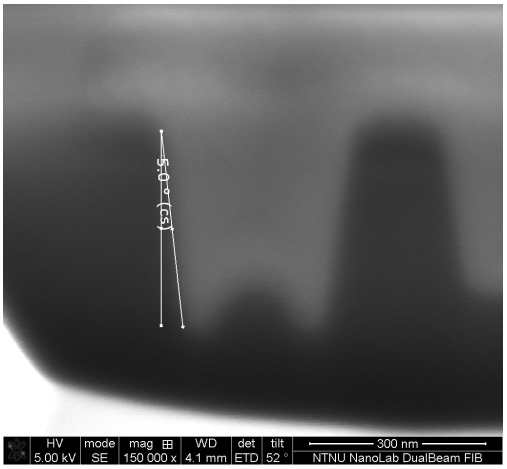

(a) 1ms, 5.0 degrees.

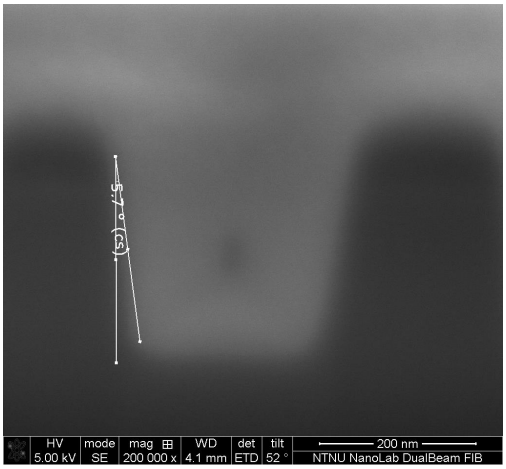

(b) 100µs, 5.7 degrees.

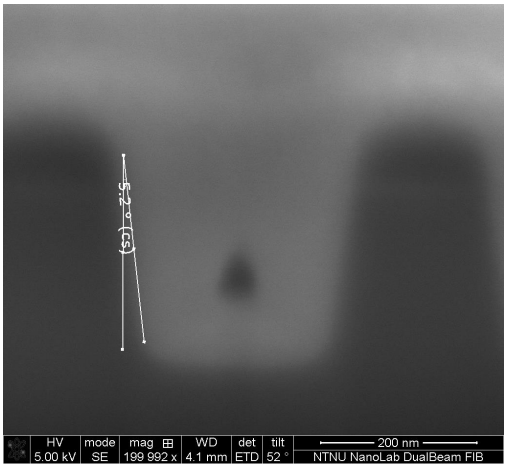

(c) 10µs, 5.2 degrees.

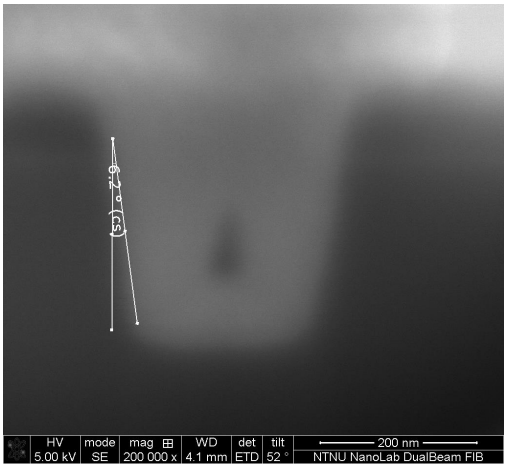

(d) 1µs, 6.2 degrees.

Figure 5.12: Close ups of the holes from figure 5.11 with sidewall angle measurements.

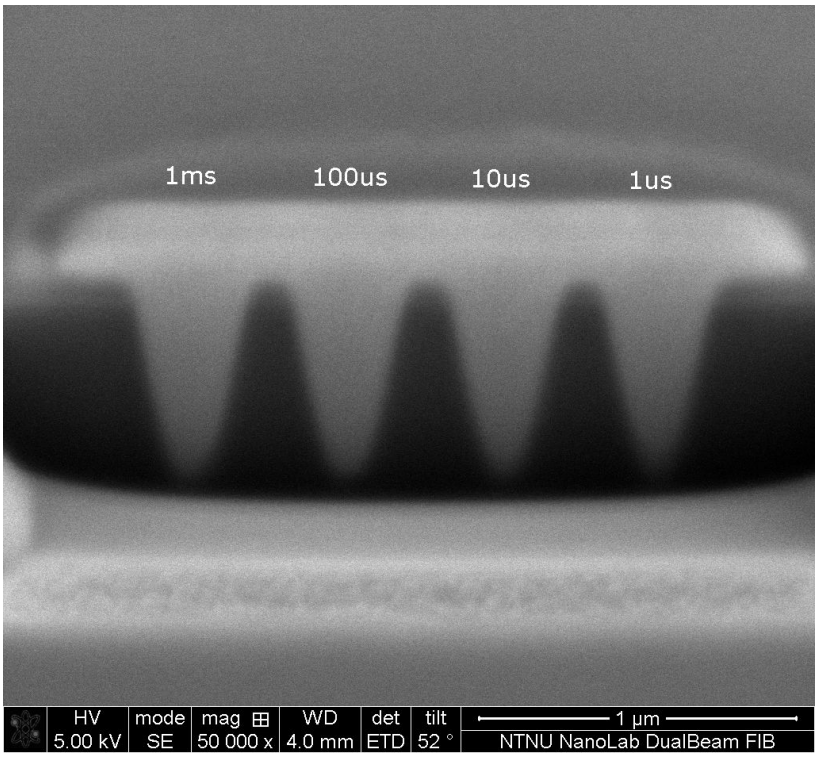

Figure 5.13: Cross sections of holes milled in silicon with a 100nm silicon oxide film using dwell times of 1ms, 100µs, 10µs, and 1µs.

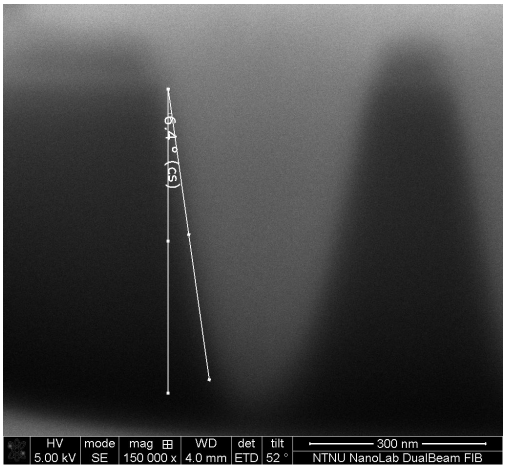

(a) 1ms, 6.4 degrees.

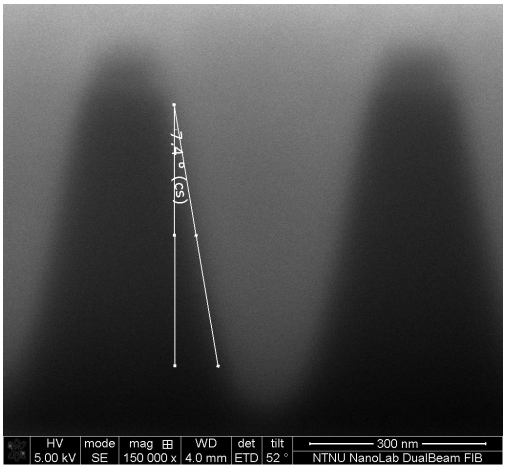

(b) 100µs, 7.4 degrees.

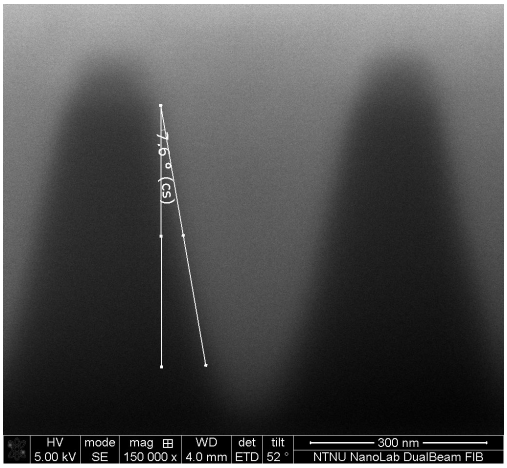

(c) 10µs, 7.6 degrees.

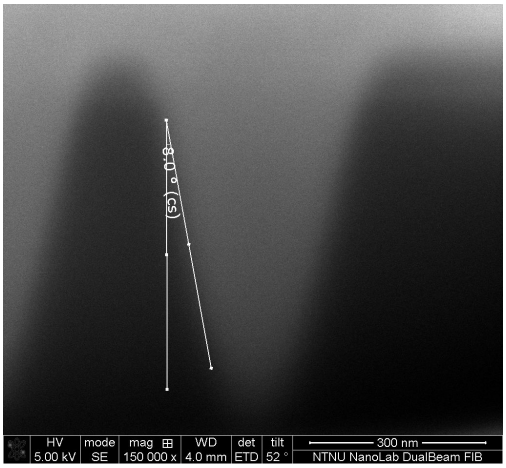

(d) 1µs, 8.0 degrees.

Figure 5.14: Close ups of the holes from figure 5.13 with sidewall angle measurements.

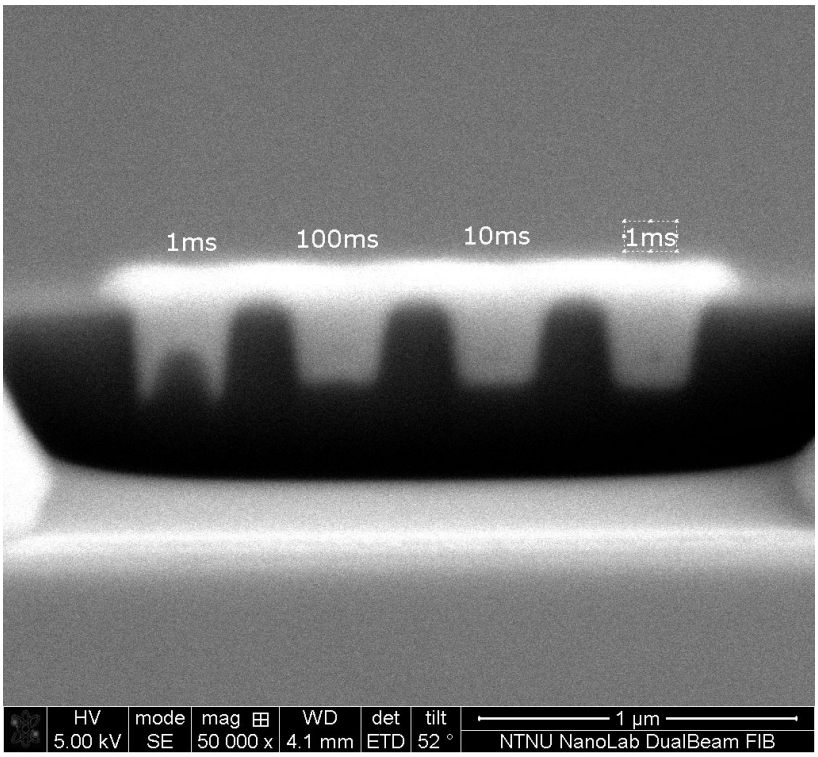

Figure 5.15: Cross sections of holes milled in silicon with a 40nm titanium dioxide film using dwell times of 1ms, 100µs, 10µs, and 1µs.

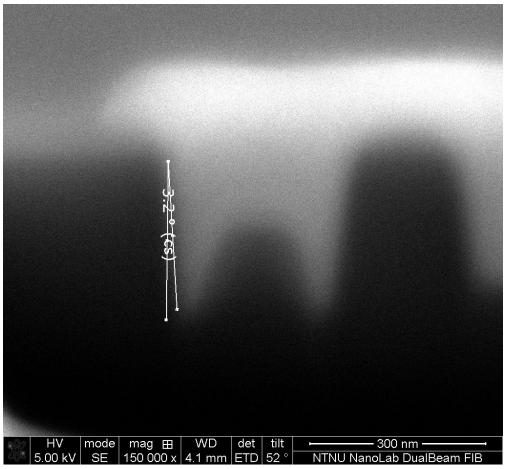

(a) 1ms, 3.2 degrees.

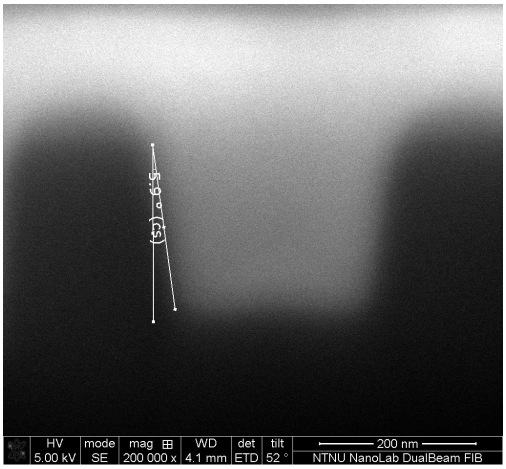

(b) 100µs, 5.9 degrees.

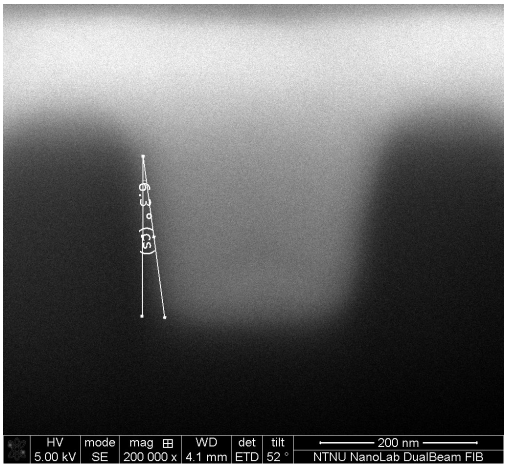

(c) 10µs, 6.3 degrees.

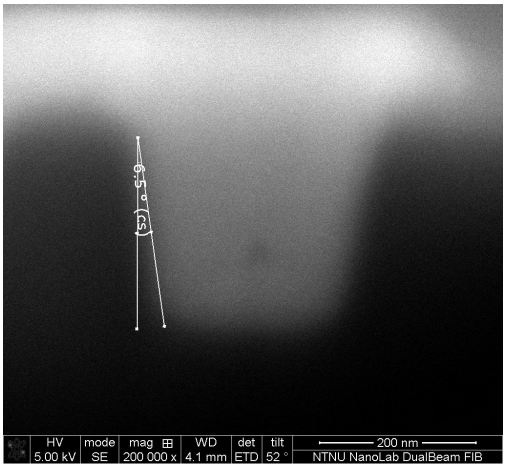

(d) 1µs, 6.5 degrees.

Figure 5.16: Close ups of the holes from figure 5.15 with sidewall angle measurements.

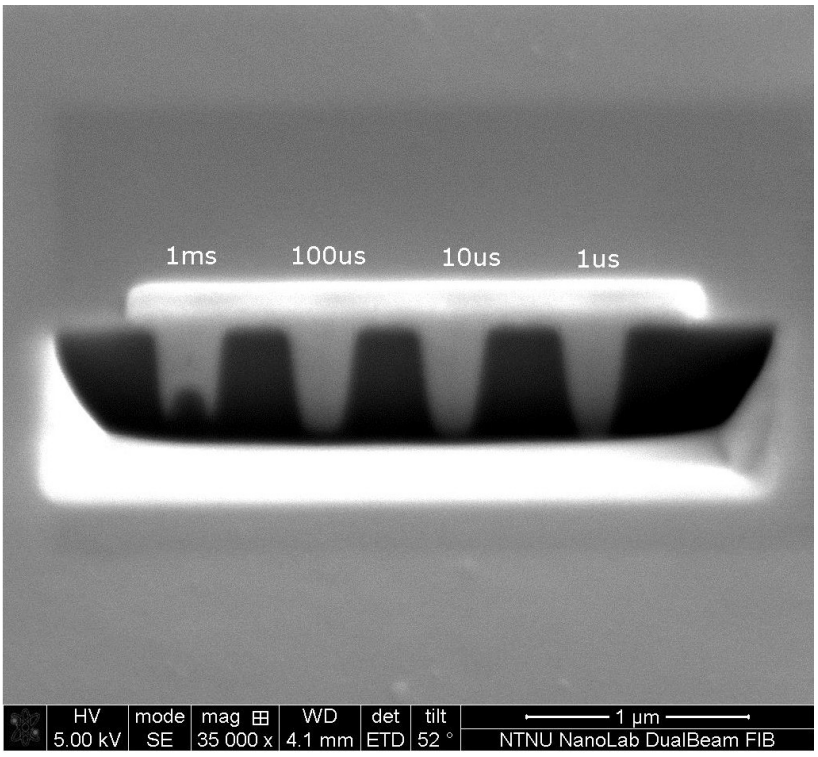

Figure 5.17: Cross sections of holes milled in silicon with a 40nm titanium dioxide film using dwell times of 1ms, 100µs, 10µs, and 1µs.

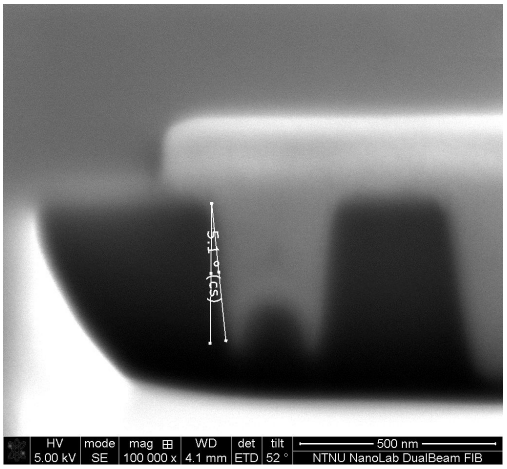

(a) 1ms, 5.1 degrees.

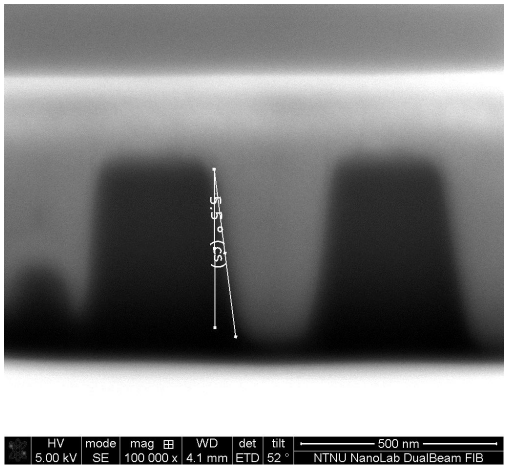

(b) 100µs, 5.5 degrees.

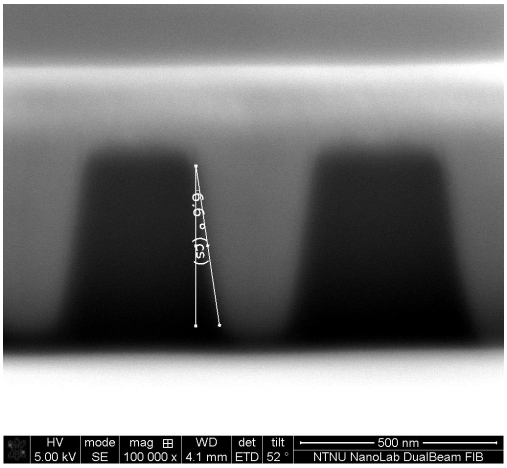

(c) 10µs, 6.6 degrees.

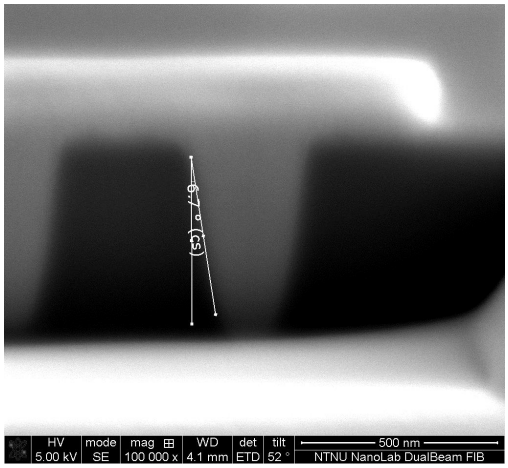

(d) 1µs, 6.7 degrees.

Figure 5.18: Close ups of the holes from figure 5.17 with sidewall angle measurements.

will vary depending on the cleaving.

In figures 5.19 and 5.20 the cross sections for the shallow holes (a dose of 666.65pC/μm^2) and deep holes (1.33nC/μm^2), respectively, are presented. The sidewalls are all smooth with little redeposition. There is some hole bottom roughness due to redeposition, seen in figures 5.19a and 5.20a. The roughness can create scattering losses with the magnitude of these losses depending on the field strength at the site of the roughness. Since the hole bottoms of the shallow holes are located closer to the silicon layer in a SOI structure, this will create more scattering losses. In figure 5.20c there is a large piece of silicon at the top of the hole. This is too large to be an effect of redeposition and is probably silicon dust from the scribing and breaking. For all the holes there is clear surface swelling around the edge from amorphizing of the silicon.

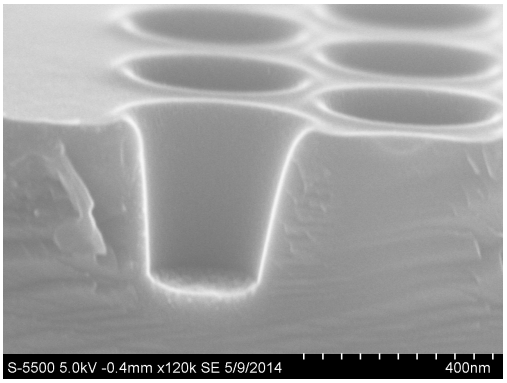

(a) Angled view of a hole with a specified diameter of 270nm.

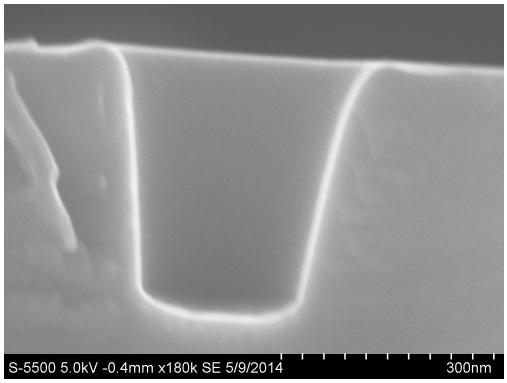

(b) Cross section of a hole with a specified diameter of 270nm.

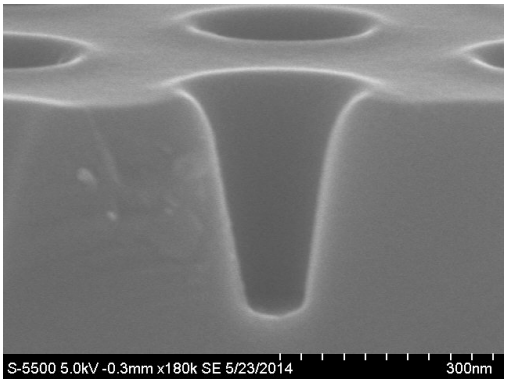

(c) Angled view of a hole with a specified diameter of 140nm.

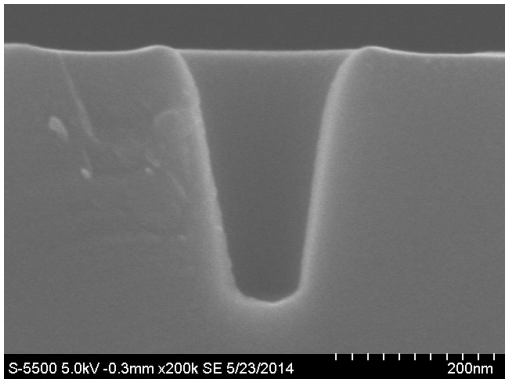

(d) Cross section of a hole with a specified diameter of 140nm.

Figure 5.19: S(T)EM pictures of shallow holes milled in silicon.

The degree of hole bottom roughness is unclear from the S(T)EM pictures of the holes milled in the SiO_2 covered samples (figures 5.21 and 5.22). The layer of SiO_2 can clearly be

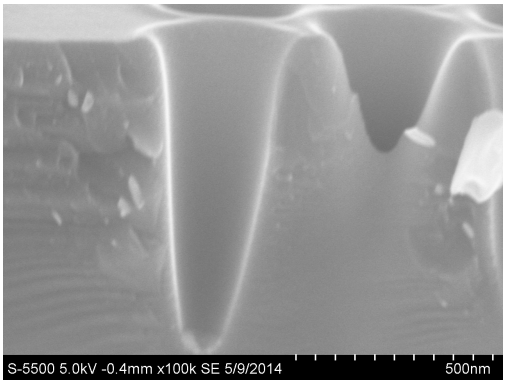

(a) Angled view of a deep hole with a specified diameter of 270nm.

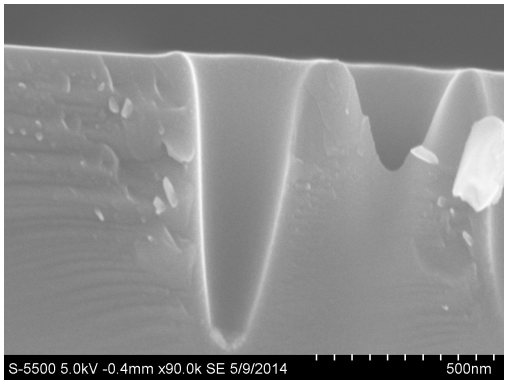

(b) Cross section of a deep hole with a specified diameter of 270nm.

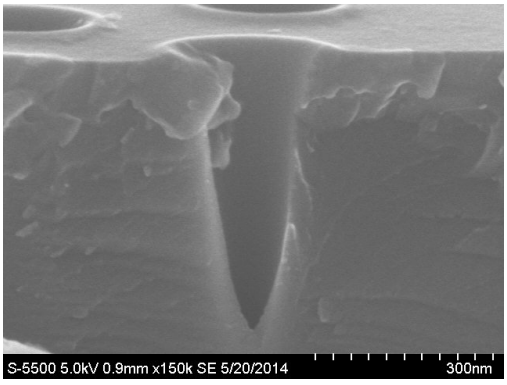

(c) Angled view of a deep hole with a specified diameter of 140nm.

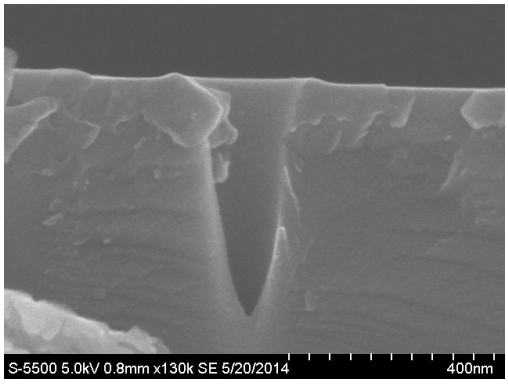

(d) Cross section of a deep hole with a specified diameter of 140nm.

Figure 5.20: S(T)EM pictures of deep holes milled in silicon.

observed in the pictures. The surface is rough, which can cause losses as roughness inside the holes, but to a smaller degree as the field strength will not be as strong on the SiO_2 surface as in the holes [118]. Roughness on an uncovered silicon surface would affect the wave to a larger degree. No swelling is observed around the holes. This is likely the result of that silicon oxide is already amorphized. Thus there is no change in state from crystalline to amorphous during milling as with silicon, with a corresponding change in density. The sidewalls are smooth similarly to the holes milled in uncovered silicon.

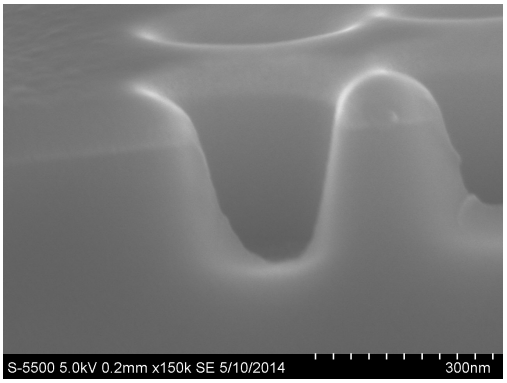

(a) Angled view of a hole with a specified diameter of 270nm.

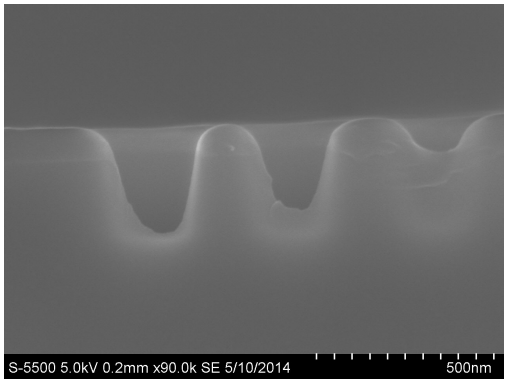

(b) Cross section of a hole with a specified diameter of 270nm.

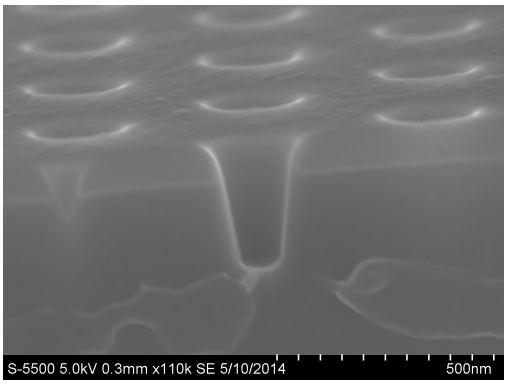

(c) Angled view of a hole with a specified diameter of 140nm.

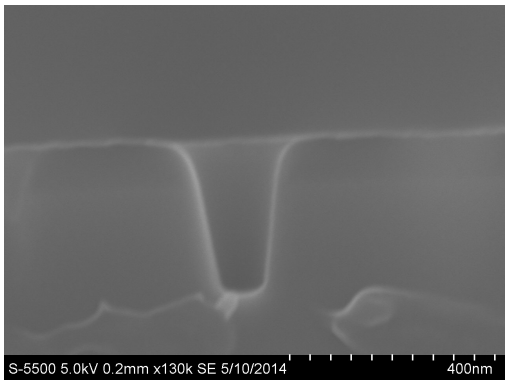

(d) Cross section of a hole with a specified diameter of 140nm.

Figure 5.21: S(T)EM pictures of shallow holes milled in silicon oxide covered silicon.

In figures 5.23 and 5.24 the milling of shallow and deep holes in silicon with a titanium dioxide thin film can be seen. The sample in figure 5.23 has some dirt on the surface due to poor sample handling. Still, it is clear that the sidewalls are smooth as in the previously discussed samples. Likewise, there is some unevenness on the hole bottoms. Some swelling around the hole edges is observed, likely as a result of the swelling observed in silicon.

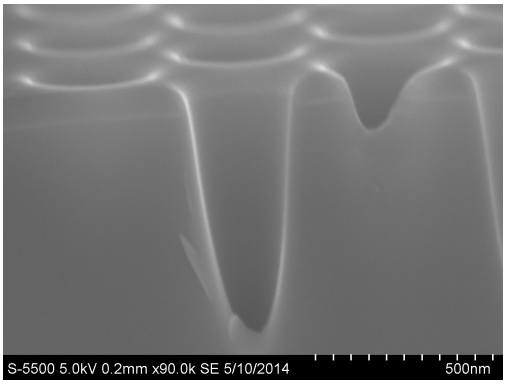

(a) Angled view of a deep hole with a specified diameter of 270nm.

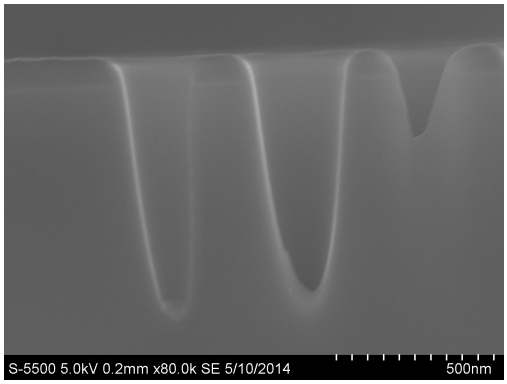

(b) Cross section of a deep hole with a specified diameter of 270nm.

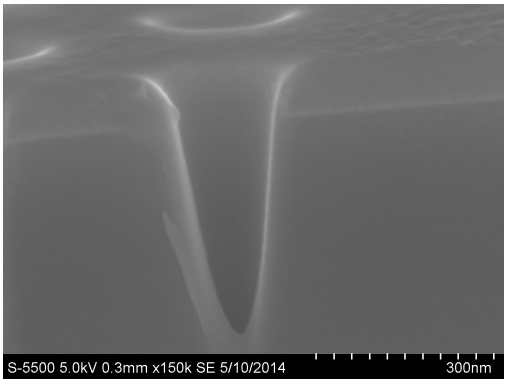

(c) Angled view of a deep hole with a specified diameter of 140nm.

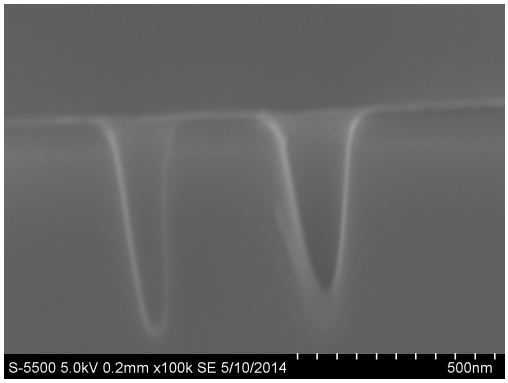

(d) Cross section of a deep hole with a specified diameter of 140nm.

Figure 5.22: S(T)EM pictures of deep holes milled in silicon oxide covered silicon.

Titanium dioxide is a crystalline material that amorphizes when exposed to milling with gallium ions. The density of crystalline titanium dioxide is higher than for amorphous titanium dioxide and explains the observed swelling [119].

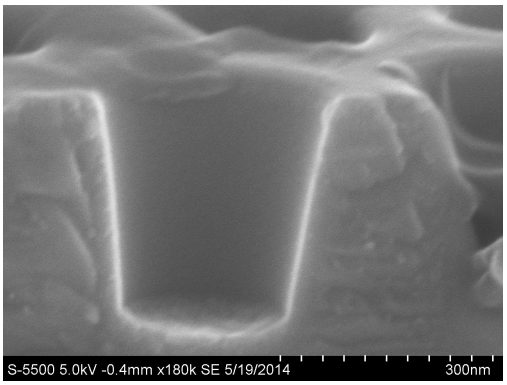

(a) Angled view of a hole with a specified diameter of 270nm.

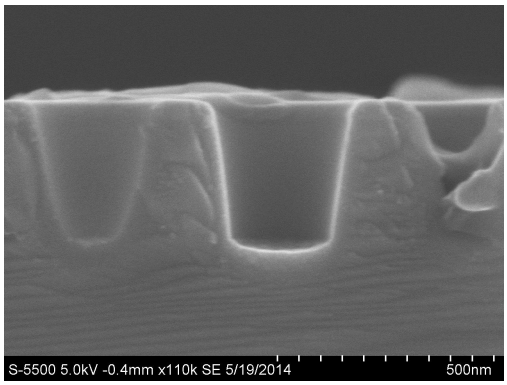

(b) Cross section of a hole with a specified diameter of 270nm.

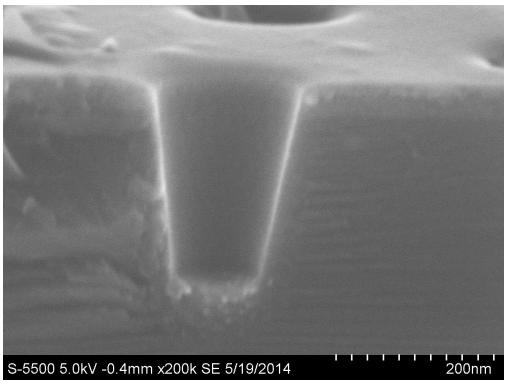

(c) Angled view of a hole with a specified diameter of 140nm.

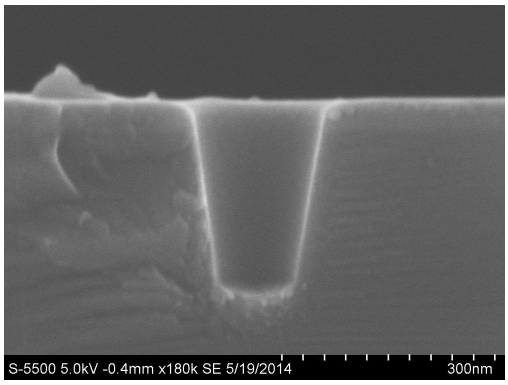

(d) Cross section of a hole with a specified diameter of 140nm.

Figure 5.23: S(T)EM pictures of shallow holes milled in titanium dioxide covered silicon.

To find the hole diameter, the cross sections were inspected with the FIB. The results for the uncovered silicon sample are shown in figure 5.25. The black areas inside the holes are owed to cavities in the deposited platinum and not redeposition as evident from the S(T)EM pictures of the cross sections. The holes are larger than specified at the top of the holes and smaller at the bottom. The correct diameter is achieved somewhere in the middle of the holes. Burr et al. [120] found that conical holes still retained the photonic band in a lithium niobate photonic crystal provided that the holes were deep enough. They also found that the wave was scattered downwards towards the substrate as discussed earlier. The scattering will be less of an issue on a SOI photonic crystal as the refractive index difference is larger

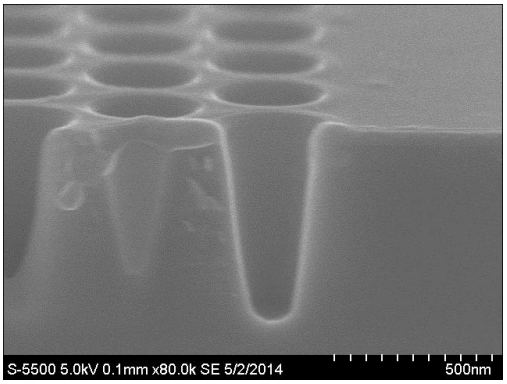

(a) Angled view of a deep hole with a specified diameter of 270nm.

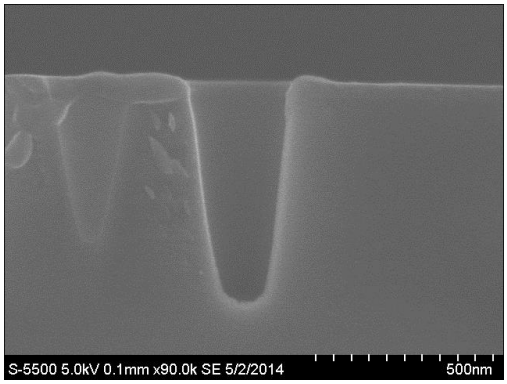

(b) Cross section of a deep hole with a specified diameter of 270nm.

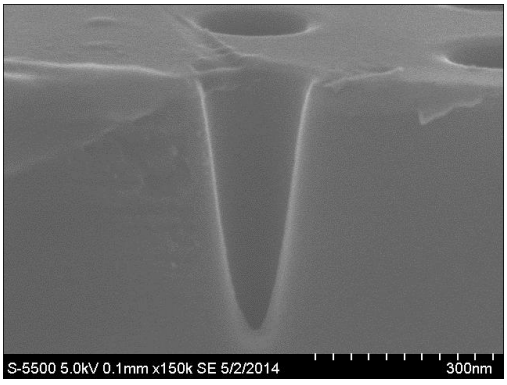

(c) Angled view of a deep hole with a specified diameter of 140nm.

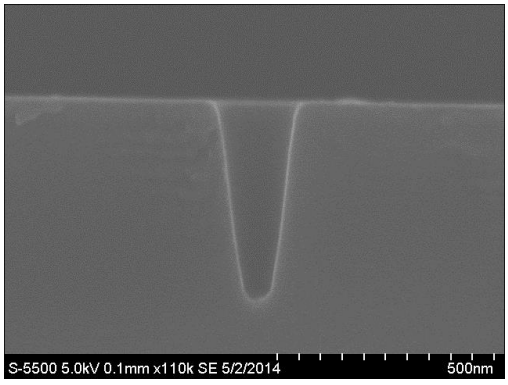

(d) Cross section of a deep hole with a specified diameter of 140nm.

Figure 5.24: S(T)EM pictures of deep holes milled in titanium dioxide covered silicon.

than in a lithium niobate photonic crystal. The same trend with regards to diameter is found for the samples with SiO_2 and TiO_2 thin films in figures 5.26 and 5.27, respectively.

5.2.5 Silicon oxide hard mask

Fabricating photonic structures using hard masks can give better results than using a PMMA resist, both with regards to roughness, feature aspect ratio and sidewall verticality [121]. One issue with etching features with a hard mask is the number of steps needed. The hard mask needs to be deposited, spin coated, patterned using EBL, then first the hard mask must be etched using one chemistry, and afterwards the substrate using a different chemistry. By patterning the thin film mask layer using FIB the process time and number of steps can be greatly reduced.

A sample was covered with 100nm of SiO_2 with the goal of fabricating a hard mask using the FIB. Holes were milled with a dose of 266.66pC/μm^2 with the intent of milling through the covering layer and leaving the silicon untouched. In figure 5.28 a structure of holes 270nm in diameter is shown. From the cross section it appears as the milling has exposed the silicon.

The structure was etched using the recipe in section 4.4. It was found in [33] that this recipe had a silicon etch rate of between 800 and 900nm/min. As the selectivity should be 10 for this etch [93], the recipe was run for 1 minute. This completely etched away the silicon oxide layer as seen in figure 5.29, resulting in destruction of the structure. This is due to aspect ratio dependent etching (ARDE). The etching rate decreases in trenches due to loss of ion flux in the trench and depletion of etching radicals and accumulation of reaction products due to lower gas flow in the etched feature [122]. The top of the structure is therefore etched faster than the holes which results in the structure seen in the figure.

A new sample was prepared and patterned with the FIB. This sample was etched for 20 seconds. The plasma ignited after 2 seconds and was slightly unstable during the etching with the CCP power varying between 39 W and 42 W and the ICP power varying between 601 W and 603 W. The thickness of the SiO_2 mask was measured before to be 97.90nm (GoF = 0.9999) before etching and after to be 63.29nm (GoF = 0.9997). This gives and SiO_2 etch rate of 1.92nm/s. The depth of the etch cannot be measured using the profilometer due to the size of the holes. The tip is larger than the hole and would not show the correct depth. The sample was broken using the scriber and investigated using the S(T)EM, shown in figure 5.30. The etch is very shallow, assumably because the FIB had not milled all the way through the SiO_2.

Therefore a sample with holes milled with a dose of 399.99pC/μm^2 was fabricated and etched as previously in this section. The thin film was 96.08nm (GoF = 0.9997) thick before etching and 59.46nm (GoF = 0.9995) thick after etching which yields an etch rate of 2.03nm/s. This time the holes were studied using the FIB system and the cross sections can be seen in figure 5.31. The holes have a depth of approximately 200nm, which is deeper than

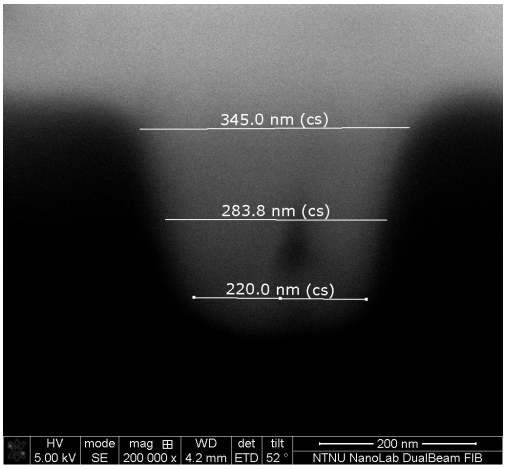

(a) Hole with a specified diameter of 270nm milled with a dose of666.65pC/μm^2.

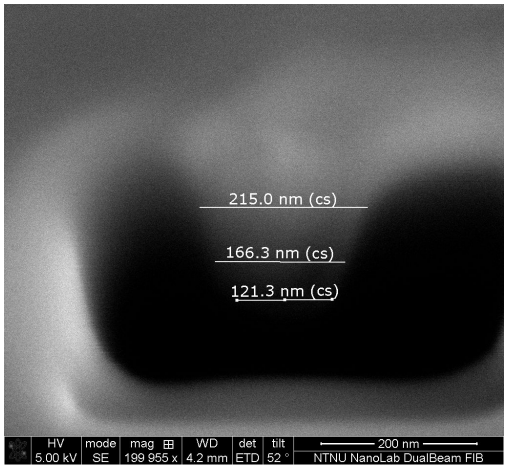

(b) Hole with a specified diameter of 140nm milled with a dose of666.65pC/μm^2

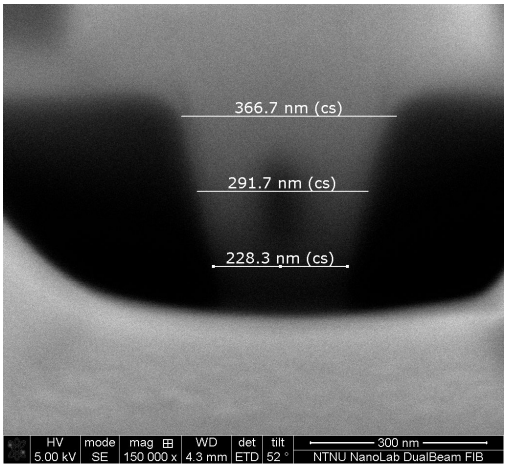

(c) Hole with a specified diameter of 270nm milled with a dose of 1.33nC/μm^2.

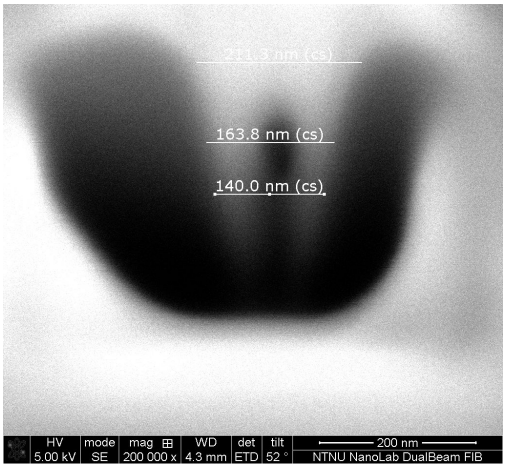

(d) Hole with a specified diameter of 140nm milled with a dose of 1.33nC/μm^2.

Figure 5.25: Cross sections of holes milled in uncovered silicon.

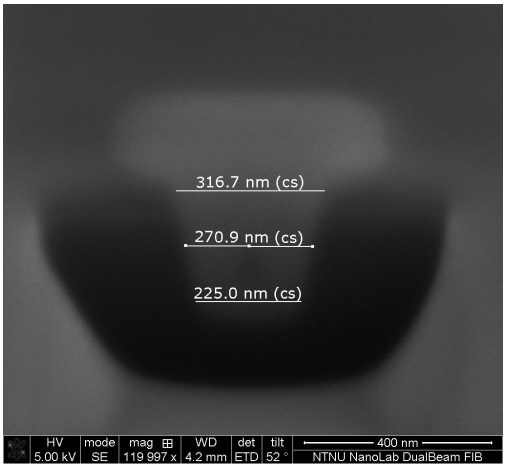

(a) Hole with a specified diameter of 270nm milled with a dose of666.65pC/μm^2.

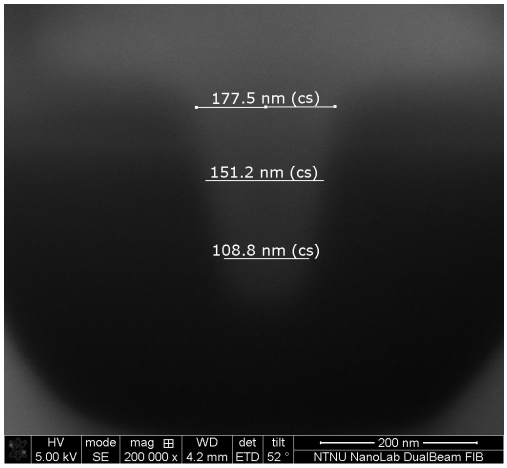

(b) Hole with a specified diameter of 140nm milled with a dose of666.65pC/μm^2

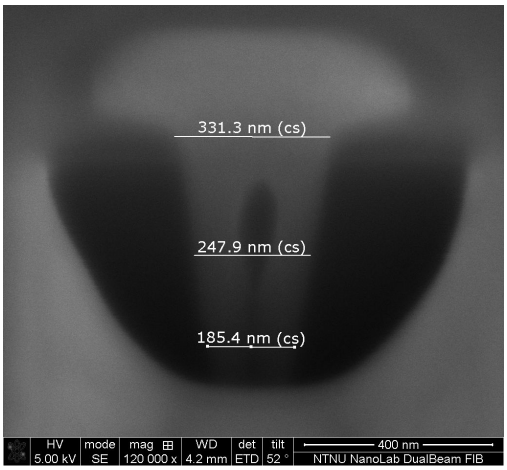

(c) Hole with a specified diameter of 270nm milled with a dose of 1.33nC/μm^2.

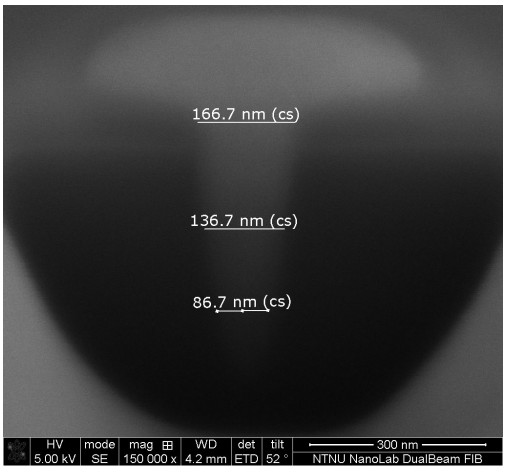

(d) Hole with a specified diameter of 140nm milled with a dose of 1.33nC/μm^2.

Figure 5.26: Cross sections of holes milled in silicon covered with a 100nm layer of silicon dioxide.

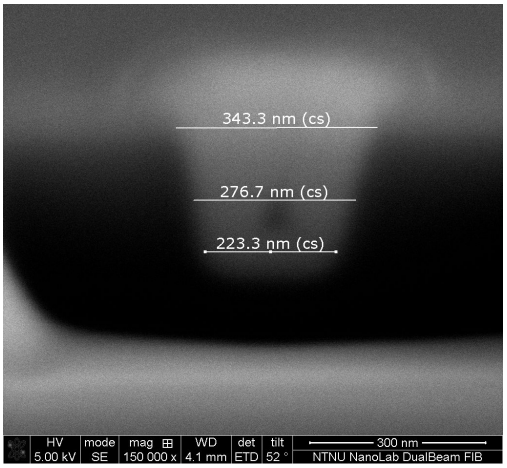

(a) Hole with a specified diameter of 270nm milled with a dose of666.65pC/μm^2.

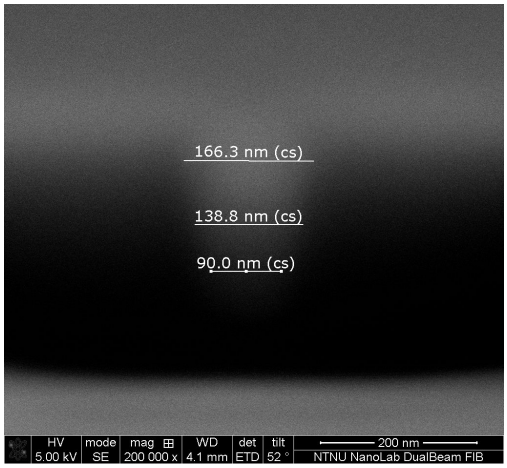

(b) Hole with a specified diameter of 140nm milled with a dose of666.65pC/μm^2

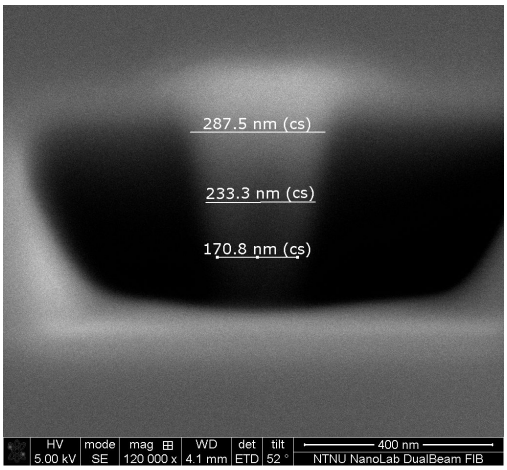

(c) Hole with a specified diameter of 270nm milled with a dose of 1.33nC/μm^2.

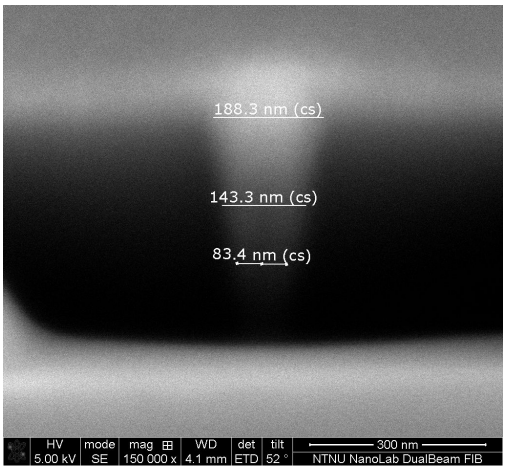

(d) Hole with a specified diameter of 140nm milled with a dose of 1.33nC/μm^2.

Figure 5.27: Cross sections of holes milled in silicon covered with a 40nm layer of titanium dioxide.

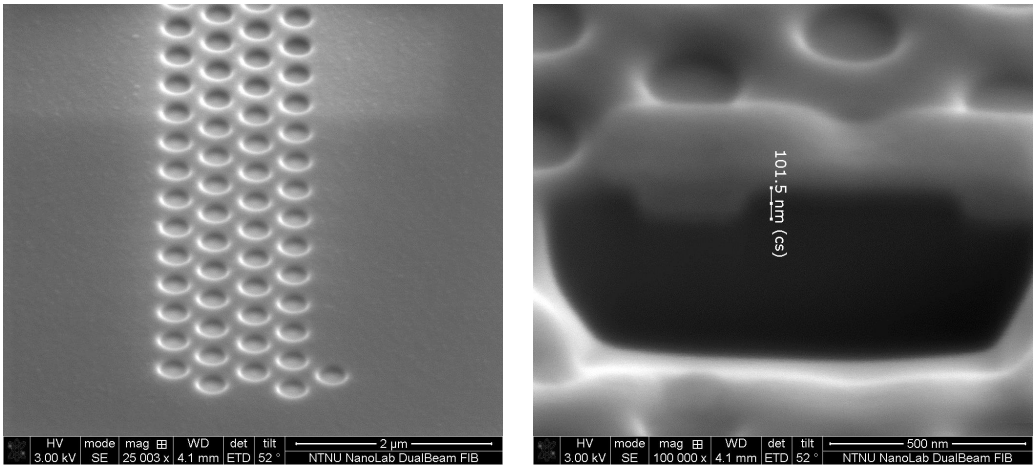

(a) Overview. (b) Cross section.

Figure 5.28: SEM pictures of holes milled in a silicon oxide covered silicon sample duing a dose of 266.66pC/µm^2.

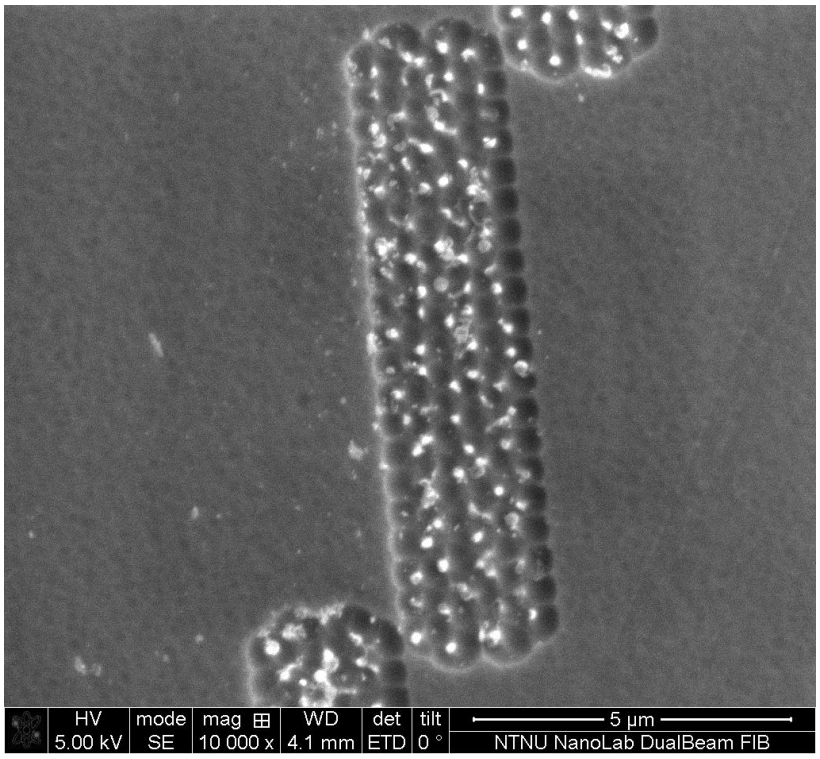

Figure 5.29: A sample etched for 60 seconds.

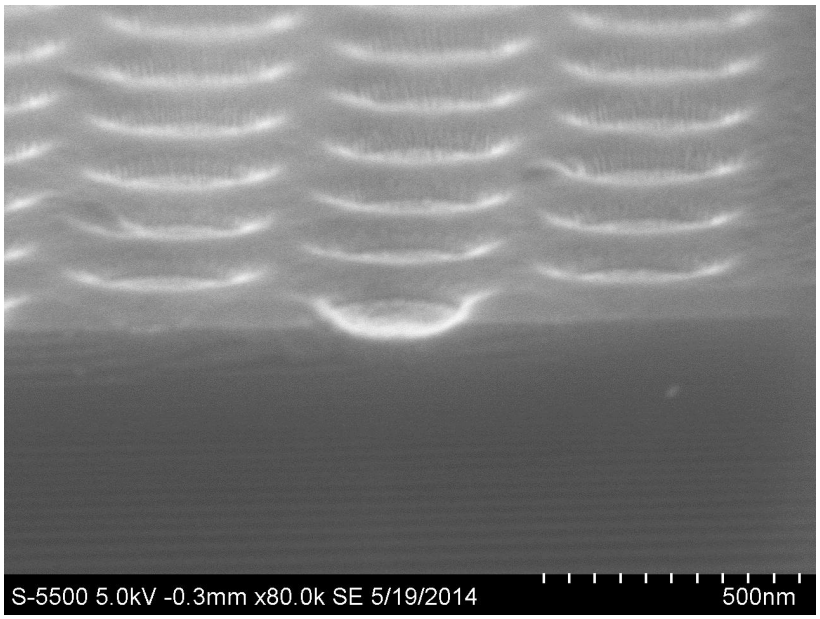

Figure 5.30: Cross section of hard mask sample etched for 20 seconds.

the holes in the mask before etching, but not as much as expected. In section 5.3 a silicon etch rate of approximately 13nm/s will be found, albeit for larger features. Still, the etch rate seen here is much lower than would be expected. It is apparent that the etch process needs refinement before being used with a silicon oxide hard mask. An alternative could be to use an Al_2O_3 thin film as a hard mask, which can yield high selectivity with silicon and does not significantly absorb light at 1.55µm [56]. Thus, the fabrication of a silicon oxide hard mask using FIB was not pursued further.

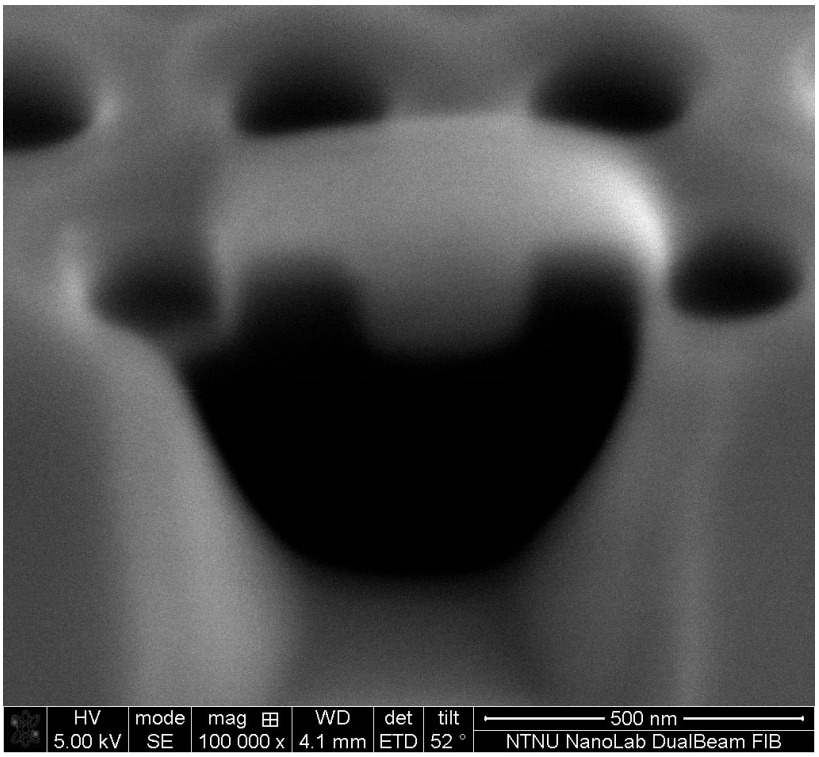

Figure 5.31: Cross section of the second hard mask sample etched for 20 seconds.

5.3 Fabrication using electron beam lithography

5.3.1 Waveguide dose optimalization

A silicon sample was prepared for EBL using the procedure defined in section 4.2 with a resist blend of 50% PMMA A9 and 50% anisol. It was exposed with the pattern shown in figure 5.32. 700nm wide and 500µm long waveguides were defined at different exposure dose factors, from 1.0 to 1.9 at 0.1 intervals. Three waveguides were exposed for each dose factor with a current of 39.9pA. After exposure and development the samples were etched using the recipe from section 4.4 for 20 seconds. The plasma ignited after about two seconds. During etching the plasma was slightly unstable with the CCP power and ICP power varying between 39W-42W and 601W-603W, respectively. This makes the process harder to reproduce later. Before etching the resist layer was measured with the reflectometer to be 307.1nm (GoF = 0.9918) thick. This is thicker than reported by Vigen [33] who measured thicknesses in the range of 250nm to 275nm. After etching the resist was measured to be 184.5nm (GoF = 0.9959). This gives a PMMA etching rate of 6.81nm/s assuming that the etching only occured during the 18 seconds the plasma was ignited. The resist was removed with an acetone bath and the etch depth measured with the profilometer (figure 5.33). All the waveguides with dose factors above 1.1 have an approximately equal etch depth of 236nm. This gives an etch rate of 13.1nm/s and a selectivity of 1.92. The found rates match the expected results from Vigen [33].

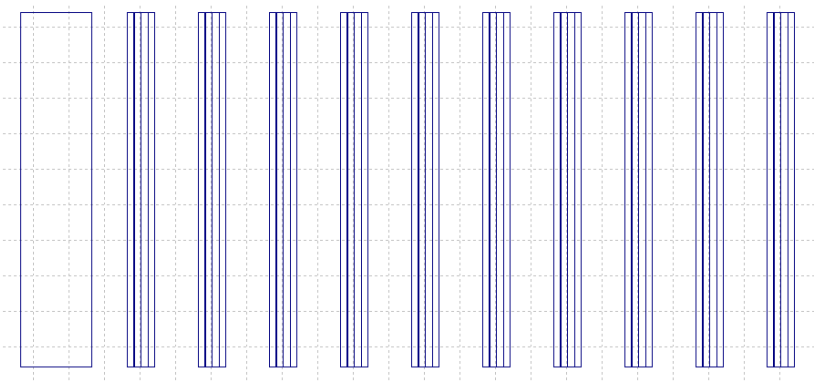

Figure 5.32: The EBL mask used for the waveguide dose optimalization. The first rectangle is a rectangle with exposure dose factor of 1.0, used for identification after etching. Each following sections defines three waveguides. The first section with dose factor 1.0, then increasing by 0.1 for each new section with the last one having a dose factor of 1.9.

The resulting waveguides turned out quite poor, with a very large degree of sidewall roughness. A S(T)EM picture of the best waveguide can be seen in figure 5.34. A subsequent attempt at exposure and etch achieved the same results. It is apparent from the figure that

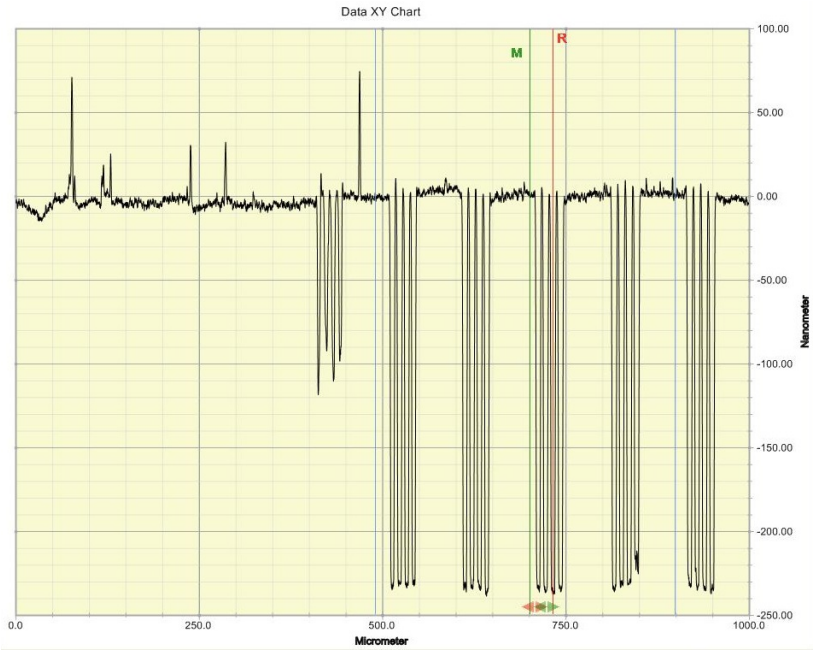

Figure 5.33: The profilometer data from the etched waveguides. From the left the height data from the waveguides exposed with a dose factor of 1.1, 1.2, 1.3, 1.4, 1.5 and 1.6 can be seen.

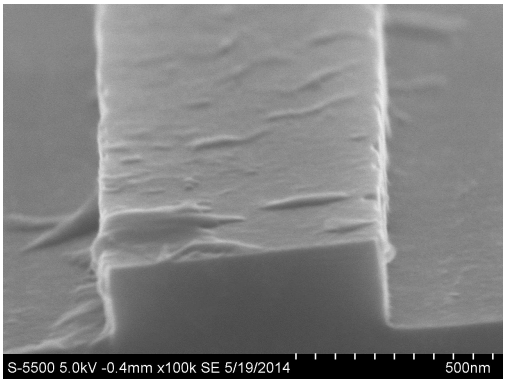

(a) Angled view.

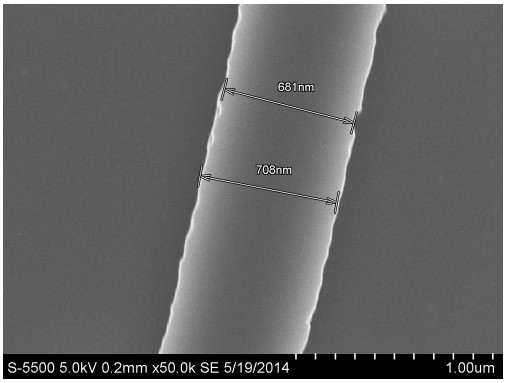

(b) Top view.

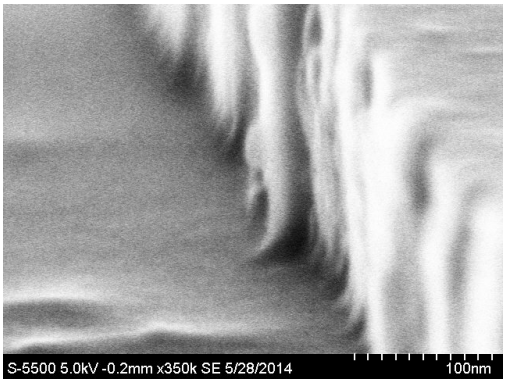

(c) Sidewall

Figure 5.34: S(T)EM pictures of the waveguides exposed with a dose factor of 1.5.

the cross section of the waveguide is close to perfect, but that the waveguide width varies greatly. The roughness being confined to the plane of the substrate points to the lithography process being the leading cause of the roughness. An unsuitable ICP-RIE process mainly causes rounded sidewalls and rough trench bottoms [93, 123]. Rather the observed roughness is likely caused by either the resist or the EBL instrument [124]. It was suspected the culprit was the resist blend as it had been blended about half a year previously. The increased thickness of the resist compared to the reported thickness in Vigen [33] leads to the same conclusion. Therefore a newly blended resist of 44% PMMA A9 and 56% anisol was used and the exposure performed again on a new sample.

The sample was etched as previously, resulting in an etch time of 18 seconds. The measured resist thickness before etching was 237.9nm (GoF = 0.9945) and after 105.5nm (GoF = 0.9959). Etch depth was found to be 258.42nm, yielding a PMMA etch rate of 7.36nm/s, a silicon etch rate of 14.35nm/s, and a selectivity of 1.95. With regards to selectivity, the new resist proved a good substitute, with approximately equal selectivities.

S(T)EM pictures of the waveguides can be seen in figures 5.35, 5.36, and 5.37. Only two cross sections are shown because the waveguides with dose factors ranging from 1.1 to 1.9 had profiles similar to the one shown in figure 5.37b. The cross sections for waveguides are similar in shape for dose factors above 1.0, with vertical sidewalls, sharp transitions between waveguide tops and sidewalls and slightly rounded at the bottom of the side walls.

There is no apparent relation between the exposure dose and degree of roughness. There is clearly less roughness than with the previous resist, typically around 10nm. The roughness is greatest for the highest dose factor, likely due to overexposure. The cross section in figure 5.37a is correspondingly very rough due to underexposure. The resist has not been exposed enough to dissolve completely in the developer, thus creating a rough bottom after etching. A relation between the width of the waveguide and the exposure dose is seen. A higher dose leads to a greater proximity effect and thus a greater area gets exposed. Figure 5.35c shows a waveguide exposed at a dose factor of 1.5, which has the width closest to 700nm.

As the waveguide with a dose factor of 1.2 gave the closest to the correct width, and the roughness and cross section being better or equal with the other etched waveguides, this is chosen as a suitable dose factor for this structure.

The results attained are poorer than reported by Vigen [33]. There has been substantial maintenance on both EBL and ICP-RIE instruments between his results and those presented here, which can be the cause of the differences. Still, no further optimization of the process was done due to time constraints and as low waveguide sidewall roughness has already been proved to be possible using the equipment at NTNU NanoLab.

5.3.2 EBL structure

The entire EBL part of the structure described in section 3.1 was fabricated on a silicon sample with the pattern shown in figure 5.38. Right after the waveguide curve, on the

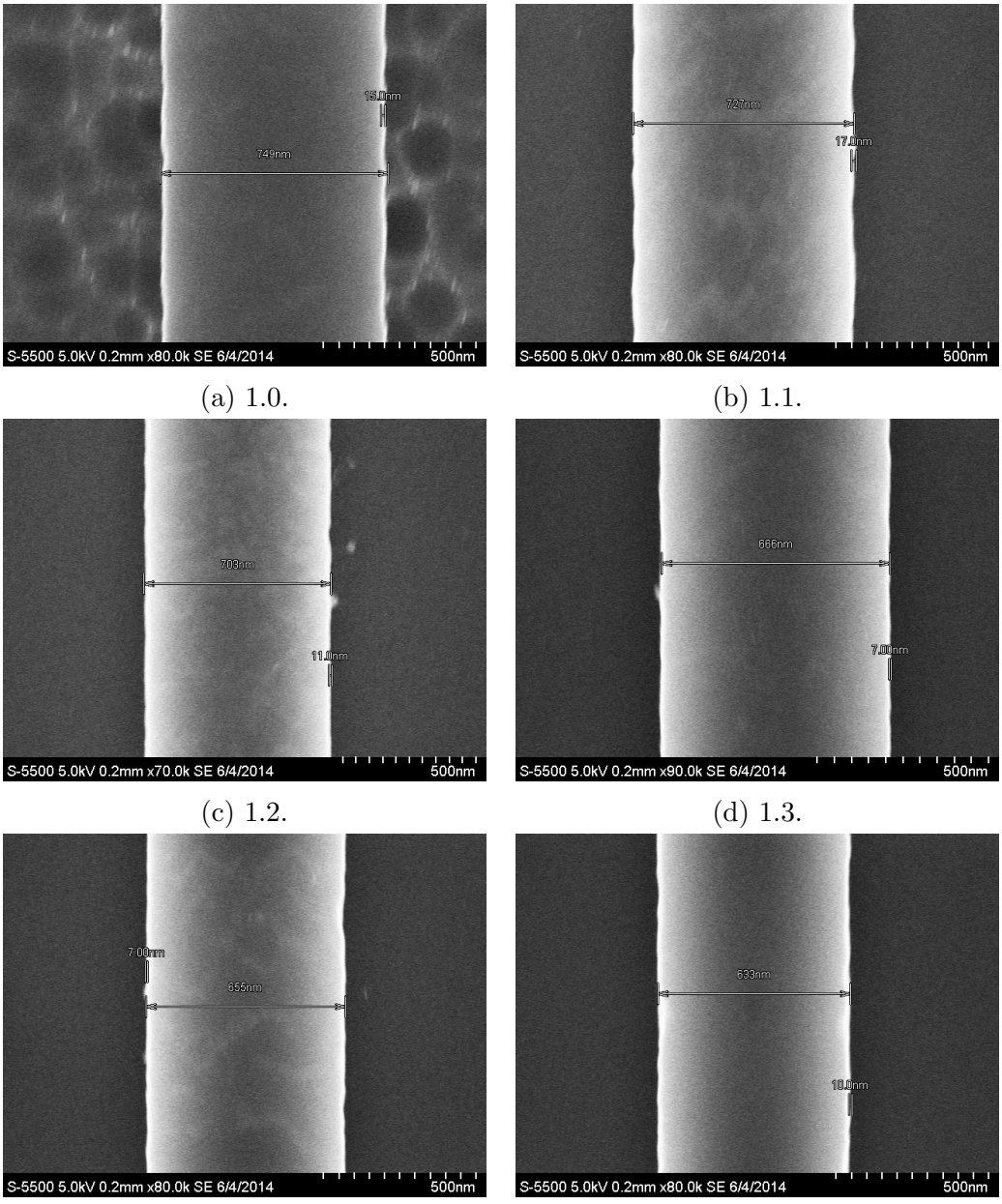

(a) 1.0. (b) 1.1.

(c) 1.2. (d) 1.3.

(e) 1.4. (f) 1.5.

Figure 5.35: Overhead view of waveguides exposed with dose factors ranging from 1.0 to 1.5.

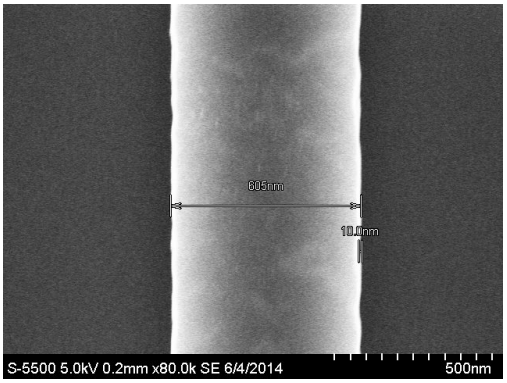

(a) 1.6.

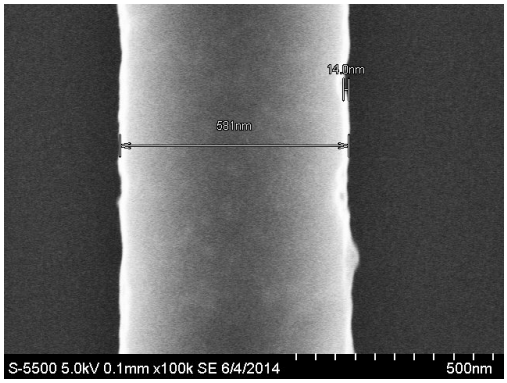

(b) 1.7.

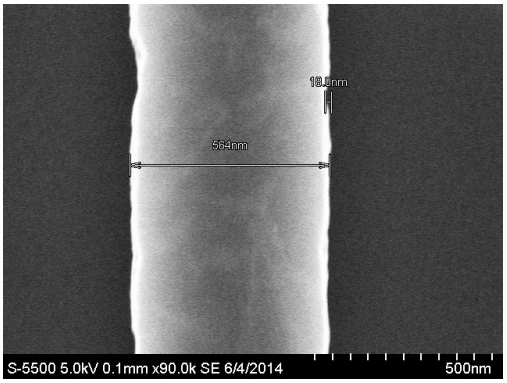

(c) 1.8.

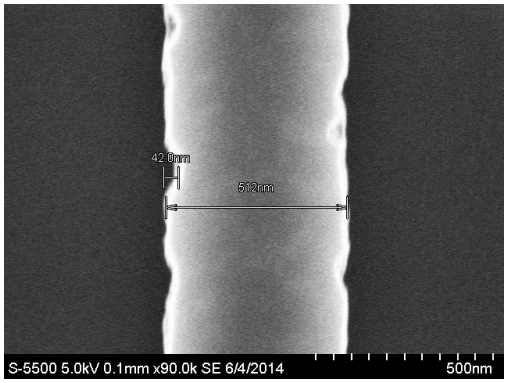

(d) 1.9.

Figure 5.36: Overhead view of waveguides exposed with dose factors ranging from 1.0 to 1.9.

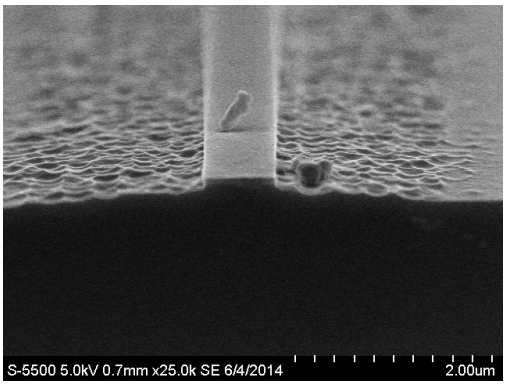

(a) 1.0.

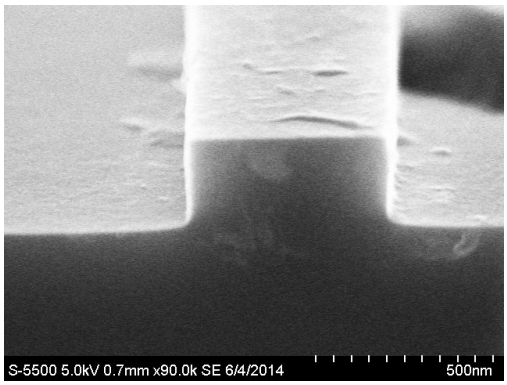

(b) 1.7.

Figure 5.37: The cross sections of waveguides exposed with dose factors of 1.0 and 1.7.

horizontal section of the waveguide a plateau, 5µm times 10µm, is defined, made to support the photonic crystal structure.

Resist was applied and measured to be 239.9nm thick (GoF = 0.9972). The exposure doses were modified with a factor 1.2 and can be seen in table 5.1. Following development, the sample was etched for 20 seconds with the same plasma behaviour as previous etch processes. Afterwards the resist thickness was measured to be 136.2nm thick (GoF = 0.9986) giving an etch rate of 5.76nm/s. Subsequently the resist was washed off with acetone and the Si etch depth measured using the profilometer (figure 5.39), and found to be 226.16nm, giving an etch rate of 12.56nm/s and a selectivity of 2.18. The differences in etch rate is assumably due to the unstable plasma. An unstable plasma comes from the plasma constantly igniting and extinguishing causing an unstable etch rate. The varying etch rate is also reported by Vigen [33], making it likely that unstable plasma was also present during that work and not a result of instrument maintenance changing the behaviour of the ICP-RIE. Further optimization of the etch recipe is needed if future work requires accurate etch depths. In the profilometer data in figure 5.39, the waveguide walls appear slanted. This is due to the shape of the profilometer needle and not a poor etch process.

Figure 5.38: The EBL mask used for the EBL structure.

The sidewall roughness and waveguide width were as expected and the results are thus not shown. The plateau with measurements is shown in figure 5.40. It is slightly larger than defined as a result of less overexposure due to the proximity effect. This will culminate in some space around the photonic crystal plateau, however, this will not eliminate the effect of the photonic crystal on the structure as similar structures have been fabricated and characterized [125, 126].

Table 5.1: The modified EBL doses.

Parameter	Value	Unit
Area dose	120	$\mu As/cm^2$
Curved area dose	120	$\mu As/cm^2$
Line dose	360	pAs/cm
Dot dose	0.12	pAs

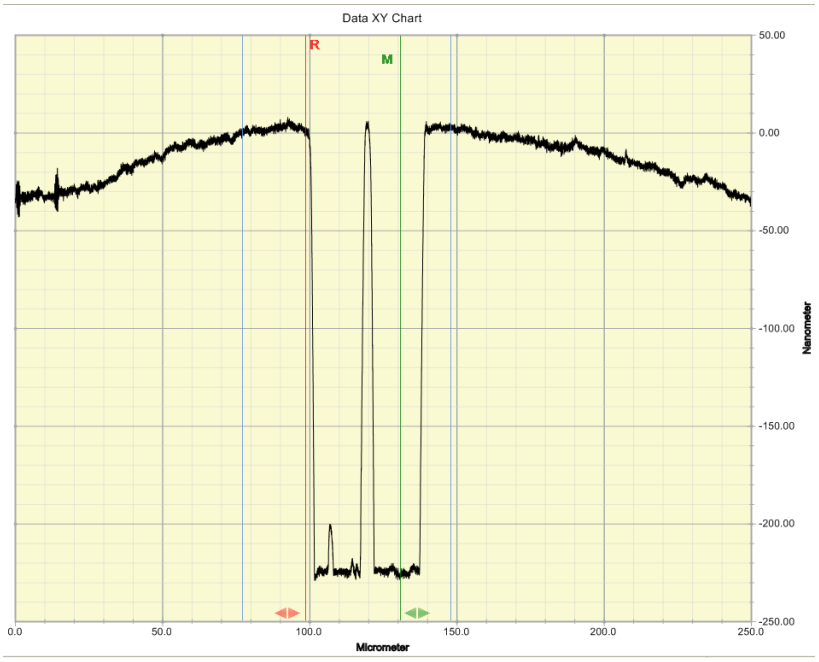

Figure 5.39: Profilometer data from waveguide.

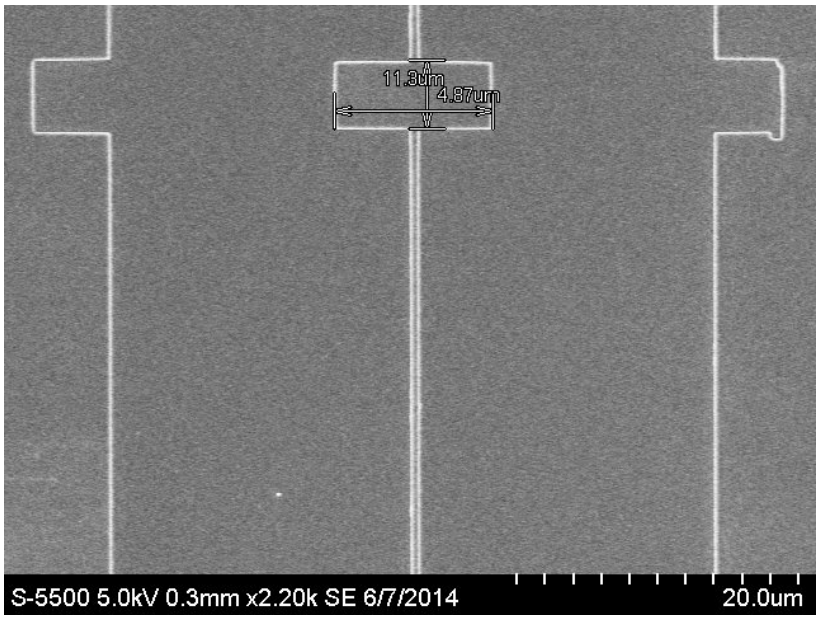

Figure 5.40: The photonic crystal plateau with measurements.

5.4 Fabrication of the final structure

Three different samples were exposed and etched using the pattern and process described in section 5.3.2. 40nm TiO_2 was deposited on one sample and 100nm SiO_2 on another. All samples were placed inside the FIB chamber and left for 10 hours to limit stage, sample, and ion beam drift while milling. Lastly the photonic crystal structures were milled using an acceleration voltage of 30kV, a current of 9pA and a dwell time of 1µs. The uncovered silicon sample was milled using a dose of 1.33nC/µm^2 and the TiO_2 and SiO_2 covered samples were milled with a dose of 666.65pC/µm^2 as those doses yielded the best sidewall angles. The results are shown in figure 5.41.

Even after waiting 10 hours, there is still substantial drift. The pictures also show that the holes are slightly asymmetrical. The simulations in section 3.3 implies that the results of this will be a splitting of the resonance peak, but that there will still be a clear bandgap. The structure will still be able to function as a sensor, but care has to be taken not to confuse the shift of the two resonances when measuring. The effect of poor write field alignment can be seen in figure 5.41d. However, it is not probable that the lines seen in the figure will affect the sensor as they are far removed from the areas with high electric field strength. The structure in figure 5.41b has an unetched area in the lower right corner. This can come from a speck of dust landing on the resist before etching. This can be avoided by better sample handling.

Compared to the photonic crystals previously fabricated at NTNU by Høvik [31] and

Lorvik [32] using EBL, the holes fabricated here are more circular and have smoother walls. However, the EBL fabricated holes have better sidewall angles and no rounding in the transition from hole to the top of the substrate.

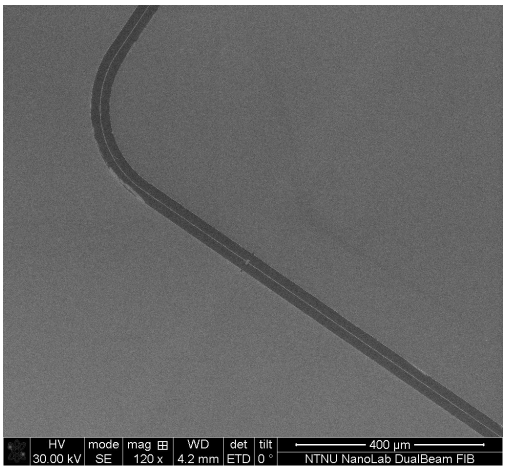

(a) Overview of uncovered silicon sensor structure.

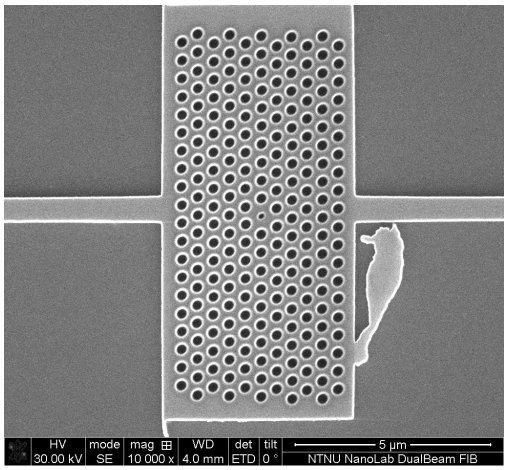

(b) The photonic crystal milled in silicon.

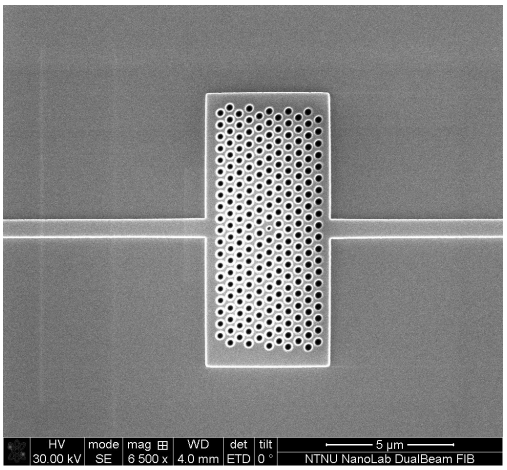

(c) The photonic crystal milled in SiO_2.

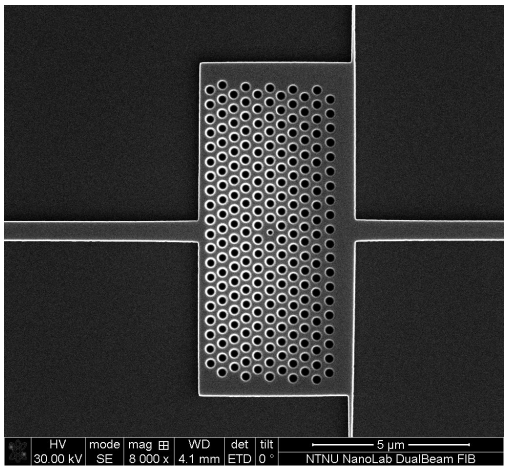

(d) The photonic crystal milled in TiO_2.

Figure 5.41: The final sensor structures.

It is likely that the final structure will suffer from high losses due to the implanted Ga ions in the photonic crystal as discussed earlier. In a FIB milled waveguide the loss is 3520 ± 90dB/cm[56]. The high field strength inside the photonic cavity implies a high photon lifetime, which results in higher losses than 4000dB/cm for the field inside the cavity. Literature suggests a number of ways to reduce the losses. Milling in the presence of I_2 reduces the losses in a waveguide to 1690 ± 90dB/cm. If this is followed by baking at 300

degrees celcius, then the losses is further reduced to 196 ± 30dB/cm[56]. High temperature annealing (1050°C) can remove the implanted ions, though Xie et al. [127] found that this caused the gallium ions to precipitate on the sample surface. Kim et al. [128] reduced the loss by annealing at 78°C in ethanol for 20 hours. [56] observed lower losses by using a protective layer, making it likely that the sensor structures with deposited thin films will suffer from less loses from the gallium implantation. In addition to the loss from the gallium ions the structure will suffer losses from the waveguide roughness and the slanted hole sidewalls.

Chapter 6

Conclusions

The aim of this work has been to investigate a photonic crystal sensor structure. Relevant photonic band gaps have been found and the sensor behaviour under non-ideal fabrication results has been analysed, both through simulations. The structure has been fabricated using a wide range of instruments, including focused ion beam milling and electron beam lithography.

Relevant theory on photonic crystals and defects was presented at the beginning of the thesis. In the follwing chapters, the sensor structure was described and possible implementation and testing issues were discussed.

6.1 Simulations

The photonic band gaps for photonic crystal slab structures, both suspended in air and on a silicon oxide substrate were found using MIT Photonic-Bands. It was concluded that two dimensional simulations are not suitable to precisely determine the band gap of a photonic slab structure. Realistic band structures were identified using three dimensional simulations. The position and size of the band gap varied depending on the refractive index of the surrounding material, the depth of the holes and the thickness of the slab, findings which were supported by theory. A silicon photonic crystal structure supported on a silicon oxide substrate yielded a larger band gap than the same structure suspended in air. Making the holes penetrate the substrate resulted in a slightly larger band gap compared to the studied structure with holes only running through the silicon layer. The slab thickness yielding the greatest gap-midgap ratio were found, with a relative thickness of 1.0 yielding the largest band gap for both structures. The gap-midgap ratios were found to be fairly constant over a range of relative thicknesses from 0.4 to 1.1, making the structure suitable for the potentially available SOI silicon top layer thicknesses. For thicker and thinner slabs the size of the gap quickly dropped off.

Using COMSOL Multiphysics, the effect of relevant fabrication errors on the resonance of the structure was simulated. Both deviating hole shapes and deviating hole positions were seen to split the resonance peak into a x-dipole resonance and a y-dipole resonance. This was supported with group theory analysis of defect modes in a hexagonal photonic crystal. The split was seen to increase with greater fabrication errors.

6.2 Focused ion beam milling

Fabrication of the photonic crystal was done using focused ion beam milling with a custom made AutoScript script. Investigations were performed both on unprocessed silicon and silicon covered with 40 nm titanium dioxide and 100 nm silicon dioxide. The thin films were intended as protective layers. The titanium dioxide films were deposited using e-beam evaporation and yielded films with thicknesses ranging from 43.21nm to 43.51nm. The PECVD deposited silicon dioxide thin films had a larger variation in thickness, ranging from 92.73nm to 101.6nm.

The effect of ion energy was studied using acceleration voltages of 5kV, 8kV, 16kV and 30kV and it was found that milling with high energy ions gave more vertical sidewalls, as well as deeper holes using the same dose compared to low energy ions. At 5kV the system was unable to focus the beam enough to fabricate the holes. Holes could be milled using higher energy ions and it was observed that the milling depth increased and the sidewall angle decreased as the ion energy increased. This and the other results were discussed and compared to results in available literature. 30kV was chosen as the optimal milling voltage, but it was also noted that this will lead to material absorption.

Optimal milling current at 30kV was found to be 9pA. Higher currents (26pA) gave poorer sidewall angles, while lower currents (1.5pA) lead to unpractically long milling times.

The effect of dwell time on the holes was studied utilizing dwell times of 1ms, 100µs, 10µs, and 1µs, both on uncovered silicon samples and silicon samples with deposited thin films. It was found that short dwell times gave the best side wall angles, but at some doses created mounds on the hole bottoms. A model based on redeposition of milled material was developed and presented. Milling deeper holes produced rounded hole bottoms. Although, as discussed, this is not and issue as the bottom will be in the oxide layer an thus not greatly affect the light propagation. Deeper holes gave for uncovered silicon better sidewall angles, a result not seen for the holes milled in the thin film covered samples. Possible reasons for this was discussed, however, no clear rationale for this was discovered. Milling in TiO_2 covered silicon yielded the best holes due to titanium dioxide having a slower etch rate than silicon and thus protects the underlying silicon from the beam tails. The best result was achieved using a dwell time of 1ms, a dose of 666.65pC/µm^2 on a titanium dioxide covered sample, giving a sidewall angle of 3.2 degrees.

By studying the hole cross sections in a scanning electron microscope it was found that the

milled holes have smooth walls, which would lead to lower scattering losses. Surface swelling in the silicon and titanium dioxide were observed, but not in the silicon dioxide. This was explained by looking at the density of crystalline and amorphous silicon and titanium dioxide. The density in the crystalline materials are higher, and thus experiences swelling when being amorphized during milling. Silicon dioxide is deposited as amorphous, and therefore does not swell during milling.

The evolution of the hole diameter was investigated using the FIB. The hole diameters decrease towards the bottom of the holes as expected with the specified hole diameter appearing near the midpoint of the holes.

Attempts at using the silicon dioxide thin film fabricated with FIB milling as a hard mask in a reactive ion etch process proved unfruitful. The silicon etch rate was shown to be very slow and the selectivity very poor for this geometry, and the process was abandoned.

6.3 Electron beam lithography

Waveguides and a plateau to support the photonic crystal structure were fabricated using electron beam lithography and reactive ion etching. Butt coupling was found to be the easiest way to facilitate a future optical characterization of the sensor, thus a 90 degree turn in the waveguide was fabricated to avoid erroneous measurements.

This work was based on work previously done at NTNU NanoLab. Two different resist blends were used, a mix 50% PMMA A9 and 50% anisol, and a mix of 46% PMMA A9 and 56% anisol. After exposure the sample was etched with a SF_6/CHF_3 reactive ion etch recipe. Dose factor tests to determine the optimal exposure dose for the needed waveguides were performed. For the first resist, the PMMA silicon etch selectivity was found to be 1.92, which was in the expected range. However, the waveguides fabricated had greater sidewall roughness than previously reported. This was attributed to the resist. A subsequent fabrication with the other resist resulted in improved results with sidewall roughness around 10nm, however not as good as expected from the previous work. The selectivity of the second resist was found for two different etches to be 1.95 and 2.18.

Optimal dose factor for the wanted waveguides was found to be 1.2. The final structure was fabricated, with the plateau for the photonic crystal being slightly larger than specified due to the that the proximity effect being weaker on the large plateau compared to the thin waveguides. Thin films were deposited on the structure and lastly the photonic crystal structure milled with FIB. The resulting structure was slightly distorted due to drift in the focused ion beam. The effect of this was discussed with help of the simulations discussed earlier.

Sensor behaviour and loss were discussed. From the observed fabrication errors it is likely that the resonance would split. Due to implanted gallium ions, high losses are expected. Potential ways to reduce these losses were reviewed.

6.4 Future work

Hopefully, this work will be useful for future work on photonics and photonic crystal structures at NTNU. Potential future work includes, but are not limited to:

- Optical characterization of the photonic structure.
- Investigation of the suggested methods of material loss minimization.
- Biofunctionalization of the surface along with measurement of the resonance shift.
- Design and fabrication of a grating coupler to simplify testing of photonic structures.
- Creation of a reliable and optimized EBL process.
- Integration with microfluidics to create a self contained "lab on a chip".

Appendix A

Acronyms

ARDE Aspect ratio dependent etching

CCP Capacitive coupled plasmas

DoF Depth of field

DoS Density of states

E-beam evaporation Electron beam physical vapor evaporation

EBL Electron beam lithography

FEM Finite element method

FIB Focused ion beam

ICP Inductively coupled plasmas

GoF Goodness of fit

MPB MIT Photonic-Bands

PEVCD Plasma enhanced chemical vapor deposition

PML Perfectly matched layer

PMMA Polymethylmethacrylate

RF Radio frequency

RIE Reactive ion etch

SE Secondary electrons

SEM Scanning electron microscope

SOI Silicon on insulator

Appendix B

Derivation of the one-dimensional dispersion relation

We will here derive the one-dimensional dispersion relation, starting from equation 2.27. This section is based on Saleh and Teich [36, ch. 7] and Dirdal [37].

$$(M_0 - e^{-ikd}I)\begin{bmatrix} u_m^+ \\ u_m^- \end{bmatrix} = 0 \tag{B.1}$$

Where M_0 was

$$M_0 = \begin{bmatrix} \frac{1}{t^*} & \frac{r}{t} \\ \frac{r^*}{t^*} & \frac{1}{t} \end{bmatrix} \tag{B.2}$$

and t and r are the transmission and reflection, respectively, going from one material to another.

If u_m^+ or u_m^- are unlike zero then $|M_0 - e^{-ikd}I| = 0$. The solution to this is

$$e^{-ikd} = Re\{\frac{1}{t}\} \pm i\sqrt{1 - \left(Re\{\frac{1}{t}\}\right)^2} \tag{B.3}$$

which can be simplified like this

$$
\begin{aligned}
2cos(kd) &= e^{-ikd} + e^{ikd} \\
&= e^{-ikd} + \frac{1}{e^{-ikd}} \\
&= Re\{\frac{1}{t}\} \pm i\sqrt{1 - \left(Re\{\frac{1}{t}\}\right)^2} + \frac{1}{Re\{\frac{1}{t}\} \pm i\sqrt{1 - \left(Re\{\frac{1}{t}\}\right)^2}} \\
&= Re\{\frac{1}{t}\} \pm i\sqrt{1 - \left(Re\{\frac{1}{t}\}\right)^2} + \frac{Re\{\frac{1}{t}\} \mp i\sqrt{1 - \left(Re\{\frac{1}{t}\}\right)^2}}{(Re\{\frac{1}{t}\})^2 - (i\sqrt{1 - \left(Re\{\frac{1}{t}\}\right)^2})^2} \\
&= Re\{\frac{1}{t}\} \pm i\sqrt{1 - \left(Re\{\frac{1}{t}\}\right)^2} + \frac{Re\{\frac{1}{t}\} \mp i\sqrt{1 - \left(Re\{\frac{1}{t}\}\right)^2}}{(Re\{\frac{1}{t}\})^2 + 1 - \left(Re\{\frac{1}{t}\}\right)^2} \\
&= Re\{\frac{1}{t}\} \pm i\sqrt{1 - \left(Re\{\frac{1}{t}\}\right)^2} + Re\{\frac{1}{t}\} \mp i\sqrt{1 - \left(Re\{\frac{1}{t}\}\right)^2}
\end{aligned}
\tag{B.4}
$$

$$
cos(kd) = Re\{\frac{1}{t}\} \tag{B.5}
$$

Now we only have to determine $Re\{1/t\}$ for our system. We start by looking at figure B.1 again. First the wave propagates through 1, then there is reflection and transmission at the barrier between material 1 and 2, propagation through 2 and then reflection and transmission at the next barrier. This gives a transfer matrix for the entire unit

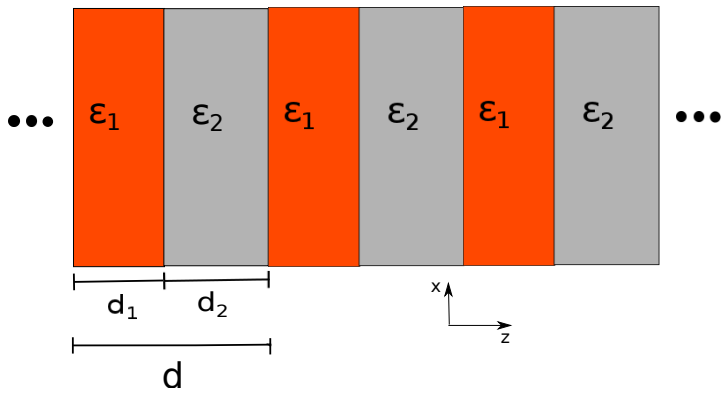

Figure B.1: The structure of a one-dimensional photonic crystal.

$$
M = M_{21} M_{prop2} M_{12} M_{prop1} \tag{B.6}
$$

From equation 2.24 we see that we need expressions for t and r. For this we use Fresnel's equations. We will only treat light with a normal incidence to the layers.

$$r_{12} = \frac{n_1 - n_2}{n_1 + n_2} \tag{B.7}$$

$$t_{12} = \frac{2n_1}{n_1 + n_2} \tag{B.8}$$

$$\begin{aligned} M_{12} = \frac{1}{t_{21}} \begin{bmatrix} t_{12}t_{21} - r_{12}r_{21} & r_{21} \\ -r_{12} & 1 \end{bmatrix} &= \frac{n_1 + n_2}{2n_1} \begin{bmatrix} \frac{2n_1}{n_1+n_2}\frac{2n_2}{n_1+n_2} - \frac{n_1-n_2}{n_1+n_2}\frac{n_2-n_1}{n_1+n_2} & \frac{n_2-n_1}{n_1+n_2} \\ -\frac{n_1-n_2}{n_1+n_2} & 1 \end{bmatrix} \\ &= \frac{1}{2n_2} \begin{bmatrix} n_1 + n_2 & n_2 - n_1 \\ n_2 - n_1 & n_1 + n_2 \end{bmatrix} \end{aligned} \tag{B.9}$$

$$M_{21} = \frac{1}{2n_1} \begin{bmatrix} n_1 + n_2 & n_1 - n_2 \\ n_1 - n_2 & n_1 + n_2 \end{bmatrix} \tag{B.10}$$

For propagation through a homogeneous medium the propagation matrix becomes

$$M_{prop} = \begin{bmatrix} e^{-i\phi} & 0 \\ 0 & e^{i\phi} \end{bmatrix} \tag{B.11}$$

Inserting these matrices in equation B.6 gives us

$$\begin{aligned} M &= \frac{1}{2n_1} \begin{bmatrix} n_1 + n_2 & n_1 - n_2 \\ n_1 - n_2 & n_1 + n_2 \end{bmatrix} \begin{bmatrix} e^{-i\phi_2} & 0 \\ 0 & e^{i\phi_2} \end{bmatrix} \frac{1}{2n_2} \begin{bmatrix} n_1 + n_2 & n_2 - n_1 \\ n_2 - n_1 & n_1 + n_2 \end{bmatrix} \begin{bmatrix} e^{-i\phi_1} & 0 \\ 0 & e^{i\phi_1} \end{bmatrix} \\ &= \frac{1}{4n_1n_2} \begin{bmatrix} (n_1 + n_2)e^{-i\phi_2} & (n_1 - n_2)e^{i\phi_2} \\ (n_1 - n_2)e^{-i\phi_2} & (n_1 + n_2)e^{i\phi_2} \end{bmatrix} \begin{bmatrix} (n_1 + n_2)e^{-i\phi_1} & (n_2 - n_1)e^{i\phi_1} \\ (n_2 - n_1)e^{-i\phi_1} & (n_1 + n_2)e^{i\phi_1} \end{bmatrix} \end{aligned} \tag{B.12}$$

From equation B.5 we see that the lower right element of M in equation B.12 should be equal to $1/t$. This yields

$$\begin{aligned} \frac{1}{t} &= \frac{(n_1 + n_2)^2}{4n_1n_2} e^{j(\phi_1+\phi_2)} - \frac{(n_1 - n_2)^2}{4n_1n_2} e^{j(\phi_1-\phi_2)} \\ &= \frac{(n_1 + n_2)^2}{4n_1n_2} (cos(\phi_1 + \phi_2) + isin(\phi_1 + \phi_2)) \\ &- \frac{(n_1 - n_2)^2}{4n_1n_2} (cos(\phi_1 - \phi_2) + isin(\phi_1 - \phi_2)) \end{aligned} \tag{B.13}$$

$$Re\{\frac{1}{t}\} = \frac{(n_1 + n_2)^2}{4n_1n_2} cos(\phi_1 + \phi_2) - \frac{(n_1 - n_2)^2}{4n_1n_2} cos(\phi_1 - \phi_2) \tag{B.14}$$

Using equation 2.27, $k_m/k_0 = n_m$ and $\phi_m = k_m d_m$ we get our dispersion relation

$$cos(kd) = \frac{(k_1 + k_2)^2}{4k_1k_2} cos(k_1d_1 + k_2d_2) - \frac{(k_1 - k_2)^2}{4k_1k_2} cos(k_1d_1 - k_2d_2) \tag{B.15}$$

This equation can be further simplified.

$$\begin{aligned}
cos(kd) &= \frac{(k_1 + k_2)^2}{4k_1k_2}[cos(k_1d_1)cos(k_2d_2) - sin(k_1d_1)sin(k_2d_2)] \\
&- \frac{(k_1 - k_2)^2}{4k_1k_2}[cos(k_1d_1)cos(k_2d_2) + sin(k_1d_1)sin(k_2d_2)] \\
&= \frac{k_1^2 + 2k_1k_2 + k_2^2 - k_1^2 + 2k_1k_2 - k_2^2}{4k_1k_2} cos(k_1d_1)cos(k_2d_2) \\
&- \frac{k_1^2 + 2k_1k_2 + k_2^2 + k_1^2 - 2k_1k_2 + k_2^2}{4k_1k_2} sin(k_1d_1)sin(k_2d_2) \\
&= cos(k_1d_1)cos(k_2d_2) - \frac{k_1^2 + k_2^2}{2k_1k_2} sin(k_1d_1)sin(k_2d_2) \\
&= cos(k_1d_1 + k_2d_2) + sin(k_1d_1)sin(k_2d_2) - \frac{k_1^2 + k_2^2}{2k_1k_2} sin(k_1d_1)sin(k_2d_2) \\
&= cos(k_1d_1 + k_2d_2) - \frac{k_1^2 - 2k_1k_2 + k_2^2}{2k_1k_2} sin(k_1d_1)sin(k_2d_2)
\end{aligned} \tag{B.16}$$

Finally we find the dispersion relation shown in equation 2.28.

$$cos(kd) = cos(k_1d_1 + k_2d_2) - \frac{(k_1 - k_2)^2}{2k_1k_2} sin(k_1d_1)sin(k_2d_2) \tag{B.17}$$

Appendix C

Derivation of temporal coupled-mode equation

This is a derivation of equation 2.46 used in section 2.6.1 and will follow the derivation in Joannopolous et al. [35, ch. 10]. We start by looking again at figure C.1 where we have a cavity with a field proportional to A, decay times of τ_1 and τ_2 into the two single mode waveguides of τ_1 and τ_2, amplitudes of fields moving towards the cavity (S_{1+}, S_{2+}) and away (S_{1-}, S_{2-}) from it.

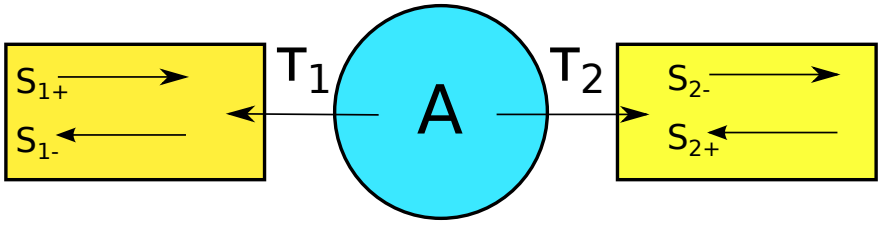

Figure C.1: A schematic figure of a system with an input waveguide with S_{1+} as the incoming field and S_{1-} as the outgoing field, a photonic crystal with a cavity with a field proportional with A and decay time into the two waveguides of τ_1 and τ_2, and an output waveguide with S_{2+} as the incoming field and S_{2-} as the outgoing field.

The assumptions made are weak coupling from the cavity, conservation of energy, linearity, time-invariance and time-reversal invariance. The most imporant being weak coupling. The field in the cavity is proportional to a variable A. We choose that $|A|^2$ is the electromagnetic energy stored in the cavity. For the fields in the waveguides $S_{i\pm}$ we chose that $|S_{i\pm}|^2$ is the incoming or outgoing power. The coupling is weak so one can assume that the field decays with a lifetime τ. We have two ways of coupling out and this gives us $1/\tau = 1/\tau_1 + 1/\tau_2$. Because the coupling is weak, the amplitude in the cavity will satisfy this differential equation $\mathrm{d}A/\mathrm{d}t = -i\omega_0 A - A/\tau$ [129, ch. 7.1], for which the solution is $A(t) = A(0)e^{-i\omega_0 t}e^{-t/\tau}$.

Now we also take the waveguides into consideration. The waves will either couple in to the cavity or be reflected, and the cavity will couple out to the waveguides.

$$\mathrm{d}A/\mathrm{d}t = -i\omega_0 A - A/\tau_1 - A/\tau_2 + \alpha_1 S_{1+} + \alpha_2 S_{2+} \tag{C.1}$$

$$S_{l-} = \beta_l S_{l+} + \gamma_l A \tag{C.2}$$

where β_l is the reflection coefficient and α_l and γ_l is the degree of coupling between the cavity and the waveguides. In these equations we have assumed linearity, time-invariance and weak coupling. Weak coupling implies that $\mathrm{d}A/\mathrm{d}t$ depends on $S_{l\pm}$ multiplied with a constant. This is because at weak coupling only the frequencies around the resonant frequency contributes.

First we want to find an expression for γ_l. If the second waveguide is totally decoupled from the cavity then $\tau_2 \to \infty$. Also, if there are no incoming waves, $S_{l+} = 0$, the expression for the field in the cavity becomes $A(t) = A(0)e^{-i\omega_0 t}e^{-t/\tau_1}$. In the waveguides only S_{1-} will be different from zero as this is the only place the energy in the cavity is allowed to decay.

$$\begin{gathered} -\mathrm{d}|A|^2/\mathrm{d}t = \frac{2}{\tau_1}|A|^2 = |S_{1-}|^2 = |\gamma_1|^2|A|^2 \\ \gamma_1 = \sqrt{\frac{2}{\tau_1}} \end{gathered} \tag{C.3}$$

We can treat the other waveguide in the same manner resulting in $\gamma_2 = \sqrt{\frac{2}{\tau_2}}$. The sign of γ_l is arbitrarily chosen since it only represents the phase of the wave.

Time-reversal symmetry tells us that if we perform this sequence backwards in time and conjugate, we will obtain another solution to equation C.1. From a decaying field in the cavity and no incoming wave we obtained $S_{l-} = \sqrt{2/\tau_l}A$. Thus $A(t) = A(0)e^{-i\omega_0 t}e^{t/\tau_1}$ with $S_{1-} = 0$ and $S_{1+} = \sqrt{2/\tau_l}A$. This immediately shows that $\alpha_l = \sqrt{\frac{2}{\tau_l}}$. Inserting this into C.2 we get that $\beta_l = -1$. Thus if $\tau_l \to \infty$, $S_{l-} = -S_{l+}$, i.e. everything is reflected as expected. The sign comes from the chosen sign of γ_l. By inserting this back into C.1 we obtain

$$\mathrm{d}A/\mathrm{d}t = -i\omega_0 A - A/\tau_1 - A/\tau_2 + \sqrt{2/\tau_1}S_{1+} + \sqrt{2/\tau_2}S_{2+} \tag{C.4}$$

$$S_{l-} = -S_{l+} + \sqrt{2/\tau_l}A \tag{C.5}$$

In a sensor we assume that there will only be an incoming field from one side, $S_{2+} = 0$. The input from S_{1+} is oscillating at a fixed frequency ω and because we have assumed linearity the field everywhere must oscillate at this frequency and $\mathrm{d}A/\mathrm{d}t = -i\omega A$.

$$-i\omega A = -i\omega_0 A - A/\tau_1 - A/\tau_2 + \sqrt{2/\tau_1}S_{1+} \tag{C.6}$$

$$S_{1-} = -S_{1+} + \sqrt{2/\tau_1}A \tag{C.7}$$

$$S_{2-} = \sqrt{2/\tau_2}A \tag{C.8}$$

In a perfect photonic crystal the transmission in the band gap is zero. It is therefore interesting to look at how the defect affects this. The definition of the transmission is $T(\omega) = |S_{2-}|^2/|S_{1+}|^2$. First we begin with solving equation C.6 for S_{1+}

$$\begin{aligned} A\left[-i(\omega-\omega_0) + \frac{1}{\tau_1} + \frac{1}{\tau_2}\right] &= \sqrt{\frac{2}{\tau_1}}S_{1+} \\ \frac{1}{|S_{1+}|^2} &= \frac{\frac{2}{\tau_1}}{(\omega_0-\omega)^2 + \left(\frac{1}{\tau_1}+\frac{1}{\tau_2}\right)^2}|A|^2 \end{aligned} \tag{C.9}$$

and divide the expression for $|S_{2-}|^2$ by this

$$T(\omega) = \frac{|S_{2-}|^2}{|S_{1+}|^2} = \frac{\frac{4}{\tau_1\tau_2}}{(\omega_0-\omega)^2 + \left(\frac{1}{\tau_1}+\frac{1}{\tau_2}\right)^2} \tag{C.10}$$

which is the equation we used in section 2.6.1.

Appendix D

MIT Photonic-Bands

MIT Photonic-Bands is a free software developed at MIT for computing the band structures and electromagnetic modes of periodic dielectric structures. It was developed by Steven G. Johnson at MIT along with the Joannopoulos Ab Initio Physics group [130].

Here, only the code used to find the band gap of a two dimensional asymmetric photonic crystal slab will be presented. A detailed introduction to MPB along with code used to plot the band structure is presented in the project thesis [34].

```
(define-param h 0.5)
(define-param eps 12)
(define-param loweps 2.1448)
(define-param r 0.25)
(define-param supercell-h 4)

(set! geometry-lattice (make lattice (size 1 1 supercell-h)
                (basis1 (/ (sqrt 3) 2) 0.5)
                (basis2 (/ (sqrt 3) 2) -0.5)))

(set! geometry
     (list (make block (material (make dielectric (epsilon loweps))
         )
          (center 0 0 (* 0.25 supercell-h))
          (size infinity infinity (* 0.5 supercell-h)))
           (make block (material (make dielectric (epsilon eps)))
          (center 0) (size infinity infinity h))
           (make cylinder (material air)
          (center 0) (radius r) (height h))))

(define Gamma (vector3 0 0 0))
```

```
(define M (vector3 0 0.5 0))
(define K (vector3 (/ -3) (/ 3) 0))

(define-param only-K false)
(define-param k-interp 32)
(if only-K
     (set! k-points (list K))
     (set! k-points (interpolate k-interp (list Gamma M K Gamma))))

(set-param! resolution (vector3 32 32 16))
(set-param! num-bands 5)

(run-zeven)
(run-zodd)

(display-eigensolver-stats)
```

Appendix E

COMSOL Multiphysics

COMSOL Multiphysics 4.4 is a computer program designed to analyse various physical phenomena. To investigate problems involving electromagnetic waves the RF module have been used. COMSOL uses the finite element method (FEM) [131]. FEM finds approximations to the solutions to partial differential equations. It takes the strong formulation of the problem and converts it in to a weak formulation with the help of a test function and transformation of integrals. This is made in to a discrete problem using Galerkin projection, which means dividing the area in to a finite number of elements. This makes it possible to transform the original problem into one that can be solved numerically [132]. A thorough introduction can be found in the project thesis [34]. Here, only the differences from the setup described will be presented.

To generate the structure the following script was used. COMSOL with Matlab is needed to run the script. The script generates a geometry file which can be imported in COMSOL under the geometry tab. The light propagation is then simulated in the same fashion as in the project thesis.

```
tic
close all;

% Parameters
a = 465e-9; %lattice const
r = 135e-9; %hole radius
defectr = 70e-9; %defect rad
ysize = 21;
xsize = 11;
points = 8; %number of circle interpolation points

PMLw = 2e-6;
WGh = 0.7e-6;
```

```
WGw = 1e-6;

stdev = 0; %hole shape standard deviation
posstdev = 0; %hole position standard deviation

sensorh = a*ysize;
sensorw = a*cos(pi/6)*(xsize-1)+a;

dy = a;
dx = cos(pi/6)*a;

numbholes = xsize*ysize - ceil(xsize/2);

xtot = PMLw + WGw + sensorw + WGw + PMLw;
ytot = PMLw + sensorh + PMLw;

%polygon coord
x11 = 0;
x12 = xtot;
y11 = PMLw + sensorh/2 - WGh/2;
y12 = y11;
x21 = x11;
x22 = x12;
y21 = PMLw + sensorh/2 + WGh/2;
y22 = y21;

%hole coordinates
x0 = zeros(1,numbholes);
y0 = x0;
hh = 1;
for ii = 1:xsize
    if mod(ii,2)
        for jj = 1:(ysize-1)
            x0(hh) = PMLw + WGw + a/2 + dx*(ii-1) + randn(1)*
                posstdev;
            y0(hh) = PMLw + dy*jj + randn(1)*posstdev;
            hh = hh + 1;
        end
    else
        for jj = 1:ysize
            x0(hh) = PMLw + WGw + a/2 + dx*(ii-1) + randn(1)*
                posstdev;
```

```
            y0(hh) = PMLw + dy/2 + dy*(jj-1) + randn(1)*posstdev;
            hh = hh + 1;
        end
    end

end


import com.comsol.model.*
import com.comsol.model.util.*


model = ModelUtil.create('Model');
geom1 = model.geom.create('geom1',2);
r1 = geom1.feature.create('r1','Rectangle');
r1.set('size',[sensorw sensorh]); %sensor rect
r1.set('pos',[PMLw+WGw PMLw]);

r2 = geom1.feature.create('r2','Rectangle');
r2.set('size',[xtot PMLw]); %PML bottom
r2.set('pos',[0 0]);

r3 = geom1.feature.create('r3','Rectangle');
r3.set('size',[xtot PMLw]); %PML top
r3.set('pos',[0 PMLw+sensorh]);

r4 = geom1.feature.create('r4','Rectangle');
r4.set('size',[PMLw sensorh]); %PML left
r4.set('pos',[0 PMLw]);

r5 = geom1.feature.create('r5','Rectangle');
r5.set('size',[PMLw sensorh]); %PML right
r5.set('pos',[PMLw+sensorw+2*WGw PMLw]);

r6 = geom1.feature.create('r6','Rectangle');
r6.set('size',[WGw sensorh]); %WG left
r6.set('pos',[PMLw PMLw]);

r7 = geom1.feature.create('r7','Rectangle');
r7.set('size',[WGw sensorh]); %WG right
r7.set('pos',[PMLw+WGw+sensorw PMLw]);

```

```
l1 = geom1.feature.create('pol1','Polygon');
l1.set('x',[x11 x12]);
l1.set('y',[y11 y12]);

l1 = geom1.feature.create('pol2','Polygon');
l1.set('x',[x21 x22]);
l1.set('y',[y21 y22]);

phi = 0:2*pi/points:2*pi;
phi(length(phi)) = [];

for hh = 1:numbholes
    if hh == ceil(numbholes/2)
        rng('shuffle')
        phi = phi + rand(1)*2*pi;
        rng('shuffle')
        rad = defectr*ones(1,length(phi)) + stdev*defectr*randn(1,
            length(phi));
    else
        rng('shuffle')
        phi = phi + rand(1)*2*pi;
        rng('shuffle')
        rad = r*ones(1,length(phi)) + stdev*r*randn(1,length(phi));
    end
    P = [(x0(hh) + rad.*cos(phi));(y0(hh) + rad.*sin(phi))];
    label = ['ic' num2str(hh)];
    temp = geom1.feature.create(label,'InterpolationCurve');
    temp.set('table',P');
    temp.set('type','solid');
end
hold off

figure(1)
mphgeom(model);
axis equal
asdasd = ['std' num2str(stdev) '-' date '_2.mphbin'];
geom1.exportFinal(asdasd)
ModelUtil.remove('Model');
toc
```

Appendix F

AutoScript

AutoScript is the programming language used for automating the FIB milling process. The first script mills the sensor structure, while the second mills the same structure multiple times over a specified area by moving the stage.

```
#MILL CIRCLE IN MIDDLE OF SCREEN
setactiveview 2
clear

totalx = 11
totalyset = 21

defectx = (totalx-1)/2
defecty = (totalyset-1)/2


a = 0.465
xa = 0.866*a
ystart = 0
xstart = 0

ypos = xstart
xpos = ystart
i=0


depth=0.2

setpatinfo depth, si
```

```
loop1:
j = 0
ypos = ystart
totaly = totalyset
if (i=0) totaly = totaly - 1
if (i=0) ypos = a/2
if (i=2) totaly = totaly - 1
if (i=2) ypos = a/2
if (i=4) totaly = totaly - 1
if (i=4) ypos = a/2
if (i=6) totaly = totaly - 1
if (i=6) ypos = a/2
if (i=8) totaly = totaly - 1
if (i=8) ypos = a/2
if (i=10) totaly = totaly - 1
if (i=10) ypos = a/2
loop2:
circle_radius=0.27
if (i=defectx) goto ifstart
ifend:

circle xpos, ypos, 0, circle_radius
mill
clear

j = j + 1
ypos = ypos + a
if (j < totaly) goto loop2


i = i + 1
xpos = xpos + xa
if (i < totalx) goto loop1


ifstart:
if (j=defecty) circle_radius = 0.14
if (i<totalx) goto ifend
```

```
i = 0
total_i = 5
```

```
loop1:
setactiveview 4
stagemovedelta xy, 0.001, 0.010

run hole.mil

if (i < total_i) goto loop1

result = 1
```

Bibliography

[1] J. D. Joannopoulos, P. R. Villeneuve, and S. H. Fan. Photonic crystals: Putting a new twist on light. *Nature*, 386(6621):143–149, 1997.

[2] P. C. Hemmer. *Faste Stoffers Fysikk*. Tapir Forlag, 1987.

[3] E. Yablonovitch. Inhibited spontaneous emission in solid-state physics and electronics. *Physical Review Letters*, 58:2059–2062, 1987.

[4] S. John. Strong localization of photons in certain disordered dielectric superlattices. *Physical Review Letters*, 58:2486–2489, 1987.

[5] A. Mekis, J. C. Chen, I. Kurland, S. H. Fan, P. R. Villeneuve, and J. D. Joannopoulos. High transmission through sharp bends in photonic crystal waveguides. *Physical Review Letters*, 77(18):3787–3790, 1996.

[6] L. H. Frandsen, A. V. Lavrinenko, J. Fage-Pedersen, and P. I. Borel. Photonic crystal waveguides with semi-slow light and tailored dispersion properties. *Optics Express*, 14 (20):9444–9450, 2006.

[7] D. Wang, Z. Yu, Y Liu, X. Guo, and S. Zhou. Optimization of a two-dimensional photonic crystal waveguide for ultraslow light propagation. *Journal of Optics*, 14(12): 125101, 2012.

[8] S. H. Fan, P. R. Villeneuve, J. D. Joannopoulos, and H. A. Haus. Channel drop filters in photonic crystals. *Optics Express*, 3(1):4–11, 1998.

[9] Y. Akahane, T. Asano, B. S. Song, and S. Noda. High-Q photonic nanocavity in a two-dimensional photonic crystal. *Nature*, 425(6961):944–947, 2003.

[10] J. S. Foresi, P. R. Villeneuve, J. Ferrera, E. R. Thoen, G. Steinmeyer, S. Fan, J. D. Joannopoulos, L .C. Kimerling, H. I. Smith, and E. P. Ippen. Photonic-bandgap microcavities in optical waveguides. *Nature*, 390(6656):143–145, 1997.

[11] P. Alivisatos. The use of nanocrystals in biological detection. *Nature Biotechnology*, 22(1):47–52, 2004.

[12] K. Lee and S. A. Asher. Photonic crystal chemical sensors: pH and ionic strength. *Journal of the American Chemical Society*, 122(39):9534–9537, 2000.

[13] M. Lee and P. M. Fauchet. Two-dimensional silicon photonic crystal based biosensing platform for protein detection. *Optics Express*, 15(8):4530–4535, 2007.

[14] M. Quirk and J. Serda. *Semiconductor Manufacturing Technology*. Prentice-Hall, 2001.

[15] B. Jalali and S. Fathpour. Silicon photonics. *Journal of Lightwave Technology*, 24(12): 4600–4615, 2006.

[16] X. Chen, C. Li, and H. K. Tsang. Device engineering for silicon photonics. *NPG Asia Materials*, 3(1):34–40, 2011.

[17] Y. B. Bolkhovityanov and O. P. Pchelyakov. GaAs epitaxy on Si substrates: modern status of research and engineering. *Physics-Uspekhi*, 51(5):437, 2008.

[18] J. L. Lawrie and Weiss S. M. *Silicon Photonics for Telecommunications and Biomedicine*, chapter Silicon photonics for biosensing applications. CRCPress, 2011.

[19] Dorfnerm D., T. Zabel, T. Hürlimann, N. Hauke, L. H. Frandsen, U. Rant, G. Abstreiter, and J. Finley. Photonic crystal nanostructures for optical biosensing applications. *Biosensors and Bioelectronics*, 24(12):3688–3692, 2009.

[20] D. F. Dorfner, T. Huerlimann, T. Zabel, L. H. Frandsen, G. Abstreiter, and J. J. Finley. Silicon photonic crystal nanostructures for refractive index sensing. *Applied Physics Letters*, 93(18), 2008.

[21] T. Kusserow, M. Wulf, R. Zamora, K. Kanwar, and H. Hillmer. Processing of photonic crystals in InP membranes by focused ion beam milling and plasma etching. *Microelectronic Engineering*, 102:25–28, 2013.

[22] M. Hill, M. Cryan, N. Lim, R. Varrazza, P. Heard, S. Yu, and J. Rorison. Fabrication of photonic crystal structures by focused ion beam etching. In *Transparent Optical Networks, 2004. Proceedings of 2004 6th International Conference on*, volume 2, pages 135–138, 2004.

[23] H. H. Tao, R. J. Liu, Z. Y. Li, S. Feng, Y. Z. Liu, C. Ren, B. Y. Cheng, D. Z. Zhang, H. Q. Ma, L. A. Wu, and Zhang Z. B. Mapping of complex optical field patterns in multimode photonic crystal waveguides by near-field scanning optical microscopy. *Physical Review B*, 74(20):205111, 2006.

[24] Y. Ruan, M. Kim, Y. Lee, B. Luther-Davies, and A. Rode. Fabrication of high-Q chalcogenide photonic crystal resonators by e-beam lithography. *Applied Physics Letters*, 90(7):071102–071102, 2007.

[25] Y. Matsubara, J. Taniguchi, and I. Miyamoto. Fabrication of three-dimensional hydrogen silsesquioxane resist structure using electron beam lithography. *Japanese Journal of Applied Physics*, 45(6B):5538–5541, 2006.

[26] G. A. DeRose, L. Zhu, J. K. S. Poon, A. Yariv, and A. Scherer. Periodic sub-wavelength electron beam lithography defined photonic crystals for mode control in semiconductor lasers. *Microelectronic Engineering*, 85(5–6):758–760, 2008. Proceedings of the Micro- and Nano-Engineering 2007 Conference {MNE} 2007.

[27] L. Wang, S. Zhang, Q. Wang, J. Chen, W. Jiang, and R. T. Chen. Fabrication of three-dimensional (3D) woodpile structure photonic crystal with layer by layer e-beam lithography. *Applied Physics A*, 95(2):329–334, 2009.

[28] S. K. Selvaraja, P. Jaenen, W. Bogaerts, D. Van Thourhout, P. Dumon, and R. Baets. Fabrication of photonic wire and crystal circuits in silicon-on-insulator using 193-nm optical lithography. *Journal of Lightwave Technology*, 27(18):4076–4083, 2009.

[29] W. Bogaerts, V. Wiaux, D. Taillaert, S. Beckx, B. Luyssaert, P. Bienstman, and R. Baets. Fabrication of photonic crystals in silicon-on-insulator using 248-nm deep UV lithography. *IEEE Journal of Selected Topics in Quantum Electronics*, 8(4):928–934, 2002.

[30] M. Settle, M. Salib, A. Michaeli, and T. F. Krauss. Low loss silicon on insulator photonic crystal waveguides made by 193nm optical lithography. *Optics Express*, 14 (6):2440–2445, 2006.

[31] Jens Høvik. Photonic crystal waveguide fabrication. Master's thesis, NTNU, 2012.

[32] Marius Lorvik. Photonic crystal structures. Master's thesis, NTNU, 2012.

[33] L. Vigen. Silicon racetrack resonator. Master's thesis, NTNU, 2014.

[34] Torstein Bolstad. Frequency domain simulations of a photonic crystal biosensor using FEM and MPB. Project thesis, NTNU, 2013.

[35] J. D. Joannopolous, S. G. Johnsonv, J. N. Winn, and R. D. Meade. *Photonic Crystals: Molding the Flow of Light*. Princeton University Press, second edition, 2008.

[36] B. E. A. Saleh and M. C. Teich. *Fundamentals of Photonics*. Wiley, second edition, 2007.

[37] C. Dirdal. Forelesningsnotater 5.09. 2013. URL `http://www.iet.ntnu.no/courses/tfe13/notater.html`.

[38] D. Van Thourhout, R. Baets, and H. Ottevaere. *Microphotonics*. Universiteit Gent, 2012.

[39] B. H. Bransden and C. J. Joachain. *Quantum Mechanics*. Prentice Hall, second edition, 2000.

[40] S. G. Johnson and J. D. Joannopoulos. Block-iterative frequency-domain methods for maxwell's equations in a planewave basis. *Optics Express*, 8(3):173–190, 2001.

[41] S. G. Johnson, S. Fan, P. R. Villeneuve, J. D. Joannopoulos, and L. A. Kolodziejski. Guided modes in photonic crystal slabs. *Physical Review B*, 60(8):5751, 1999.

[42] E. Chow, S. Y. Lin, S. G. Johnson, P. R. Villeneuve, J. D. Joannopoulos, J. R. Wendt, G. A. Vawter, W. Zubrzycki, H. Hou, and A. Alleman. Three-dimensional control of light in a two-dimensional photonic crystal slab. *Nature*, 407(6807):983–986, 2000.

[43] S. G. Johnson, P. R. Villeneuve, S. Fan, and J. D. Joannopoulos. Linear waveguides in photonic-crystal slabs. *Physical Review B*, 62(12):8212, 2000.

[44] S. Fan and J. D. Joannopoulos. Analysis of guided resonances in photonic crystal slabs. *Physical Review B*, 65(23):235112, 2002.

[45] C. G. Bostan and de R. M. Ridder. 'hexagon-type' photonic crystal slabs based on SOI. *IEEE/LEOS Benelux Chapter 2002 Annual Symposium*, 2002.

[46] S. Noda and T. Baba. *Roadmap on photonic crystals*, volume 1. Springer, 2003.

[47] O. Painter and K. Srinivasan. Localized defect states in two-dimensional photonic crystal slab waveguides: A simple model based upon symmetry analysis. *Physical Review B*, 68(3):035110, 2003.

[48] O. Painter, K. Srinivasan, J. D. O'Brien, A. Scherer, and P. D. Dapkus. Tailoring of the resonant mode properties of optical nanocavities in two-dimensional photonic crystal slab waveguides. *Journal of Optics A: Pure and Applied Optics*, 3(6):S161, 2001.

[49] O. Painter. *Optical nanocavities in two-dimensional photonic crystal planar waveguides*. PhD thesis, California Institute of Technology, 2001.

[50] Michael Tinkham. *Group theory and quantum mechanics*. Courier Dover Publications, 2012.

[51] J. V. Galán, P. Sanchis, and J. Martí. Low-loss coupling technique between SOI waveguides and standard single-mode fibers. *European Conference on Integrated Optics*, 2007.

[52] O. Mitomi, K. Kasaya, and H. Miyazawa. Design of a single-mode tapered waveguide for low-loss chip-to-fiber coupling. *IEEE Journal of Quantum Electronics*, 30(8):1787–1793, 1994.

[53] D. Taillaert, F. Van Laere, M. Ayre, W. Bogaerts, D. Van Thourhout, P. Bienstman, and R. Baets. Grating couplers for coupling between optical fibers and nanophotonic waveguides. *Japanese Journal of Applied Physics*, 45(8R):6071, 2006.

[54] F. Van Laere, G. Roelkens, M. Ayre, J. Schrauwen, D. Taillaert, D. Van Thourhout, T. F. Krauss, and R. Baets. Compact and highly efficient grating couplers between optical fiber and nanophotonic waveguides. *Journal of Lightwave Technology*, 25(1): 151–156, 2007.

[55] D. Vermeulen, S. Selvaraja, P. Verheyen, G. Lepage, W. Bogaerts, P. Absil, D. Van Thourhout, and G. Roelkens. High-efficiency fiber-to-chip grating couplers realized using an advanced CMOS-compatible silicon-on-insulator platform. *Optics Express*, 18(17):18278–18283, 2010.

[56] J. Schrauwen. *Focused Ion Beam Processing of Nanophotonic Structures*. PhD thesis, Ghent Universtiy, 2009.

[57] R. Renneberg. *Biotechnology for beginners*. Elsevier, 2008.

[58] S. Pal, E. Guillermain, R. Sriram, B. Miller, and P. M. Fauchet. Microcavities in photonic crystal waveguides for biosensor applications. In *BiOS*, pages 755304–755304. International Society for Optics and Photonics, 2010.

[59] F. Eftekhari, C. Escobedo, J. Ferreira, X. Duan, E. M. Girotto, A. G. Brolo, R. Gordon, and D. Sinton. Nanoholes as nanochannels: flow-through plasmonic sensing. *Analytical Chemistry*, 81(11):4308–4311, 2009.

[60] J. Humlicek. *Ellipsometry at the Nanoscale*, chapter Data Analysis for Nanomaterials: Effective Medium Approximation, Its Limits and Implementations. Springer Berlin Heidelberg, 2013.

[61] Z. H. Zhu, W. M. Ye, J. R. Ji, X. D. Yuan, and C. Zen. Influence of random errors on the characteristics of typical 2D photonic crystal microcavity. *Applied Physics B*, 88 (2):231–236, 2007. ISSN 0946-2171.

[62] W Fan, Z Hao, Z Li, Y Zhao, and Y Luo. Influence of fabrication error on the characteristics of a 2-d photonic-crystal cavity. *Journal of Lightwave Technology*, 28 (10):1455–1458, 2010.

[63] H. Hagino, Y. Takahashi, Y. Tanaka, T. Asano, and S. Noda. Effects of fluctuation in air hole radii and positions on optical characteristics in photonic crystal heterostructure nanocavities. *Physical Review B*, 79:085112, 2009.

[64] M. Lorvik. Investigating non-ideal effects in a 2D photonic crystal waveguide, using finite element method simulation software. Project thesis, NTNU, 2012.

[65] E. D. Palik. *Handbook of Optical Constants of Solids*. Academic Press, 1998.

[66] J. K. Hutchison and P. A. O'Brien. *RSC Nanoscience and Nanotechnology, Volume 3 : Nanocharacterisation*. Royal Society of Chemistry, 2007.

[67] A. Khursheed. *Scanning Electron Microscope Optics and Spectrometers*. World Scientific Publishing Co., 2010.

[68] H. Seiler. Secondary electron emission in the scanning electron microscope. *Journal of Applied Physics*, 54(11):R1–R18, 1983.

[69] R. F. Egerton. *Physical Principles of Electron Microscopy : An Introduction to TEM, SEM, and AEM*. Springer Science+Business Media, Inc., 2005.

[70] Norfab. `http://http://ntnu.norfab.no/`. Accessed: 2014-04-30.

[71] R. Waser. *Nanoelectronics and Information Technology*. Wiley-VCH, third edition, 2012.

[72] M. Hatzakis. Electron resists for microcircuit and mask production. *Journal of the Electrochemical Society*, 116(7):1033–1037, 1969.

[73] S. Thoms. *Nanofabrication Handbook*, chapter Electron Beam Lithography. CRC Press, 2012.

[74] I. Zailer, J. E. F. Frost, V. Chabasseur-Molyneux, C. J. B. Ford, and M. Pepper. Crosslinked PMMA as a high-resolution negative resist for electron beam lithography and applications for physics of low-dimensional structures. *Semiconductor Science and Technology*, 11(8):1235, 1996.

[75] K. Suzuki. *Microlithography: science and technology*, volume 126, chapter Electron Beam Lithography Systems. CRC press, 2010.

[76] K. M. Beckwith. EBL tricks: Improving EBL performance for writing nanostructure arrays over large areas. Technical report, NTNU, 2013.

[77] M. A. Mohammad, M. Muhammad, S. K. Dew, and M. Stepanova. Fundamentals of electron beam exposure and development. In *Nanofabrication*, pages 11–41. Springer, 2012.

[78] J. Melngailis. Focused ion beam technology and applications. *Journal of Vacuum Science & Technology B*, 5(2):469–495, 1987.

[79] K. Kant and D. Losic. Focused ion beam (FIB) technology for micro-and nanoscale fabrications. In *FIB Nanostructures*, pages 1–22. Springer, 2013.

[80] W. C. L. Hopman, F. Ay, W. Hu, V. J. Gadgil, L. Kuipers, M. Pollnau, and R. M. de Ridder. Focused ion beam scan routine, dwell time and dose optimizations for submicrometre period planar photonic crystal components and stamps in silicon. *Nanotechnology*, 18(19):195305, 2007.

[81] C. A. Volkert and A. M. Minor. Focused ion beam microscopy and micromachining. *MRS Bulletin*, 32(05):389–399, 2007.

[82] P. R. Munroe. The application of focused ion beam microscopy in the material sciences. *Materials Characterization*, 60(1):2–13, 2009.

[83] M. Kolíbal, T. Matlocha, T. Vystavěl, and T. Šikola. Low energy focused ion beam milling of silicon and germanium nanostructures. *Nanotechnology*, 22(10):105304, 2011.

[84] L. A. Giannuzzi and F. A. Stevie. *Introduction to focused ion beams: instrumentation, theory, techniques and practice*. Springer, 2005.

[85] S. Reyntjens and R. Puers. A review of focused ion beam applications in microsystem technology. *Journal of Micromechanics and Microengineering*, 11(4):287, 2001.

[86] W. C. L. Hopman, F. Ay, and R. M. de Ridder. Focused ion beam milling strategy for sub-micrometre holes in silicon. *First International Workshop on FIB for Photonics*, 2008.

[87] S. Rubanov and P. R. Munroe. FIB-induced damage in silicon. *Journal of Microscopy*, 214(3):213–221, 2004.

[88] J. P. Biersack and J. F. Ziegler. The stopping and range of ions in solids. In H. Ryssel and H. Glawischnig, editors, *Ion Implantation Techniques*, volume 10 of *Springer Series in Electrophysics*, pages 122–156. Springer Berlin Heidelberg, 1982.

[89] D. Z. Xie, B. K. A. Ngoi, W. Zhou, and Y. Q. Fu. Fabrication and thermal annealing behavior of nanoscale ripple fabricated by focused ion beam. *Applied Surface Science*, 227(1):250–254, 2004.

[90] H. H. Tao, C. Ren, S. Feng, Y. Z. Liu, Z. Y. Li, B. Y. Cheng, D. Z. Zhang, and A. Z. Jin. Optical improvement of photonic devices fabricated by Ga+ focused ion beam micromachining. *Journal of Vacuum Science & Technology B*, 25(5):1609–1614, 2007.

[91] Y. Q. Fu, N. K. A. Bryan, O. N. Shing, and N. P. Hung. Influence of the redeposition effect for focused ion beam 3D micromachining in silicon. *The International Journal of Advanced Manufacturing Technology*, 16(12):877–880, 2000.

[92] M. Shearn, X. Sun, M. D. Henry, A. Yariv, and A. Scherer. Advanced plasma processing: etching, deposition, and wafer bonding techniques for semiconductor applications. 2010.

[93] R. Legtenberg, H. Jansen, M. de Boer, and M. Elwenspoek. Anisotropic reactive ion etching of silicon using SF6/O2/CHF3 gas mixtures. *Journal of The Electrochemical Society*, 142(6):2020–2028, 1995.

[94] C. Gatzert, A. W. Blakers, P. N. K. Deenapanray, D. Macdonald, and F. D. Auret. Investigation of reactive ion etching of dielectrics and Si in CHF3/O2 or CHF3/Ar for photovoltaic applications. *Journal of Vacuum Science & Technology A*, 24(5):1857–1865, 2006.

[95] M. Schaepkens, T. E. F. M. Standaert, N. R. Rueger, P. G. M. Sebel, G. S. Oehrlein, and J. M. Cook. Study of the SiO2-to-Si3N4 etch selectivity mechanism in inductively coupled fluorocarbon plasmas and a comparison with the SiO2-to-Si mechanism. *Journal of Vacuum Science & Technology A*, 17(1):26–37, 1999.

[96] B. El-Kareh. *Fundamentals of semiconductor processing technologies*. Springer, 1994.

[97] K. S. S. Harsha. *Principles of vapor deposition of thin films*. Elsevier, 2005.

[98] K. X. Chen, R. Mirhosseini, and E. F. Schubert. Parameters used in E-beam deposition system. http://www.ecse.rpi.edu/ schubert/Course-Teaching-modules/A040-Parameters-used-in-E-beam-deposition-system.pdf.

[99] P. Hlubina, J. Luňáček, D. Ciprian, and R. Chlebus. Spectral interferometry and reflectometry used to measure thin films. *Applied Physics B*, 92(2):203–207, 2008.

[100] C. G. Bostan, R. M. de Ridder, V. J. Gadgil, H. Kelderman, L. Kuipers, and A. Driessen. Design and fabrication of line-defect waveguides in hexagon-type SOI

photonic crystal slabs. In *Photonics Europe*, pages 323–332. International Society for Optics and Photonics, 2004.

[101] Y. K. Kim, A. J. Danner, J. J. Raftery, and K. D. Choquette. Focused ion beam nanopatterning for optoelectronic device fabrication. *IEEE Journal of Selected Topics in Quantum Electronics*, 11(6):1292–1298, 2005.

[102] A. Hayat, N. Berkovitch, and M. Orenstein. Enhanced resolution and high aspect-ratio semiconductor nanopatterning by metal overcoating. *Applied Physics Letters*, 94(6): 063103, 2009.

[103] K. P. Yap, A. Delâge, J. Lapointe, B. Lamontagne, J. H. Schmid, P. Waldron, B. A. Syrett, and S. Janz. Correlation of scattering loss, sidewall roughness and waveguide width in silicon-on-insulator (SOI) ridge waveguides. *Journal of Lightwave Technology*, 27(18):3999–4008, 2009.

[104] F. P. Payne and J. P. R. Lacey. A theoretical analysis of scattering loss from planar optical waveguides. *Optical and Quantum Electronics*, 26(10):977–986, 1994.

[105] D. Gerace and L. C. Andreani. Effects of disorder on propagation losses and cavity Q-factors in photonic crystal slabs. *Photonics and Nanostructures - Fundamentals and Applications*, 3(2–3):120 – 128, 2005.

[106] W. Bogaerts, P. Bienstman, and R. Baets. Scattering at sidewall roughness in photonic crystal slabs. *Optics Letters*, 28(9):689–691, 2003.

[107] K. R. Maskaly. *Computational Study and Analysis of Structural Imperfections in 1D and 2D Photonic Crystals*. PhD thesis, Massachusetts Institute of Technology, 2000.

[108] K. K. Lee, D. R. Lim, H. C. Luan, A. Agarwal, J. Foresi, and L. C. Kimerling. Effect of size and roughness on light transmission in a Si/SiO2 waveguide: Experiments and model. *Applied Physics Letters*, 77(11):1617–1619, 2000.

[109] Y. Tanaka, T. Asano, Y. Akahane, B. S. S., and S. Noda. Theoretical investigation of a two-dimensional photonic crystal slab with truncated cone air holes. *Applied Physics Letters*, 82(11):1661–1663, 2003.

[110] L. O'Faolain, X. Yuan, D. McIntyre, S. Thoms, H. Chong, R. M. De La Rue, and T. F. Krauss. Low-loss propagation in photonic crystal waveguides. *Electronics letters*, 42 (25):1454–1455, 2006.

[111] R. Ferrini, B. Lombardet, B. Wild, R. Houdré, and G. H. Duan. Hole depth- and shape-induced radiation losses in two-dimensional photonic crystals. *Applied Physics Letters*, 82(7):1009–1011, 2003.

[112] E. Rogstad. personal communication, 2014.

[113] R. J. Young, J. R. A. Cleaver, and H. Ahmed. Characteristics of gas-assisted focused ion beam etching. *Journal of Vacuum Science & Technology B*, 11(2):234–241, 1993.

[114] L. M. Ephrath. Selective etching of silicon dioxide using reactive ion etching with CF 4-H 2. *Journal of The Electrochemical Society*, 126(8):1419–1421, 1979.

[115] H. B. Morris. Method of depositing titanium dioxide (rutile) as a gate dielectric for MIS device fabrication, 1980. US Patent 4,200,474.

[116] O. Powell, D. Sweatman, and H. B. Harrison. The use of titanium and titanium dioxide as masks for deep silicon etching. *Smart Materials and Structures*, 15(1):S81, 2006.

[117] K. R. Ervik. personal communication, 2014.

[118] W. Bogaerts, R. Baets, P. Dumon, V. Wiaux, S. Beckx, D. Taillaert, B. Luyssaert, J. Van Campenhout, P. Bienstman, and D. Van Thourhout. Nanophotonic waveguides in silicon-on-insulator fabricated with cmos technology. *Lightwave Technology, Journal of*, 23(1):401–412, 2005.

[119] B. Prasai, B. Cai, M. K. Underwood, J. P. Lewis, and D. A. Drabold. Properties of amorphous and crystalline titanium dioxide from first principles. *Journal of Materials Science*, 47(21):7515–7521, 2012.

[120] G. W. Burr, S. Diziain, and M. P. Bernal. The impact of finite-depth cylindrical and conical holes in lithium niobatephotonic crystals. *Optical Express*, 16(9):6302–6316, 2008.

[121] Y. Vlasov and S. McNab. Losses in single-mode silicon-on-insulator strip waveguides and bends. *Optical Express*, 12(8):1622–1631, 2004.

[122] S. L. Lai, D. Johnson, and R. Westerman. Aspect ratio dependent etching lag reduction in deep silicon etch processes. *Journal of Vacuum Science & Technology A*, 24(4):1283–1288, 2006.

[123] H. Jansen, H. Gardeniers, M. de Boer, M. Elwenspoek, and J. Fluitman. A survey on the reactive ion etching of silicon in microtechnology. *Journal of Micromechanics and Microengineering*, 6(1):14, 1996.

[124] A. E. Grigorescu and C. W. Hagen. Resists for sub-20-nm electron beam lithography with a focus on HSQ: state of the art. *Nanotechnology*, 20(29):292001, 2009.

[125] Y. Sugimoto, N. Ikeda, N. Carlsson, K. Asakawa, N. Kawai, and K. Inoue. Fabrication and characterization of different types of two-dimensional AlGaAs photonic crystal slabs. *Journal of Applied Physics*, 91(3):922–929, 2002.

[126] S. Cabrini, A. Carpentiero, R. Kumar, L. Businaro, P. Candeloro, M. Prasciolu, A. Gosparini, C. Andreani, M. De Vittorio, T. Stomeo, and E. Di Fabrizio. Focused ion beam lithography for two dimensional array structures for photonic applications. *Microelectronic Engineering*, 78–79(0):11–15, 2005. Proceedings of the 30th International Conference on Micro- and Nano-Engineering.

[127] D. Z. Xie, B. K. A. Ngoi, W. Zhou, and Y. Q. Fu. Fabrication and thermal annealing behavior of nanoscale ripple fabricated by focused ion beam. *Applied surface science*, 227(1):250–254, 2004.

[128] Y. K. Kim, A. J. Danner, J. J. Raftery, and K. D. Choquette. Focused ion beam nanopatterning for optoelectronic device fabrication. *Selected Topics in Quantum Electronics, IEEE Journal of*, 11(6):1292–1298, 2005.

[129] H. A. Haus. *Waves and Fields in Optoelectronics*. Prentice-Hall, 1984.

[130] MIT photonic bands, June 2014. URL `http://ab-initio.mit.edu/wiki/index.php/MIT_Photonic_Bands`.

[131] *COMSOL Multiphysics v4.3 documentation*, 2014.

[132] A. Quarteroni. *Numerical Models for Differential Problems*. Springer, first edition, 2009.